DECIPHERING THE MOLECULAR MECHANISMS OF ORGANIC CRYSTALLIZATION

by
Rajshree Chakrabarti

A dissertation submitted to the William A. Brookshire Department of Chemical and Biomolecular Engineering

in partial fulfillment of the requirements for the degree of

DOCTOR OF PHILOSOPHY

in Chemical Engineering

Chair of Committee: Dr. Peter G. Vekilov

Committee Member: Dr. Jeffrey D. Rimer

Committee Member: Dr. Jeremy C. Palmer

Committee Member: Dr. Viktor G. Hadjiev

Committee Member: Dr. Ognjen Š. Miljanić

University of Houston

May 2021

ACKNOWLEDGEMENTS

First and foremost, I would like to express my sincerest gratitude for my advisor Dr. Peter G. Vekilov. I am extremely grateful for this opportunity to be advised by you. I have learnt a lot from you and thank you making me the person, I am today. Hopefully, one day I can make you proud. You taught me how to think critically and how to be calm under pressure and thank you for giving direction to my research. You have guided me through not only professional but also personal crisis. To Professor Jeffrey D. Rimer thank you very much for your advice on several of my research projects your suggestions have been very crucial for the completion of my thesis. To professor Jeremey C. Palmer, I will be forever grateful to you for your contributions towards the better understanding of the molecular mechanisms during organic crystallization. To Dr. Viktor G. Hadjiev, thank you very much for serving in my committee and proving crucial insights for the dimer formation of etioporphyrin I in organic solvents, your guidance and help was the very essential for my successful PhD thesis. To Dr. Ognjen Š. Miljanić, thank you very much for your suggestions, comments and for serving in my PhD defense committee.

Dear Karoline Muller, I would like to thank you not for the scientific discussions and help with powder XRD but also for the introducing me to the world of amazing no-oil vegan dishes. To Monica Warzecha, I would like to thank you for everything that you have done for me, the amazing scientific discussions to great advices in the field of crystallography. Thank you very much for the single crystal XRD of my crystals.

To Katy Newlin, Mike Byington and Mohamad Safari, thank you for being amazing seniors and nurturing three new graduate students, me, Alex and Wenchuan in the Spring of 2017. Thank you for listening to me and for providing your helping hand whenever possible.

To Yolanda Thomas, Nicollet Solano, and Miranda Vernon-Harrison, thank you for making sure that all our paperwork, course work are in line with requirements, and timely reminders which made the graduation process smooth. To David Dawlearn thank you very much for the safety advice, hot soups, and amazing personal advice. To Alpana Thorat, thank you very much for the professional and personal advice.

To my lab mates Wenchuan Ma, Alex Xu, David Yang, Lakshman Ji Verma (it was amazing collaborating with you), Sima Mafi Moghaddam thank you very much for all the support, love, and care that you all have given me. To my friends in no order Sujina Mali, Anuradha Marathe, Oshin Malhara, Nilamani Venisetty, Deepjyoti Ghosh, Shreya Bhattacharya, Prajakta Bedekar, Deepanwita, Monali, Tattwamasi Amrutham, and Priyam Verma thank you very much for supporting me through thick and thin and somehow guiding me through this journey.

To my parents Sanghamitra Chakrabarti, Partha Pratim Chakrabarti, and brother Ananya Chakrabarti, I will be forever grateful to you three for always loving, supporting, and caring for me.

To Sumitava, my husband for standing by my side during my PhD journey. To dear Medha and Champakali thank you for all your love, care, and support. To Sarada Ma, Sri Ramakrishna and Swami Vivekananda for having my back always.

ABSTRACT

Crystallization is a central part of several physiological, pathological processes, in the manufacturing of pharmaceuticals, fine chemicals, semiconductors, and many other engineered materials. Organic solvents are extensively used for crystallization of organic small molecules such as active pharmaceutical ingredients and organic molecules like porphyrins. Fundamental studies on organic crystallization are important as solution thermodynamics plays an important role in crystal growth rates. Solvent structuring and solute–solvent interactions are yet unexplored realms of organic crystallization, whereas aqueous crystallization where the H-bonds of water molecules play an important role of controlling the solution thermodynamics is relatively well understood. In this work we address the effects of factors like solute-solvent interactions, solvent viscosity, and solvent size. We determine the solution thermodynamics of etioporphyrin I crystallization from a line of five organic solvents highlighting the role of several solute- solvent interactions. We use these solubility measurements and complement them with X-ray diffraction and UV-vis spectroscopy of the solution phase. From the thermodynamics data we shed light on the solute-solvent interactions. For organic solvents with weak solvent -solvent bonds, solvent structuring at the crystal interface is weak resulting in a lower activation energy barrier for solute incorporation into the growth sites. We showed that the solute-solvent interactions govern the mode of solute incorporation into the growth sites. Results on the growth mechanism of etioporphyrin I reveal that an incoming solute molecule occupies a state where it is only partially attached to the kink and this state precedes full incorporation. The stability of this intermediate state dictates the activation barrier for growth and, ultimately, the crystal growth rate. We explored the composition of the solute species that

exist in the solution and incorporate in the crystal and found out that, at least in one case, that of etioporphyrin I, a continuum of solute dimers are present in the solution and reform on their way to a kink into a growth competent conformation. This latter mechanism fully deviates from the assumption of the classical theories of crystal nucleation and growth, which posit that only solute monomers can associate to the kinks.

On exploring the mechanisms employed by foreign additives to impact the propagation of steps on a crystal surface we demonstrate that certain modifiers may exert dual action, by blocking both the kinks and the steps. These novel finding will help us control crystallization process development with desired end product features like crystal shape, size and from.

TABLE OF CONTENTS

LIST OF TABLES

LIST OF FIGURES

Chapter 1: Introduction to Crystal Growth

Crystalline materials are present in every aspects of our life, be it crystals occurring naturally (biomineralization[1,2] or pathological crystallization[3,4]) or industrially[5,6] engineered. Crystallization is a continually growing field that impacts a myriad of applications spanning energy and electronics to medicine. Fundamental knowledge of crystal growth mechanisms can be used to develop novel and more efficient methods of tailoring material properties (e.g., size and habit) for improved performance in commercial processes. Solution-grown crystalline materials are implemented in numerous applications owing to their chemical, mechanical, optical, and electrical properties. Single crystals of inorganic salts or mixed organic-inorganic materials are used in non-linear optics elements[7] and for other electronic and optical-electronic applications[8]. Chemical products and intermediates are precipitated as crystals in thousands-of-tons quantities[9]. Many pharmaceuticals are crystalline in nature that are specifically designed to exhibit a slow crystal dissolution rate for the sustained release of medications over longer periods of time compared to their amorphous or soluble counterparts[10-14].

The need for predictive control of the physical and chemical properties of crystals and of crystalline populations has driven research efforts to elucidate the fundamental processes of crystallization[15]. Many challenges to the traditional understanding of crystal growth mechanisms and the respective control parameters remain. For numerous systems, quantitative information of the thermodynamics and kinetics of solute incorporation into crystals is still missing, and these gaps hamper the development of efficient, sophisticated methods to prepare new and improved crystalline materials[16]. Growth of crystals can be

classified as classical or non-classical depending on the pathways taken by the incorporating species.

1.1 Solution Crystallization

Solution crystallization is an essential element of many industrial, natural, and physiological processes.[17,18] Numerous chemical products and production intermediates are precipitated as crystals in thousands-of-ton quantities[19]. Crystal synthesis is a central step in pharmaceuticals manufacture since crystalline drugs offer the advantage of steady medication release rates that are maintained for longer periods than amorphous or solubilized formulations.[20-24] The grand challenge in the area is the control of the nucleation and growth of crystals of complex chemical compounds. Successful and versatile control strategies rest on understanding the fundamental thermodynamic and kinetic mechanisms of crystallization.[17]

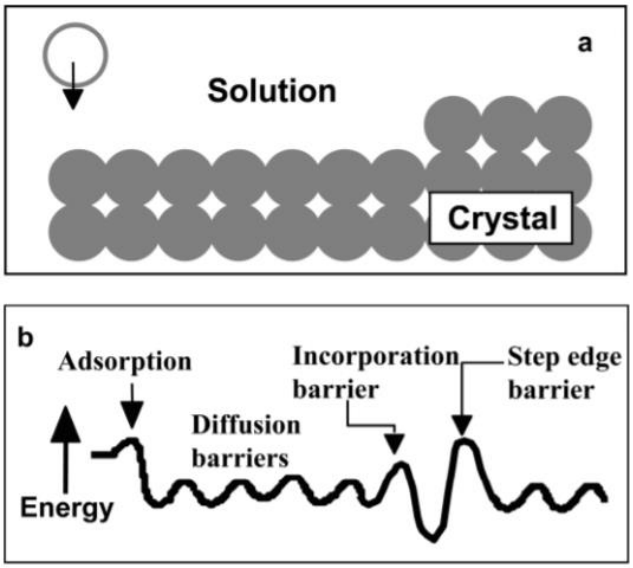

Figure 1: Schematic of (a) physical landscape and (b) energy landscape seen by a solute molecule as it becomes part of the crystal[25].

Traditional crystallization procedures employ aqueous solutions where the corresponding mechanisms have been studied in detail at all relevant lengthscales:

macroscopic, mesoscopic, and molecular. At the macroscopic scale we now understand the transport of solute and impurities towards the crystal–solution interface,[26-30] the relative significance of convection and diffusion,[30,31] and their impact on crystal surfaces that may provoke growth instabilities and engender defects.[32-34] At the mesoscopic scale, we attribute the faceted morphology of the majority of solution grown crystals to the high surface free energy of the crystal–solution interface and explain the relative significance of the individual crystal faces in the equilibrium crystal shape through the surface free energy anisotropy.[35,36] At the molecular lengthscale, a fundamental property of water to form a three-dimensional network of hydrogen bonds, molded around solute molecules and along the crystal surface, has been identified as a major factor that determines the thermodynamic and kinetic parameters of solute incorporation into growth sites[35,37-44] and, correspondingly, the pathways and the rates of crystallization from aqueous solvents.[45-48]

1.2 Mechanism of Crystal Growth

When crystals grow from solution, the incorporating molecules can take several different pathways as shown in figure 1[49], these pathways can be broadly classified as classical and non-classical. It depends on growth conditions like solvent, temperature, pressure, ion concentration, presence of impurities or growth modifiers present in the system. It is important to understand these different molecular pathways as understanding the energy barrier for these distinct pathways will help us control the thermodynamics and kinetics of crystallization processes thus controlling the physicochemical property of the final crystalline product.

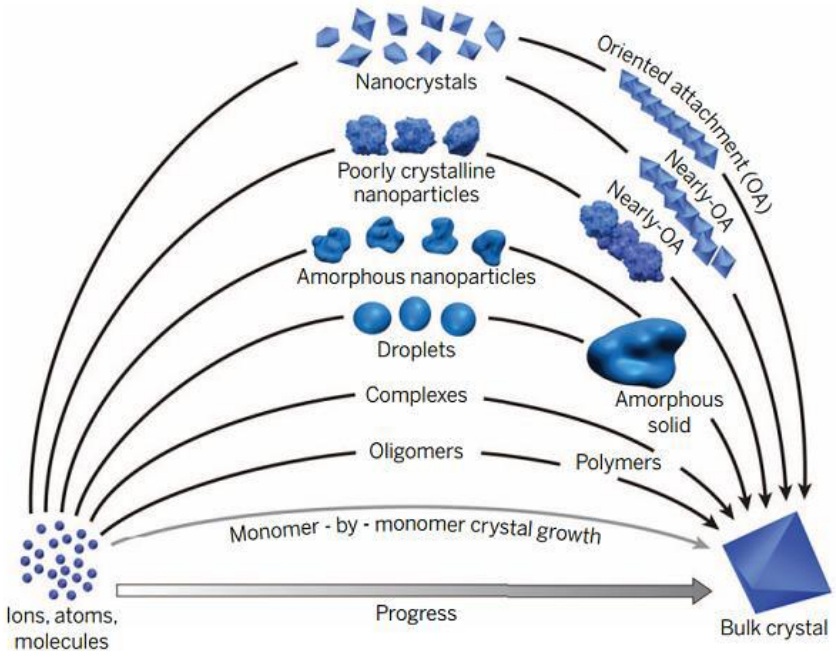

Figure 2: Crystallization Routes. Schematics of several pathways that a building block can take towards the growth of a bulk crystal. Classical routes involve the addition of monomeric species to the crystal lattice and non-classical pathways involve increasing complex precursory particle incorporation[49].

1.2.1 Classical Crystallization

During classical crystallization growth occurs via monomer-by-monomer attachment from solution to the crystal interface. While non-classical crystallization consists of an ever-expanding pathway of precursors more complex than a monomer. Crystallization is driven by the difference in the chemical potential μ between the crystal and the solution surrounding the growing interface. When the μ between the two phases are in equilibrium there is no driving force for growth and the crystal is at its solubility C_e. The Gibbs free energy change is given by

$$dG = VdP - SdT, \tag{1}$$

where S is the enthalpy, T is temperature, P is pressure, and V is volume. This fundamental thermodynamic equation can be rearranged to give the Clapeyron equation

$$\frac{dP}{dT} = \frac{\Delta S}{\Delta V} = \frac{\Delta H}{T\Delta v}. \quad (2)$$

Assuming that the system behaves as an ideal gas and that the solute is relatively dilute then the Clausius – Clapeyron equation can be applied as follows

$$\frac{dlnP}{dT} = \frac{\Delta H}{RT^2}. \quad (3)$$

To evaluate the standard enthalpy ΔH^o_{cryst} of crystallization from solution, it is noted that, in the crystallization equilibrium: etioporphyrin I (solution) ⇆ etioporphyrin I (crystal) where the product is a solid phase and has activity of one. The activity of the soluble solute (e.g., etioporphyrin I) was assumed to be equal to its concentration and is justified by the low solubility values which correspond to long intermolecular separations, at which the intermolecular interactions are weak, and the activity coefficients are near unity for this work. As a result, the equilibrium constant for crystallization is

$$K_{cryst} = c_e^{-1}. \quad (4)$$

The temperature *T* dependence of solubility c_e *(T)* is given by the classical van't Hoff's equation

$$\frac{\partial lnc_e}{\partial(1/T)} = \frac{\Delta H^o_{cryst}}{R}, \quad (5)$$

Where *R* is the universal gas constant. The slope of c_e data plotted in van't Hoff's coordinates *ln* c_e Vs *(1/T)* yields ΔH^o_{cryst}. The solubility of the solute in each solvent gives the Gibbs free energy and entropy of crystallization.

$$\Delta G^o_{cryst} = -RTlnK_{cryst} = RTlnc_e. \quad (6)$$

The crystallization entropy reflects the translational and rotational degrees of freedom lost when a solute molecule incorporates into the crystal lattice, it is slightly balanced by the vibrational degrees of freedom gained by the solute molecules and translational and rotational degrees of freedom gained by the solvent molecules. The thermodynamic

parameters act as sensitive tools to determine the solvent-solute interactions in the solution phase and solvent structuring at the crystal interface. The H-bonds in aqueous solvents contribute to the solution thermodynamics and thus governing solute incorporation into the growth sites. Through this work we study the effect of organic solvent- solvent bonds on the solution thermodynamics. Crystal growth rate depends on the thermodynamic free energy of the system. The process of crystallization leads to the formation of a new phase will lower free energy. The nucleation rates depend on the supersaturation, which is defined as the difference in chemical potentials $\Delta\mu$ of the growth solution and the crystal given by

$$\Delta\mu = \mu_c(C) - \mu_l(C). \quad (7)$$

The crystal growth rate, R which depends on the supersaturation is given by

$$R = \beta v(C - C_o), \quad (8)$$

where β is the step kinetic coefficient (nm/s), v (nm/s) step velocity and C, solute concentration and C_o, solubility. On a molecular level, crystals grow by the spreading of layers as the solute molecules attaching to the crystal growth sites known as the kinks. A Kossel crystal (Figure 2) is a model system which demonstrates the most common site on crystal facets for monomer and or modifier attachment: kinks, steps and terraces (Figure 2). Terraces are the flat surface areas between step edges; step are the layers made of growth units propagating across the surface; kinks form the step edges where incoming solute molecules incorporate where half the crystal bonds are unfinished.

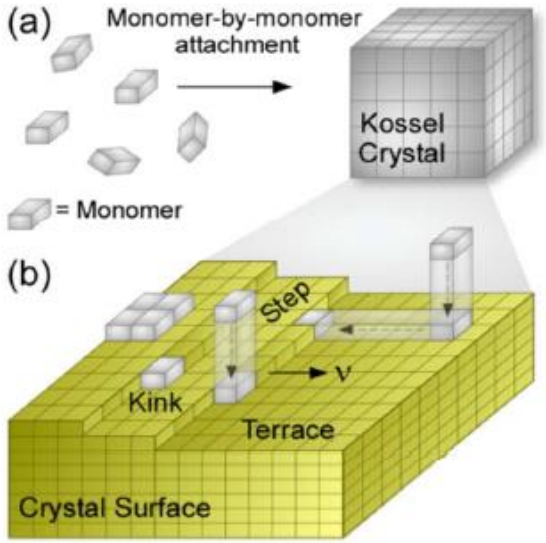

Figure 3: Kossel crystal and surface features. Schematic of a Kossel crystal illustrating crystal surface features like crystal terrace, steps, and kinks where solute molecule attaches[50].

On the crystal surface there are five important sites where the monomers can attach as shown in figure 3: (1) vacancies on terraces/faces, (2) hole in a step, (3) kink, (4) step edge, and (5) directly on top of terrace or face. Each active site has a specific surface free energy because of the unsaturated and saturated bonds. Voids place substantial strain on the crystal lattice as five units each have a single dangling bond; further, a molecule cannot add to the next layer until the void is filled. Therefore, voids are the most likely to be filled but are generally uncommon sites as they are filled quickly so that the second layer can generate and advance. Step edges contain two unsaturated bonds, and a kink site has three. Molecules that add to a step edge generate new kink sites through 1-dimensional (1D) nucleation events, but due to the amount of unsaturated bonds on a 1D nuclei, the molecule will most likely diffuse along the step edge until it is incorporated at a kink. As solute undergoes Brownian diffusion in solution towards a crystal interface it displaces solvent molecules. Solvent behaves differently in the bulk compared to a few nanometers away

from a solid interface. Therefore, as solute attaches to kink sites it must displace solvent along its path. By classical definition, a crystal grows when a molecule from solution adds to a kink site or the "half crystal position." Monomer incorporation into a kink site is the most energetically favorable due to the formation of three monomer-crystal bonds (compared to two bonds for steps and a single bond for terraces) since the amount of dangling bonds present on a crystal surface changes the surface energy. There are three reasons why attachment to this growth site at a crystal interface is essential: 1) attachment to a kink generates a new kink, 2) the same amount of saturated and unsaturated bonds are formed and regenerated, and 3) the surface free energy of the crystal surface remains unchanged. The degree of supersaturation surrounding the crystal interface is the driving force behind monomer addition. The rate of growth is proportional to the supersaturation. The slowest growing faces of the crystal determines the final crystal habit.

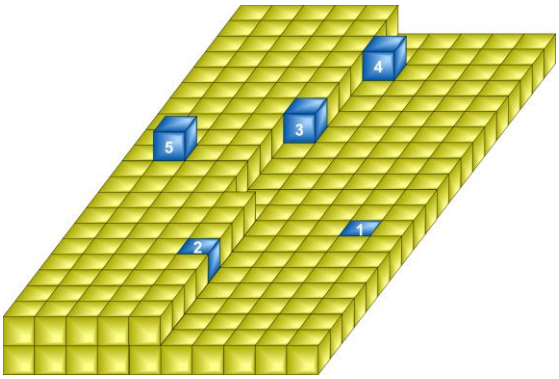

Figure 4: Sites for monomer attachment. Schematic showing the five sites for monomer attachment during classical crystallization.

1.2.2 Direct incorporation and surface diffusion

Modes of monomer incorporation can be by two different pathways[51] 1. direct incorporation and 2. surface diffusion (figure 4). Molecules can attach to kink sites directly, wherein they diffuse through solution until they reach a kink with a single energy barrier as denoted in figure 4. The pathway for incorporation can be of increasing complexity if a

molecule becomes incorporated into a kink via surface diffusion. Here multiple energy barriers are presented as the molecule first diffused through solution, adsorbs onto the surface (thereby displacing solvent molecules that are structured around the crystal interface), diffuse along the terrace, and finally gets incorporated into the kinks[52,53]. Combining these different energy barriers poses a vastly different time scale for solute addition to a crystal. The growth rate for crystallization is governed by the kink density and the energy barriers that are present during crystallization. The barriers have both enthalpic and entropic contributions which arise from displacing solvent, resulting latent heat due to bond formation/disassociation, and forming a more ordered system (which defies the second law of thermodynamics). Enthalpic contributions allow the phase transformation to occur by minimizing the overall free energy of the system. Solute-solvent interactions are important in determining the solution phase enthalpy.

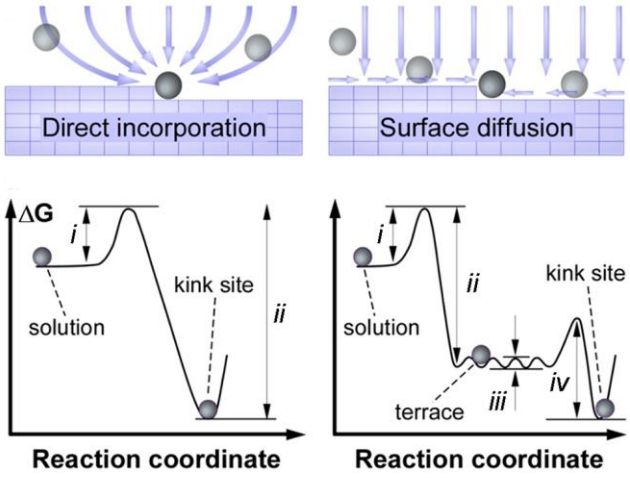

Figure 5: Mode of solute incorporation. Schematics showing direct incorporation and surface diffusion and the corresponding energy barriers[52].

Both pathways involve dynamic events at sites presented along the solid-liquid interface. Direct incorporation occurs when a monomer in solution attaches to a kink, step edge, or terrace site. Alternatively, monomers can add to a kink/step site after first

adsorbing onto a crystal terrace, then diffusing along the surfaces and attaching to the growth site. The lifetime of a monomer on a crystal surface is governed by desorption, adsorption, and surface "hopping" that lead to a dynamic sequence of events. The immediate layer of solvent surrounding the crystal surface can impose barriers for monomer (or modifier) adsorption. In aqueous solutions, water structuring can occur for up to three layers from the liquid-solid interface[54]. Adsorbate interaction with crystal sites invariably requires the displacement of solvent molecules – an energetic barrier predominantly governed by entropy.

1.2.3 Generation of Crystal Layers

Crystals grow by spreading of layers, at low supersaturations the growth hillock emanates from a screw dislocation due to partial shifting of planes causing a linear defect resulting in an edge or screw dislocation (figure 6).

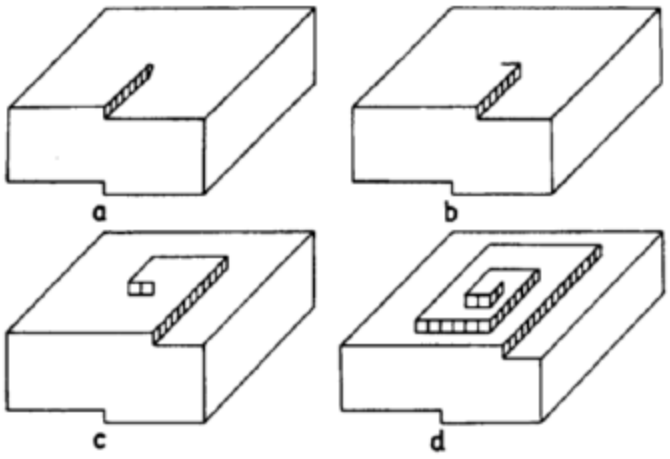

Figure 6: Dislocation as the source of layer generation. Layers spreading from screw dislocations[25].

At low supersaturations σ near equilibrium layers grow from screw dislocation it has been observed for several crystals as shown in figure 7. Another common method of layer formation and spreading is via 2D nucleation shown in figure 8 (a) and (b) for calcite and

canavalin crystals, respectively. 2D nucleation mostly dominates at higher σ. Higher supersaturation allows for heterogeneous nucleation to occur on a growing crystal face such that 2-dimensional (2D) islands form in between successive turns of a hillock. At very high supersaturations kinetic roughening occurs where the individual crystal layers become indistinguishable from one another and perpendicular growth to the growing crystal face dominates.

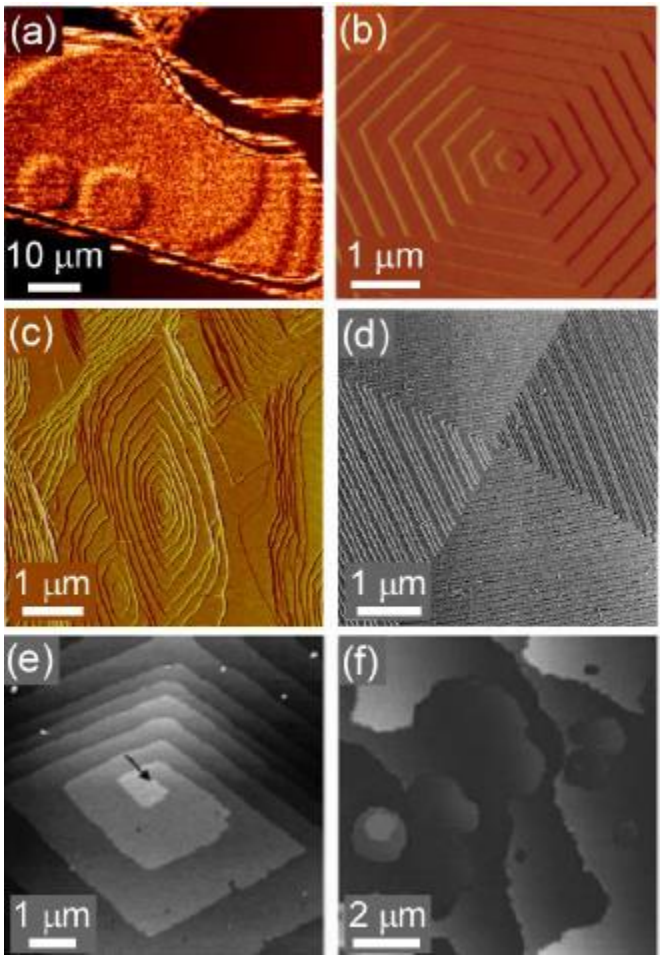

Figure7: Examples of layer growth with 2D or screw dislocation. (a) 2D nucleation of ice crystals[55], screw dislocation on (b) L-cystine crystal (001) surface[56] (c) calcium oxalate monohydrate crystal (010) surface[3], (d) calcite crystal {1014 surface[57], (e) insulin crystal (100)[58] and (f) ferritin crystal (111) surface[51] with 2D nucleation.

During growth by 2D nucleation of island and spreading of layers, two kinetic parameters need to be quantified. The step velocity v and the rate of nucleation J_{2D} are a function of the supersaturation σ which correlated to $\Delta\mu/kT$, the relative driving force for crystallization. The rate of nucleation is defined as the number of nuclei that grow per area per unit time [nucleation events/nm^2/s]. Both measurable values vary depending on crystal facet and other growth conditions.

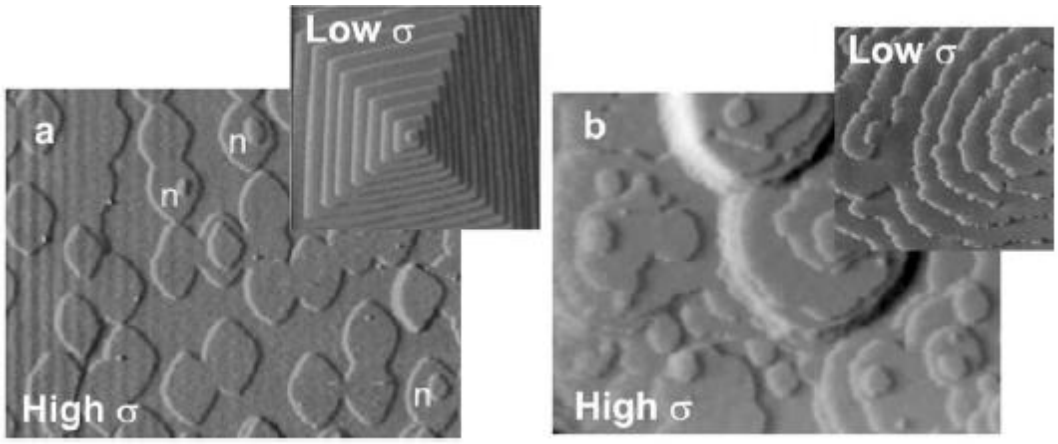

Figure 8: Layer growth in calcite and canavalin. (A) Calcite and (B) canavalin crystals grow from screw dislocations at low supersaturations σ and transition to layer-by-layer growth via 2-dimensional nucleation at higher σ[25].

As molecules adsorb on the terraces, they encounter each other due to collisions and probability dictates that with random collisions enough molecules come together thus overcoming the free energy barrier to form the critical radius. This barrier is directly proportional to the supersaturation. Higher supersaturation leads to lower critical radius. A nucleus of the critical radius has 50:50 probability of dissolving or growing. When the size exceeds R_{crit}, the layers will spread until it reaches the crystal edges, thus faceting the crystals. Crystals that grow via classical mechanisms grow tangentially to each face layer-by-layer and are facetted by the slowest growing face. These parameters giving rise to their characteristic habit, which is the size, shape, and overall morphology.

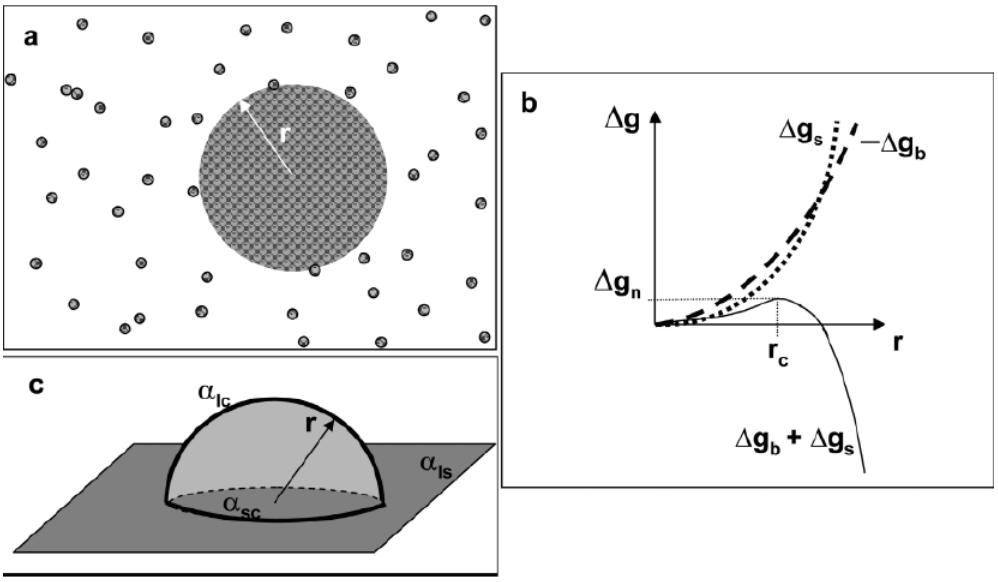

Figure 9: Nucleation. (a) Formation of a spherical nucleus of radius r from solution leads to the free energy changes shown in (b). The cross-over of the bulk and surface energy terms with their opposite signs leads to a free energy barrier. (c) Heterogeneous nucleus formation on a foreign substrate[25].

1.2.4. Non-classical Crystallization

Recently a lot of work has been done identifying growth units larger and more complicated than monomers comprising the non-classical growth mechanism.

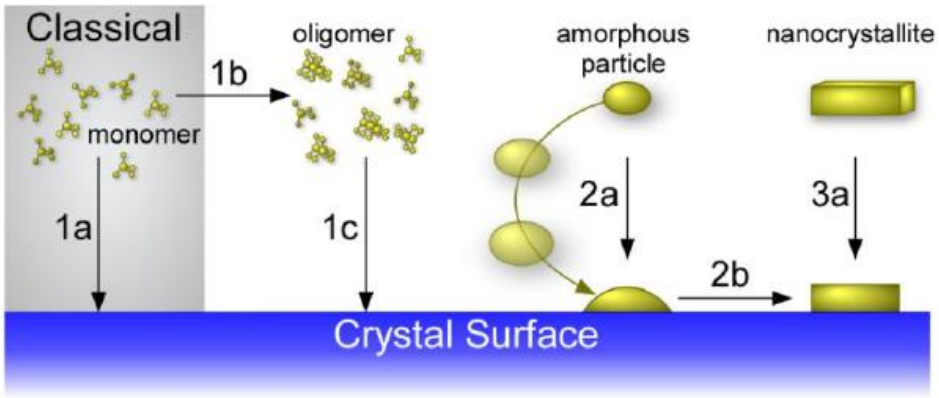

Figure 10: Solute addition via non-classical pathways. (1b) Oligomer formation, (2a) amorphous particle addition and (3c) nanocrystalline material addition[50].

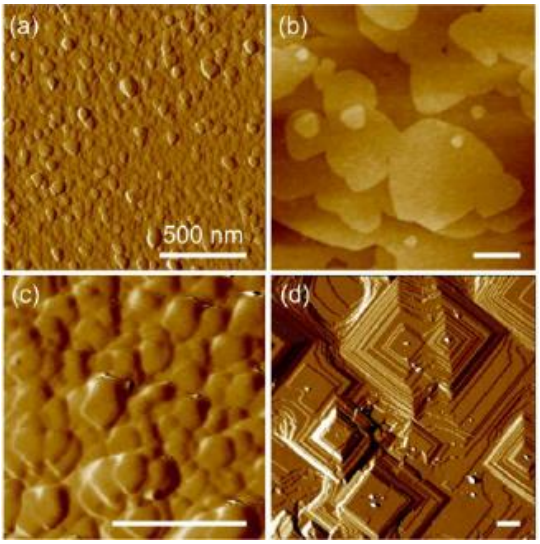

Figure 11: AFM images showing nonclassical (left column; A and C) and classical (right column; B and D) growth. (a) and (b) Sillicate-1[59] while (c) and (d) SSZ-13[60]. Scale bars equal to 500 nm.

The high level of complexity involved in non-classical growth modes can be seen in zeolite crystallization. AFM studies on zeolite crystals show dual growth modes at various stages of crystallization (figure 11a). At high supersaturations surfaces of zeolite crystals appear rough due to primary particle deposits that evolve into 3D layers made of macrosteps (figure 11c). When crystals are removed from growth solution after several days of hydrothermal treatment the crystal surface contains layers with step heights comparable to unit cell dimensions (figure 11 b and d). This suggests that at the final stage of crystallization, at low supersaturations growth is dominated by classical 2D or screw dislocation layer growth.

1.2.5. Crystal growth modifiers

In classical crystallization, the effect of modifiers can be explained by type of species attachment and the location on the crystal surface. There are three proposed mechanisms for types of inhibition based on the type of species attachment (Figure 10): (i) the solute could form a complex with the inhibitor and block crystal growth by binding to the surface;

(ii) a solute/inhibitor complex does not bind the crystal surface, altering the degree of supersaturation slowing growth; and (iii) the inhibitor could bind directly to the crystal surface causing inhibition.

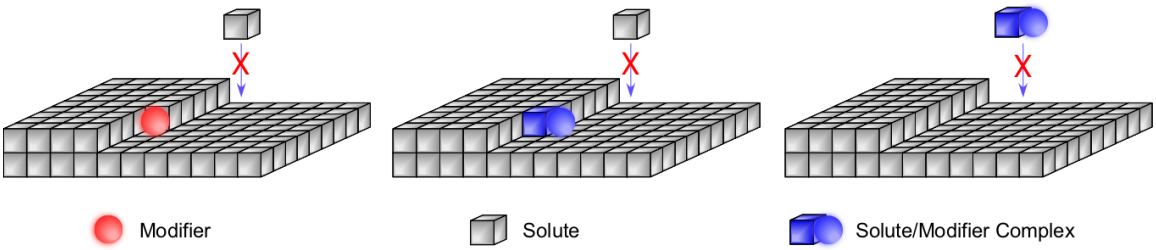

Figure 12: Inhibition mechanism based on the type of species attachment to the kink.

On the crystal surface, modifiers can bind to kinks, steps and terraces. In the step pinning mechanism, modifiers attach to crystal terraces and impede further propagation of steps. As steps advance and chance upon a modifier on a terrace, the step velocity decreases due to strain imposed. If two or more modifiers are spaced on a terrace close enough, the step propagation will be fully arrested as seen in Figure 11a. For kink blocking mechanism, modifiers bind to kink sites on the crystal surface shown in Figure 11b. This attachment decreases step velocity due to blocking the most energetically favorable site for monomer addition. Depending on the concentration of modifier attachment to kinks, step advancement can be fully suppressed or significantly reduced.

Larger modifiers can cause macro-step induction or bridging. In this case, the modifier binds to a step edge and the terrace above the step. This causes macro-steps to form and step velocity to decline.

Another mechanism, shown in Figure 11c-d, behaves similar to the kink blocking mechanism, but can cause dissolution of crystal surfaces under certain conditions by inducing localized strain. This mode of action is not fully resolved yet and only works for specific range of concentrations; if the concentration is too low or high, it will revert to

kink blocking or competitive attachment/detachment of monomers leading to non-uniform attachment and disappearance of distinct layers, respectively.

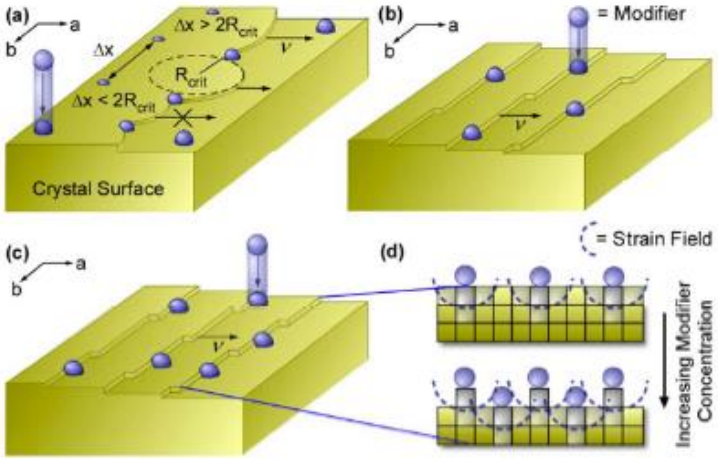

Figure 13: Modes of classical crystallization inhibition. (a) step-pinning, (b) kink blocking and (c-d) strain induced dissolution[50].

1.2.6 Inhibition of Non-classical Crystallization

In nonclassical crystallization, there are no specific crystal surface binding sites for modifier attachment. However, modifiers can alter monomer, oligomer or precursor attachment, speciation reactions, self-assembly of amorphous particles and structural evolution of precursors. On the surface, the transition from disordered to ordered can also be hindered. The modifier can complex with oligomers in solution or stabilize precursors to prevent aggregation and attachment to crystal surfaces. Overall, for nonclassical crystallization, there are a plethora of pathways for inhibition.

Chapter 2: Crystallization of Porphyrins

2.1 Organic Crystallization

In recent years, organic liquids have been recruited as alternative solvents for preparation of crystalline materials and separation or purification by crystallization,[61,62] in particular for high-value materials such as pharmaceuticals and fine chemicals.[63-65] Crystallization has been the most important separation and purification process in the pharmaceutical industry throughout its history. In contrast to crystallization from aqueous solvents, the level of understanding of the fundamental processes of crystal growth from organic solvents is severely limited.[66-68] In most cases, optimization of the growth processes is carried out by trial-and-error or by mimicking pathways developed for other compounds.[63] The lack of insight into the relevant fundamental mechanisms has emerged as a major obstacle to a rational approach to optimize and control organic crystallization.[17] Many parallels exist in the fine chemicals industry also. Over the past several decades the study of crystallization operations has taken on increasing levels of importance because of several factors that require effective control of crystallization processes. These levels of control require better understanding of the complex interactions of nucleation and growth as well as the operating characteristics of crystallization equipment including the critical issue of scale-up. In the pharmaceutical industry, the issue of better control, desirable in and of itself, is reinforced by the need to satisfy both company internal and governmental regulatory authorities on the consistency of chemical and physical properties of active pharmaceutical ingredients (APIs). Control of crystallization operations and choice of solvents are thereby critical. Aqueous crystallization results in the formation of 3-D hydrogen network at the crystal-solution interface[65,68,69]. These structured solvent layers at

the crystal interface results in complex interactions between the incoming solute and the structured solvent layers at the interface. The incoming solute molecules need to remove the structured solvent at the crystal interface for incorporation. Additionally in natural and in synthetic crystallization, soluble foreign compounds that interact with the solute or the crystal-solution interface are deployed to promote or inhibit crystallization[50]. Nature achieves remarkable diversity of shapes, patterns, compositions, and functions of the arising crystalline structures by applying ingredients that control the number of nucleated crystals and their anisotropic rates of growth[38,61,70-72].

Most data on how modifiers impact crystal growth derives from experiments in aqueous solutions. Recently, organic liquids have been used extensively as alternative solvents for preparation of crystalline materials and separation or purification by crystallization,[61,62] in particular for high-value materials such as pharmaceuticals and organic semi-conductors.[63-65] Physiological crystallization, such as the accumulation of cholesterol crystals in arterial walls,[73] often selects lipid environments. The interactions of an organic solvent with the solute and modifier and the contacts between solute and modifier molecules are largely constrained to van der Waals forces and may drastically diverge from those operating in water-based solutions, where H-bonding dominates.[74-77] The disparity in the interactions that regulate the molecular-level structures and dynamics in organic crystallization may mobilize distinct operating mechanisms. In contrast to aqueous solvents, the level of understanding of the fundamental processes of crystal growth from organic solvents is severely limited.[66-68] In most cases, optimization of the growth processes is carried out by trial-and-error or by mimicking practices developed for other compounds.[63] The lack of insight into the fundamental mechanisms of how foreign

compounds modify the molecular pathways of crystallization has emerged as a major obstacle to a rational approach to optimize and control organic crystallization.[17]

2.2 Porphyrins

Porphyrins are a group of heterocyclic macrocycle organic compounds, composed of four modified pyrrole subunits interconnected at their α carbon atoms via methine bridges (=CH−). The parent of porphyrin is porphine, a rare chemical compound exclusively used for research and theorical study. Substituted porphines are called porphyrins, with a total of 26 π-electrons, of which 18 π-electrons form a planar, continuous cycle, the porphyrin ring structure is often described as aromatic[78]. One result of the large conjugated system is that porphyrins typically absorb strongly in the visible region of the electromagnetic spectrum, i.e. they are deeply colored. The name "porphyrin" derives from the Greek word *porphyra*, meaning *purple*[78].

Metal complexes derived from porphyrins occur naturally. One of the best-known families of porphyrin complexes is heme, the pigment in red blood cells, a cofactor of the protein hemoglobin.

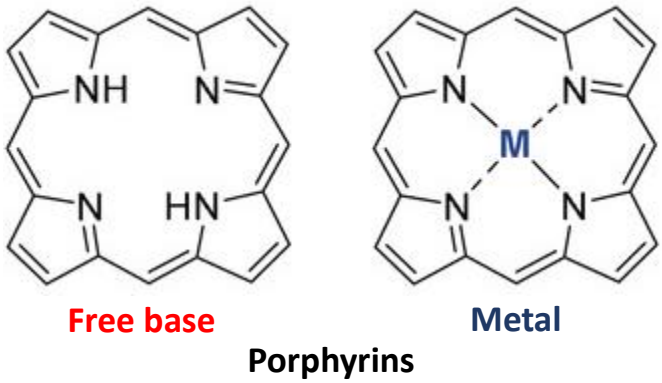

Figure 14: Ring structure of a parent porphine. A. Free base porphyrin and a metal coordinated porphyrin.

The porphyrins (Fig. 2.1) are an important class of naturally occurring macrocyclic compounds found in biological compounds that play a very important role in the

metabolism of living organisms. They have a universal biological distribution and were involved in the oldest metabolic phenomena on earth. Some of the best examples are the iron-containing porphyrins found as heme [52](of hemoglobin) and the magnesium-containing porphyrin found in chlorophyll[79]. Without porphyrins and their relative compounds, life as we know would be impossible and therefore the knowledge of these systems and their excited states is essential in understanding a wide variety of biological processes, including oxygen binding, electron transfer, catalysis, and photosynthesis. The porphyrins have attracted considerable attention because are ubiquitous in natural systems and have prospective applications in mimicking enzymes[80], catalytic reactions[81], photodynamic therapy[82], molecular electronic devices[83], and conversion of solar energy. Several porphyrins based artificial light-harvesting antennae, and donor acceptor dyads and triads have been prepared and tested to improve our understanding of the photochemical aspect of natural photosynthesis. The porphyrins play important roles in the nature, due to their special absorption, emission, charge transfer and complexing properties as a result of their characteristic ring structure of conjugated double bonds[84]. The absorbance spectra of porphyrins exhibit extreme intense bands, the so-called Soret or B-bands in the 380–500 nm and at longer wavelengths, in the 500–750-nm range, their spectra contain a set of weaker, but still considerably intense Q bands. Metalloporphyrins can be utilized in artificial photosynthetic systems, modelling the most important function of the green plants[85]. The studies of the wavelength shift of their adsorption band and the absorbance changes as function of pH, temperature, solvent change, reaction with metal ions and other parameters permits to obtained accurate information about equilibrium, complexation, kinetic and aggregation of porphyrins.

2.3 UV-Vis Spectrum of Porphyrins

The intensity and color of porphyrins are derived from the highly conjugated π-electron systems and the most fascinating feature of porphyrins is their characteristic UV-visible spectra that consist of two distinct region regions: in the near ultraviolet and in the visible region. It has been well documented that changes in the conjugation pathway and symmetry of a porphyrin can affect its UV/Vis absorption spectrum[86-88]. The absorption spectrum of porphyrins has long been understood in terms of the highly successful "four-orbital" (two highest occupied π orbitals and two lowest unoccupied π* orbitals) model first applied in 1959 by Martin Gouterman that has discussed the importance of charge localization on electronic spectroscopic properties and has proposed the four orbital model in the 1960s to explain the absorption spectra of porphyrins[89-91].

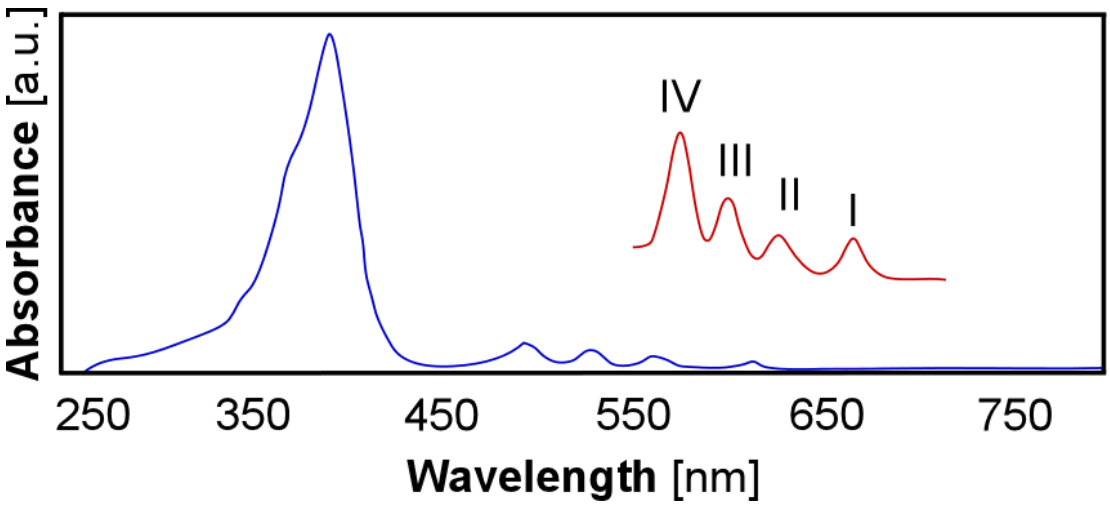

Figure 15: The electronic absorption spectra of free base porphyrins. The Uv-vis spectra shows the soret band at 400 nm and four q bands at higher wavelengths.

According to this theory, the absorption bands in porphyrin systems arise from transitions between two HOMOs and two LUMOs, and it is the identities of the metal center and the substituents on the ring that affect the relative energies of these transitions.

The HOMOs were calculated to be an a_{1u} and an a_{2u} orbital, while the LUMOs were calculated to be a degenerate set of e_g orbitals (figure 2.3). Transitions between these orbitals gave rise to two excited states. Orbital mixing splits these two states in energy, creating a higher energy state with greater oscillator strength, giving rise to the Soret or B band, and a lower energy state with less oscillator strength, giving rise to the Q-bands.

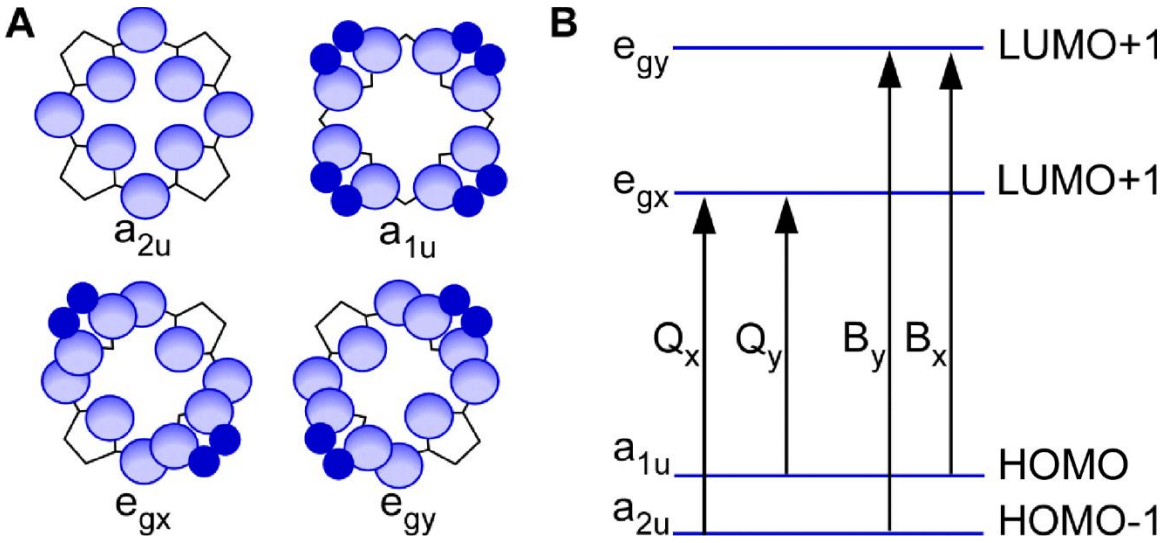

Figure 16: Porphyrin HOMO and LUMOs. A. Representation of the four Gouterman orbitals in porphyrins. B. Schematic representation of the energy levels of the four Gouterman orbitals upon symmetry lower from D4*h* to C2V. The sets of e_g orbitals gives rise to Q and B bands[90].

The electronic absorption spectrum of a typical porphyrin consists therefore of two distinct regions. The first involve the transition from the ground state to the second excited state (Figure2.2 and 2.3), the corresponding band is called the Soret band, where the range of absorption is between 380-500 nm depending on whether the porphyrin is β- or meso-substituted. The second region consists of a weak transition to the first excited state in the range between 500-750 nm (the Q bands). These favorable spectroscopic features of porphyrins are due to the conjugation of 18 π- electrons and provide the advantage of easy and precise monitoring of interaction with other molecules. The relative intensity of Q

bands is due to the kind and the position of substituents on the macrocycle ring. Based on the substituents, porphyrins could be classified as *etio, rhodo, oxo-rhodo e phyllo* [92]. When the relative intensities of Q bands are such that IV > III > II > I, the spectrum is said etio-type and porphyrins called etioporphyrins. This kind of spectrum is found in all porphyrins in which six or more of the β-positions are substituted with groups without π- electrons, e.g., alkyl groups. Substituent with π-electrons, as carbonyl or vinyl groups, attached directly to the β-positions gave a change in the relative intensities of the Q bands, such that III > IV > II > I. This is called rhodo-type spectrum (rhodoporphyrin) because these groups have a "reddening" effect on the spectrum by shifting it to longer wavelengths. On the other hand, when mesopositions are occupied, the phyllo-type spectrum is obtained, in which the intensity of Q bands is IV > II > III > I. While variations of the peripheral substituents on the porphyrin ring often cause minor changes to the intensity and wavelength of the absorption features, protonation of two of the inner nitrogen atoms or the insertion/change of metal atoms into the macrocycle strongly change the visible absorption spectrum.

Neglecting the overall charge of the macrocycle, a monomeric free-base porphyrin H_2-P in aqueous solution can add protons to produce mono H_3-P^+ and dications H_4-P^{2+} at very low pHs, or lose protons to form the centrally monoprotic H-P^- at pH about 6 or aprotic P^{2-} species at pH ≥ 10. These chemical forms of porphyrin may exist in equilibrium, depending upon the pH of the solution and can be characterized from the change of the electronic absorption spectrum. The change in spectra upon addition of acid or basic substances can generally be attributed to the attachment or the loss of protons to the two imino nitrogen atoms of the pyrrolenine-like ring in the free-base.

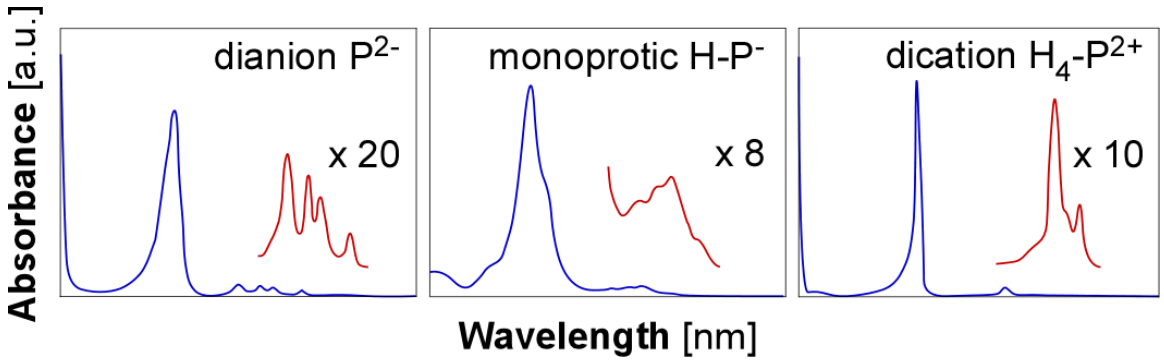

Figure 17: Absorption spectra of protonated free base porphyrins.

Spectrophotometric titration was employed for determining the acid dissociation constants over the inter pH range and change in absorbance with pH can be attributed to the following acid dissociation reactions of porphyrins. Upon addition of acid the spectral pattern of porphyrins changes from the four Q-band spectrum, indicating D2h symmetry for free-base porphine, to a two Q-band spectrum for the formation of dications H_4-P^{2+} (Figure 2.4), indicating D4h symmetry, characteristic of porphyrin coordinated to a metal ion through the four N-heteronuclei. Self-assembly of porphyrin molecules via noncovalent interactions, such as π-π stacking, electrostatic interactions, H-bonding, coordination bonding and van der Waals forces produces well defined porphyrin nanocrystals with improved electronic and optical properties finding widespread applications in catalysis, nonlinear optics, sensors and photoelectronic devices. Solution crystallization of porphyrins by controlling the monomer concentration, temperature, pressure, additives, crystal growth modifier and solvent.

Chapter 3: Thermodynamics of Organic Crystallization

Solution crystallization is an essential element of myriad industrial, natural, and physiological processes.[17,18] Numerous chemical products and production intermediates are precipitated as crystals in thousands-of-ton quantities.[19] Crystal synthesis is a central step in pharmaceuticals manufacture since crystalline drugs offer the advantage of steady medication release rates that are maintained for longer periods than amorphous or solubilized formulations.[20-24] The grand challenge in the area is the control of the nucleation and growth of crystals of complex chemical compounds. Successful and versatile control strategies rest on understanding the fundamental thermodynamic and kinetic mechanisms of crystallization.[17]

Traditional crystallization procedures employ aqueous solutions where the corresponding mechanisms have been studied in detail at all relevant lengthscales: macroscopic, mesoscopic, and molecular. At the molecular lengthscale, a fundamental property of water to form a three-dimensional network of hydrogen bonds, molded around solute molecules and along the crystal surface, has been identified as a major factor that determines the thermodynamic and kinetic parameters of solute incorporation into growth sites[35,37-44] and, correspondingly, the pathways and the rates of crystallization from aqueous solvents.[45-48]

In recent years, organic liquids have been recruited as alternative solvents for preparation of crystalline materials and separation or purification by crystallization,[61,62] in particular for high-value materials such as pharmaceuticals and fine chemicals.[63-65] In contrast to crystallization from aqueous solvents, the level of understanding of the fundamental processes of crystal growth from organic solvents is severely limited.[66-68] In

most cases, optimization of the growth processes is carried out by trial-and-error or by mimicking pathways developed for other compounds.[63] The lack of insight into the relevant fundamental mechanisms has emerged as a major obstacle to a rational approach to optimize and control organic crystallization.[17]

It is likely that the processes occurring at macroscopic and mesoscopic lengthscales in organic solvents follow mechanisms similar to those found in aqueous solutions and can be understood by rescaling the solvent viscosity, solute diffusivity, and the surface free energy of the solution-crystal interface with those characteristic of the organic solution.[93] On the other hand, the processes occurring at the molecular lengthscale will likely not abide by similar rescaling laws.[69] In contrast to water, organic solvents may not erect networks that envelope the solute molecules and shield the crystal surfaces.[94] Understanding the molecular processes of organic solute incorporation into crystals requires definition of the spatial and energy attributes of the interactions between solute and solvent that supplant those mediated by structured water.[47,66-68,95]

Here we address the thermodynamic interactions that govern the dissolution of porphyrins in a line of organic solvents and drive their crystallization. We focus on etioporphyrin I, which consists of four pyrrole residues linked at positions 2 and 5 by methine groups to form a flat porphyrin ring; the porphyrin ring is decorated at positions 3 and 4 of the constituent pyrroles by alternating four ethyl and four methyl groups (Figure 18A). The conformational flexibility of the methyl and ethyl groups lowers the molecular symmetry from D_{2h} (or mmm) of porphyrin to C_1 (or 1). Single crystals of porphyrins and their metal derivatives mostly have low symmetries and find potential use as organic semiconductors, solar cells, and field-effect transistors due to their electronic and optical

properties.[8,96,97] We dissolve etioporphyrin in five solvents (Figure 18B): three alcohols, butyl, hexyl, and octanyl, with increasing alkyl chain length to gauge the importance of the interactions between nonpolar functional groups; dimethyl sulfoxide (DMSO), a small polar aprotic molecule with two short aliphatic residues to assess the function of its substantial dipole moment; and caprylic (octanoic) acid to probe if salt bridges form with the positively charged pyrrole nitrogens. We evaluate the significance of solute-solvent hydrogen bonds by using two alternative solutes, the variant porphyrins protoporphyrin IX and coproporphyrin I, which carry on the periphery of the porphyrin ring two or four, respectively, carboxyl groups that may hydrogen-bind to the alcohols.

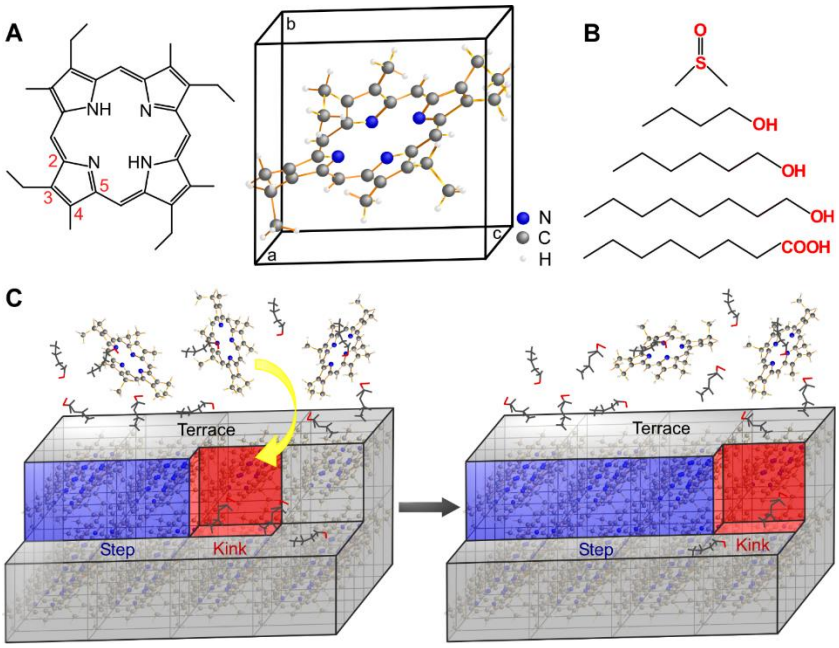

Figure 18: The structures of the etioporphyrin I, solvents, and crystals. A. The etioporphyrin I molecule and crystal structure in P1 space group; Cambridge Structural Database REFCODE WOBVUF[8]. **B.** The structures of the tested solvents, from top to bottom, DMSO, butanol, hexanol, octanol and caprylic acid. **C.** Schematic illustration of the incorporation of an etioporphyrin molecule from a solution into a kink on the crystal surface.

As a metric of the solute-solvent interactions we employ the relative enthalpies H_{soln} and entropies S_{soln} of etioporphyrin I solutions in the five solvents. We evaluate H_{soln} and

S_{soln} from the crystallization enthalpies ΔH^{o}_{cryst} and entropies ΔS^{o}_{cryst}. Analyses of H_{soln} and S_{soln} indicate that the solution thermodynamics are dominated by interactions between permanent dipoles, promoted by the dielectric constants of the solvents, which are substantially lower than that of water, and London dispersion forces between the nonpolar groups of the solute and solvent, which take the place of the hydrophobic bonds common in aqueous solutions.[98] Surprisingly, we find that both hydrogen bonds and salt bridges, which can potentially strongly ligate solvent to solute, contribute little to the solution thermodynamics.

3.1 Determination of Extinction Coefficients of Porphyrins

For solubility measurement it is imperative to determine concentration, for which we use uv-vis spectroscopy. Beer's Law relates the concentration dependence on absorbance, A= εCl, where ε is the extinction coefficient, *C* is the concentration and *l* absorbance path length. Calibration curves for extinction coefficient measurement were determined by measuring the absorbance of porphyrins in the organic solvents (shown in the inset of figures 19 and 20). Known amounts of etioporphyrin I was completely dissolved in the respective solvents thus solutions of known concentrations were made and absorbance was measured. Distinct Soret and q bands were visible for the free base porphyrins and merged q bands for the protonated coproporphyrin I. The extinction coefficients were determined in the listed values of wavelengths as shown in figure 19 and 20, the local maxima of the absorbance spectrum. Experiments were done in triplicates for repeatability and reproducibility. The determined values of extinction coefficients are listed in table 1 for the wavelengths mentioned which are local maxima of the absorption spectrum.

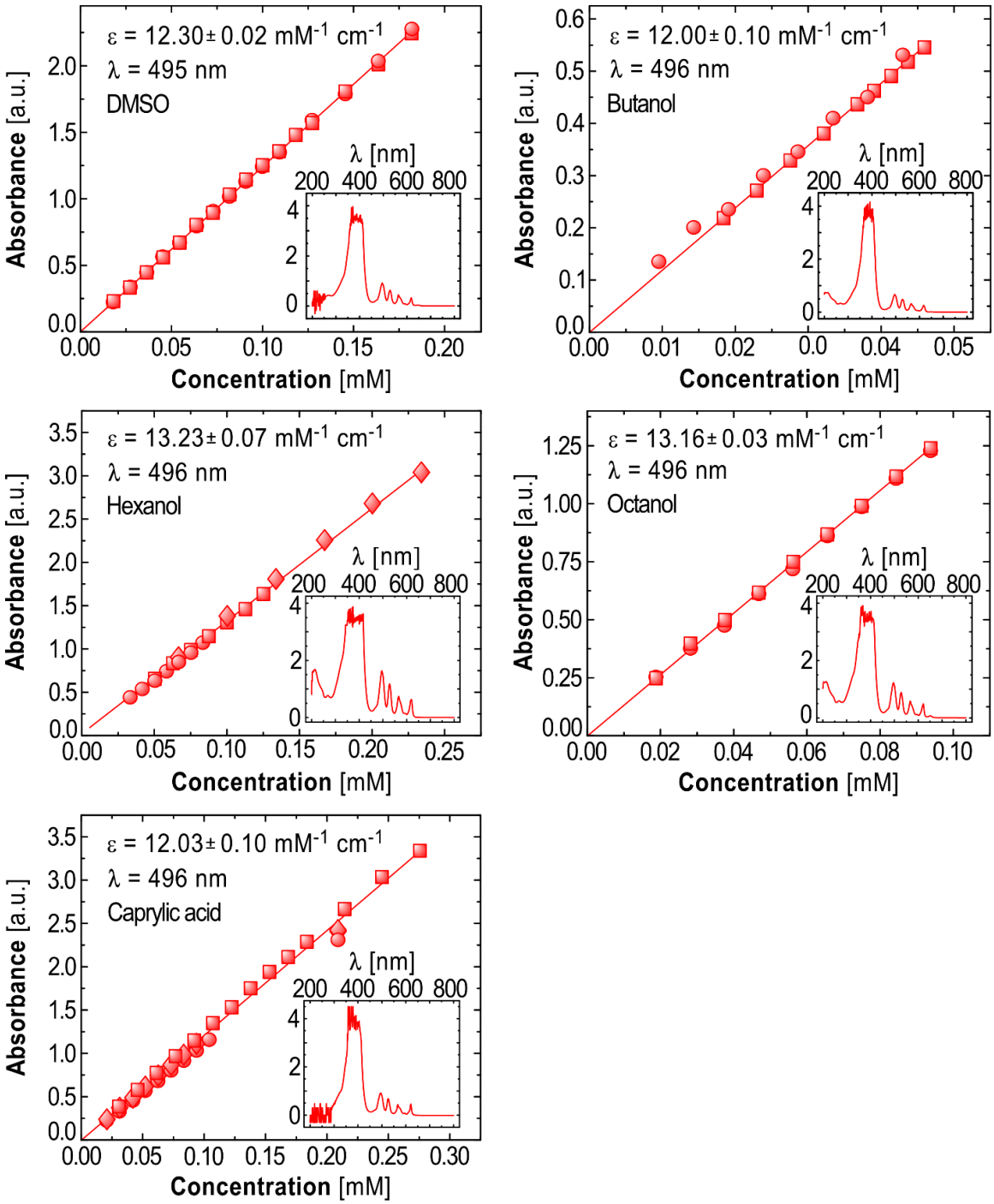

Figure 19: Determination of extinction coefficient of etioporphyrin I in organic solvents. The absorbance at a local maxima wavelength selected from the q bands of the spectra in the respective insets are plotted as a function of etioporphyrin I concentration. The corresponding extinction coefficient ε is listed in each plot. Individual experiments are indicated in different symbols. Solid lines represent linear regression fits.

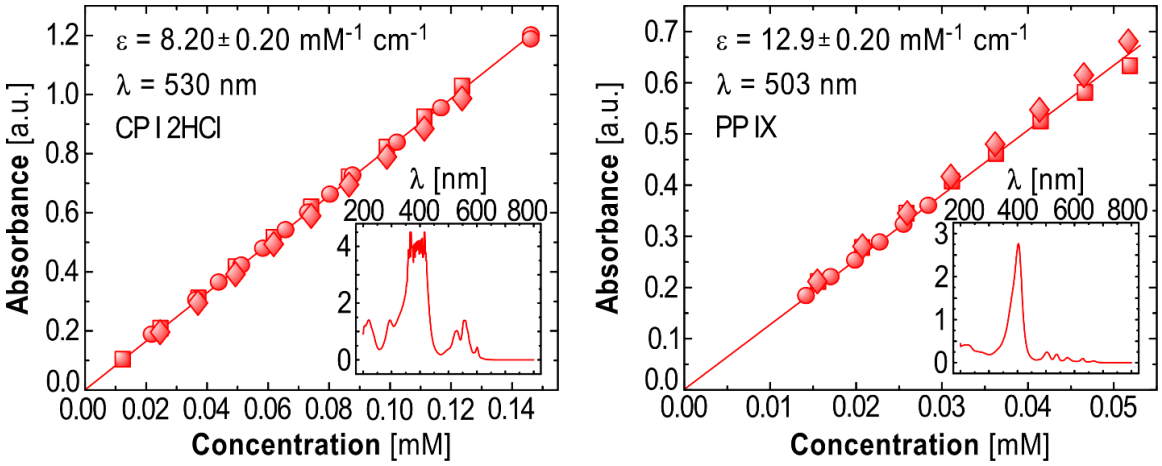

Figure 20: Determination of extinction coefficient of coproporphyrin I dihydrochloride and protoporphyrin IX in butanol. The absorbance at a local maxima wavelength selected from the q bands of the spectra in the respective insets are plotted as a function of the solute concentration. The corresponding extinction coefficient ε is listed in each plot. Solid lines represent linear regression fits.

Table 1. Extinction coefficient ε of porphyrins in organic solvents at wavelength λ of local maximum absorbance.

Compounds	DMSO	butanol	hexanol	octanol	caprylic acid
Etioporphyrin I	12.30 ± 0.02 (495 nm) 8.38 ± 0.01 (528 nm) 5.91 ± 0.01 (664 nm)	12.00 ± 0.10 (496 nm) 8.55 ± 0.10 (528 nm) 5.31 ± 0.10 (565 nm)	13.23 ± 0.07 (496 nm) 9.59 ± 0.05 (528 nm) 6.02 ± 0.03 (566 nm)	13.16 ± 0.03 (496 nm) 9.43 ± 0.10 (528 nm) 6.22 ± 0.10 (567 nm)	12.03 ± 0.10 (496 nm) 8.92 ± 0.05 (526 nm) 5.97 ± 0.04 (567 nm)
Coproporphyrin I dihydrochloride	12.62 ± 0.10 (496 nm)	8.20 ± 0.20 (530 nm)	--	8.35 ± 0.20 (530 nm)	--
Protoporphyrin IX	12.54 ± 0.20 (504 nm)	12.90 ± 0.20 (503 nm)	--	12.17 ± 0.10 (504 nm)	--

3.2 Quantification of the Solution-Crystal Equilibrium

The only entry for etioporphyrin I in the Cambridge Structural Database (CSD) is of unsolvated crystals that belong to the non-centrosymmetric P1 crystallographic symmetry group (Figure 18A).[8] The morphologies of the crystals grown from the five tested solvents divide into two groups: relatively isometric crystals that form in DMSO and elongated four-sided prisms that grow from the three alcohols and caprylic acid (Figure 21A). Powder x-ray diffraction spectra of the five crystal types reveal, however, that their structures are identical to that of the commercial stock and to the structure deposited in CSD (Figure 21B). The distinct morphology of DMSO-grown crystals reflects a unique anisotropy of the growth rates *R* in this solvent, whereby *R*s in different crystallographic directions are commensurate; by contrast, in the other four solvents, *R* in the axial direction substantially exceeds the *R*s in the lateral directions.

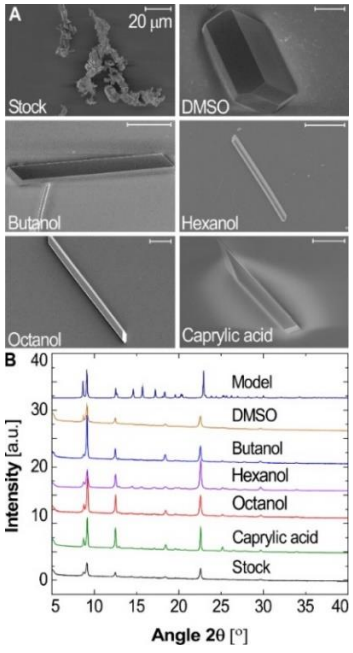

Figure 21: Structural identity of etioporphyrin I crystals grown from distinct solvents. A. Scanning electron micrographs of crystals grown in solvents listed in each panel and of the commercial stock. **B.** X-ray powder diffraction patterns of etioporphyrin I crystals grown in the five listed solvents.

Solute molecules integrate into a crystal exclusively at kinks, the end sites of unfinished molecular rows that terminate unfinished crystal planes of a growing crystal (Figure 18C).[99,100] In consequence, ΔH^o_{cryst} and ΔS^o_{cryst} characterize the equilibrium

Etioporphyrin I (solution) ⇌ etioporphyrin I (kink). (9)

Because etioporphyrin I crystallizes in the same polymorph from the five solvents that we test, the bonds that form in the kinks are identical, the enthalpy and entropy of etioporphyrin I in the crystals H_{cryst} and S_{cryst} are independent of the solvent, and the differences in $\Delta H^o_{cryst} = H_{cryst} - H_{soln}$ and $\Delta S^o_{cryst} = S_{cryst} - S_{soln}$ between solvents exactly mirror the differences between H_{soln} and S_{soln} of the solute in each solvent.

To relate ΔH^o_{cryst} and ΔS^o_{cryst} to a measurable property of the crystal – solution equilibrium, we use that in the two-phase system comprising crystals and a solution the total free energy effect $dG = dG^{cryst} + dG^{soln}$ of the transfer of dn_1 solvent molecules and dn_2 etioporphyrin I molecules from the solution to the crystal is

$$dG = dG^{cryst} + dG^{soln} = \boldsymbol{\mu_1^{cryst} dn_1^{cryst} + \mu_2^{cryst} dn_2^{cryst} + \mu_1^{soln} dn_1^{soln} + \mu_2^{soln} dn_2^{soln} = \mu_2^{cryst} dn_2^{cryst} + \mu_2^{soln} dn_2^{soln}} \quad . \tag{10}$$

The second equality in eq. (10) employs that etioporphyrin I crystals in all tested solvents are unsolvated and the solvent amount that transfers from the solution to a crystal $dn_1 = dn_1^{cryst} = -dn_1^{soln} = 0$. Since $dn_2^{cryst} = -dn_2^{soln} = dn_2$, then $dG = (\mu_2^{cryst} - \mu_2^{soln}) dn_2$. At equilibrium, $dG = 0$ and

$$\mu_2^{cryst} = \mu_2^{soln} = \mu_2^o + RTlna_{2,e}, \tag{11}$$

where μ_2^0 is the standard value of μ_2^{soln}, $a_{2,e}$ is the etioporphyrin I activity at equilibrium with its crystals, R is the universal gas constant, and T is temperature. Since μ_2^{cryst} is constant and independent of the solute concentration, $\mu_2^{cryst} = \mu_2^{cryst,o} = \mu_{2,e}^{cryst}$, and we rewrite eq. (11) as

$$\mu_2^{cryst,o} - \mu_2^0 = RTlna_{2,e}. \quad (12)$$

Since etioporphyrin is the only component that transitions between the solution and the crystals, $\mu_2^{cryst,o} - \mu_2^0 = \Delta G_{cryst}^o$, where ΔG_{cryst}^o is the molar free energy change of crystallization. We introduce the equilibrium constant for crystallization, $K_{eq} \equiv \exp\left(-\Delta G_{cryst}^o/RT\right)$ and combine this definition with eq. (12) to reach $K_{eq} = a_{2,e}^{-1}$. In all tested solvents and temperatures, the concentrations of etioporphyrin I were about 1 mM or less, at which the activity coefficients of the solute would be close to one and $a_{2,e} \approx C_e$, where C_e is the concentration of the etioporphyrin I solution at equilibrium with the respective crystals, also called solubility. We obtain

$$K_{eq} = C_e^{-1}. \quad (13)$$

Eq. (13) implies that we can describe the correlation between C_e and T using the van 't Hoff law

$$\frac{\partial \ln C_e}{\partial(1/T)} = \frac{\Delta H_{cryst}^o}{R}, \quad (14)$$

and determine ΔH_{cryst}^o from the slope of the correlation $\ln C_e(1/T)$. A second corollary of eq. (13) is that $\Delta G_{cryst}^o = RT \ln C_e$. We employ the values of ΔH_{cryst}^o and ΔG_{cryst}^o to

evaluate ΔS^o_{cryst}. The Gibbs-Helmholtz relation $\Delta S^o_{cryst} = (\Delta H^o_{cryst} - \Delta G^o_{cryst})/T$ reveals that ΔS^o_{cryst} presents as the intercept of the van 't Hoff correlations.[52,101,102]

Eqs. (13) and (14) indicate that ΔH^o_{cryst} and ΔS^o_{cryst} in individual solvents can be evaluated from data on the respective temperature dependence of etioporphyrin I solubility. In an alternative approach, the crystallization enthalpy ΔH^o_{cryst} can be determined by scaling the heat released during crystallization (measured by calorimetry at constant temperature and pressure) with the crystallized amount. The calorimetry determination may be distorted, however, by solution trapped between crystals and mislabeled as crystalline mass. Concurrent measurements of ΔH^o_{cryst} by both methods returned nearly identical heat effects and substantially higher experimental uncertainty of the calorimetry result.[103]

To determine the solubility, we hold vials with the respective solvents at several temperatures in the range 4°C to 45°C. We add crystals to the vials until a fraction of the added crystals remains undissolved and monitor the evolution of the concentration, which increases owing to ongoing dissolution. We view three successive concentration determinations that produce consistent results (Figure 22A) as indication that the solution has reached equilibrium with the crystals. The averaged value of the three concentrations is taken as the solubility. These determinations were

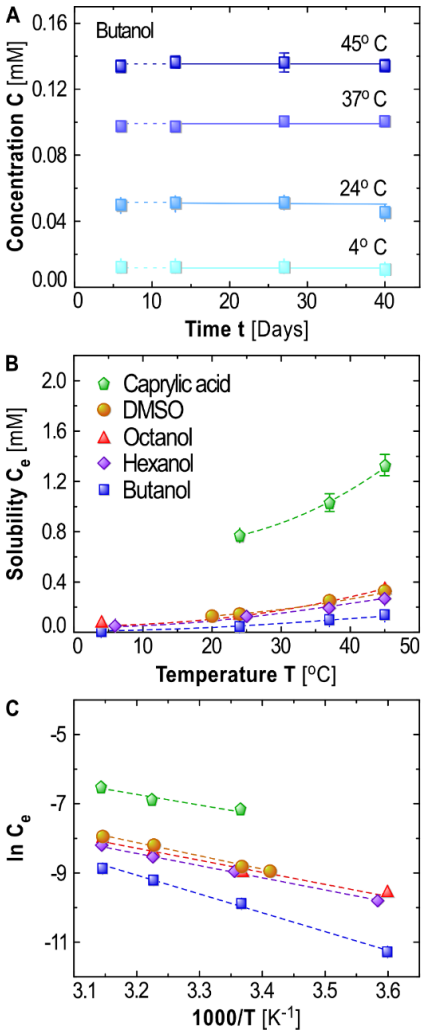

Figure 22: The equilibrium between etioporphyrin I in the solution and in the crystal. A. Evolution of etioporphyrin I concentration *C* in butanol at 4°C, 24°C, 37°C, and 45°C in the presence of excess crystals. *C* increases as the crystal dissolve. *C* saturates when it reaches its equilibrium value, the solubility C_e. Error bars represent the average of three independent determinations. **B.** Temperature dependence of solubility C_e of etioporphyrin I in five listed solvents. **C.** van 't Hoff coordinate plots of the solubility C_e of etioporphyrin I as a function of temperature *T* in the five listed solvents. Dashed lines in B and C depict the best-fit linear regressions to data in C.

carried out in triplicate for each solvent and at each temperature so that each solubility value is the result of averaging over nine concentrations. In the selected procedure, the solution approaches equilibrium with the crystals by dissolving crystalline matter, which has advantages over common techniques to determine solubility by monitoring the

decrease of the concentration of a supersaturated solution due to crystal growth. Crystals may cease to grow before equilibrium is reached owing to poisoning by impurities [104-106] or lack of new layer sources;[107] such growth cessation may exaggerate the solubility estimate up to two-fold. Kinetic obstacles to dissolution *en route* to equilibrium are rare owing to abundant supply of dissolving layers from the crystal edges.[108]

In all solvents, increasing temperature enforces higher solubility (Figure 22B), which indicates that the respective equilibriums shift towards the solution by partial dissolution of crystals. The Le Chatelier principle implies that crystallization in all solvents is exothermic (and crystal dissolution is endothermic) and all ΔH^o_{cryst} are negative. The $C_e(T)$ correlations in van 't Hoff coordinates, $\ln C_e(1/T)$ fit well straight lines (Figure 22C). This linearity indicates, according to eq. (14), that ΔH^o_{cryst} values for the five solvents are relatively constant in the tested temperature range. In keeping with the Le Chatelier's principle prediction, the slopes of the van 't Hoff correlations are negative (Figure 22C): eq. (14) reveals that the slopes' signs coincide with the signs of ΔH^o_{cryst}.

3.3 Contribution of Dipole-Dipole and Dispersion Interactions

The negative values of ΔH^o_{cryst} (Figure 23A) indicate that the enthalpies of the solutions are greater than the enthalpy of the etioporphyrin I P1 crystals and crystallization in the five tested solvents is driven by enthalpy. The relation $H_{soln} = H_{cryst} - \Delta H^o_{cryst}$ implies that in solvents, for which ΔH^o_{cryst} is algebraically high, the respective H_{soln} is low and manifests strong solute-solvent interactions (Figure 23C). The crystallization entropy ΔS^o_{cryst} is negative in all five solvents, between –5 and –60 J $mol^{-1}K^{-1}$, and implies that degrees of freedom are lost upon crystallization.

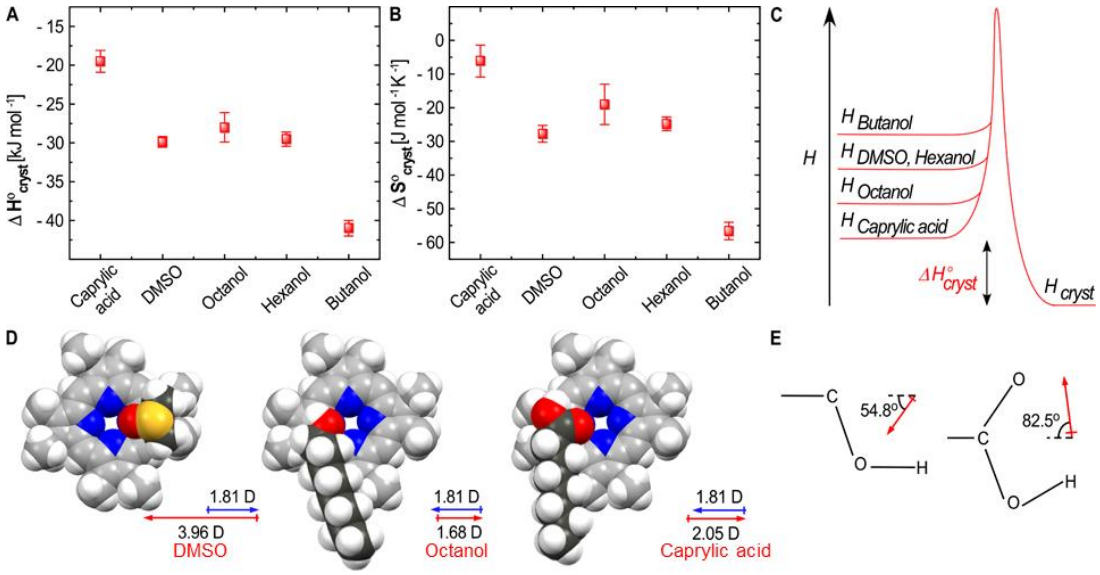

Figure 23: Thermodynamic parameters of etioporphyrin I crystallization in five solvents. **A.** The crystallization enthalpy ΔH^{o}_{cryst}. **B.** The crystallization entropy ΔS^{o}_{cryst}. **C**. Schematic representation of the enthalpy change along the reaction coordinate for crystallization. **D.** Schematics of the interactions of the dipole moment of a pyrrole group in etioporphyrin I with the dipole moments of DMSO, octanol, and caprylic acid. **E.** The orientation of the dipole moment of the hydroxyl group with respect to the C_α–C_β bond and of the carboxyl group with respect to the C–C_α bond.

(Figure 23B). The loss of six translational and rotational degrees of freedom, partially offset by the gain of newly created vibrational motions, due to the binding of a molecule of about 1 nm dimeter is characterized by $\Delta S \approx$ –100 to –120 J mol^{-1}K^{-1}.[109,110] In all tested solvents, ΔS^{o}_{cryst} is greater than this threshold revealing a partial gain of molecular freedom upon crystallization. This counterintuitive entropy gain likely reflects the release of solvent molecules coating the solute and lining the kinks as etioporphyrin I incorporates into a kink. ΔH^{o}_{cryst} and ΔS^{o}_{cryst} vary conformally between solvents and this consistency reflects the lower entropy of solvent molecules that strongly bind to the solute. The conformity between the ΔH^{o}_{cryst} and ΔS^{o}_{cryst} trends suggests that solvent-solvent interactions do not contribute to the thermodynamics of etioporphyrin I solutions and the solvent structuring

that they may support is weak. Indeed, solvent-solvent bonds that support several layers of solvent molecules structured around solutes, as in aqueous solutions,[111,112] would significantly increase the crystallization entropy owing to the release of the layered solvent upon incorporation into the crystal, but contribute little to the crystallization enthalpy since their energy is similar to that in the bulk solvent. Correspondingly, in aqueous and partially aqueous solutions, where water-water hydrogen bonds build up, this conformity is often violated.[101]

To correlate the values of ΔH^o_{cryst} and ΔS^o_{cryst} with the interaction between solute and solvent, we note that the UV-Vis spectra of etioporphyrin I in the five tested solvents (Figure S1) contain a prominent Soret band between 350 and 450 nm and four Q-band peaks in the 500-700 nm range, analogously to model spectra that assume etioporphyrin I in vacuum.[113] The similarity of the measured and model spectra in vacuum implies that the interactions between solvent and solute are weak and exclude exchanges of electron density that accompany salt bridges and hydrogen and covalent bonds.

ΔH^o_{cryst} of etioporphyrin I in DMSO is close to ΔH^o_{cryst} in octanol and hexanol (Figure 4A). DMSO carries two short methyl groups (Figure 18B), in contrast to longer alkyl chains of octanol and hexanol (Figure 18B), but it has a substantial dipole moment μ = 3.96 D (1 Debye = 3.336×10^{-30} Coulomb meters); the (Dipole moments) μs of octanol and hexanol are 1.66 and 1.60 D, respectively.[114,115] The similar ΔH^o_{cryst} values in the three solvents suggest that the polar groups and the aliphatic tails cooperate in the interactions that govern H_{soln} and ΔH^o_{cryst}. The polar groups of the solvents likely engage the pyrrole entities, in which the nitrogen accrues partial positive charge.[116] This charge distribution contrasts other five-membered heterocyclic compounds, furan and thiopene, where the

heteroatoms, O and S, respectively, charge negatively; pyrrole's odd charge distribution is attributed to the bias that its N-bound hydrogen imparts on the localization of π-electron density.[116] The pyrrole dipole moment points along the axis of the heterocycle[116] and orients the dipole moments of the sulfinyl and hydroxyl groups against itself. The dipole moment of DMSO is directed from a positive S to a negative O and interaction with the pyrrole dipole steers the O atom to the vicinity of the pyrrole N and the two methyl groups near C2, C3 and C4, C5, respectively (Figure 23D). The negative pole of the hydroxyl groups is anchored on the oxygen and the dipole moment points roughly along the bisectrix of the HCO angle (Figure 23E). Aligning the dipole moments of the alcohols with that of pyrrole directs their alkane chains towards the methine group that links two pyrrole cores (Figure 18D) and the nonpolar sites of an adjacent pyrrole (Figure 23D). This orientation of the alcohols with respect to etioporphyrin I allows robust interaction of the alcohol alkyl chains with the non-polar groups of the porphyrin ring.

The contribution of this dispersion interaction of the alcohols' alkane tails with the non-polar groups of the porphyrin ring is highlighted by the low ΔH^o_{cryst} and high H_{soln} in butanol (Figure 23A,C). The high H_{soln} in butanol manifests weak solute-solvent interaction due to an alkane tail shorter than those of octanol and hexanol, while its dipole moment, 1.66 D,[114,115] is close to those of the other two alcohols.

3.4 Contribution of Salt Bridges to the Solution Thermodynamics

Caprylic acid hosts the highest etioporphyrin I solubility (Figure 22B) testifying to solute –solvent interactions stronger than of the other four solvents. Accordingly, ΔH^o_{cryst} and S^o_{cryst} are highest (Figure 23A,B), and the related H_{soln}, lowest (Figure 23C). The propensity of the carboxyl group of caprylic acid to donate its proton advocates that proton

transfer from caprylic acid to etioporphyrin generates protonated porphyrin nitrogens and negative caprylate ions that bind in strong salt bridges. This hypothesis is refuted by the UV-vis absorption spectrum of etioporphyrin I dissolved in caprylic acid (Figure 24A), which shows intact Q bands of the solute. Protonation of two of the pyrrole nitrogens (Figure 24B, protonation of only one of them is rare[84,117,118]) in acidic environments invokes significant distortion and often merging of the porphyrin Q bands.[84,117,118] Indeed, the spectra of etioporphyrin I in acetic acid exhibit merged Q bands (Figure 24A), likely due to protonated nitrogens that are stabilized by the higher dielectric contact of acetic acid, 6.2, in contrast to 2.5 of caprylic acid; the acidities of the two acids, judged from their pK_as in water, 4.85 and 4.89, respectively, are very close.

As a consequence of this spectral shift, the color of etioporphyrin solutions in acetic acid is pink (close to the purple color that gave metal-liganded porphyrins their name)[84], whereas in caprylic acid and all other solvents it is brown (Figure 24C). Solvent-dependent color variations, known as solvatochromism, are a sensitive indicator of specific and non-specific solute-solvent interactions.[119] The color of etioporphyrin I solutions affords an additional opportunity to gauge the strength of solute-solvent interaction.

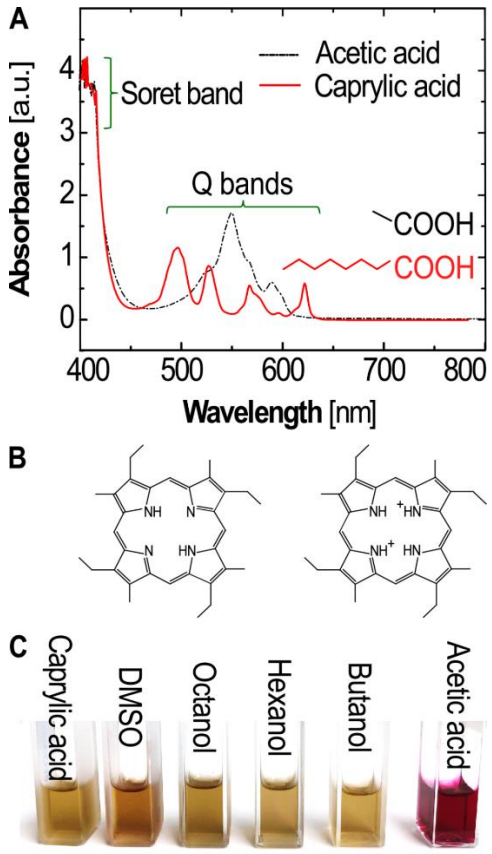

Figure 24: Binding of caprylic acid to etioporphyrin I. A. UV-vis absorption spectra of etioporphyrin I dissolved in pure acetic and caprylic acids; the Soret and Q bands are highlighted. **B.** Deprotonated and di-protonated forms of etioporphyrin I. **C** The distinct colors of etioporphyrin I solutions in the listed solvents.

The consistency of the solution color and the similarity of the UV-vis spectra of etioporphyrin I in the five solvents (Figures 24A, C and 19) signify that the interactions of etioporphyrin I with caprylic acids match those with the alcohols and DMSO and comprise dipole-dipole and dispersion forces. The dipole moment of monomeric caprylic acid, 2.05 D[120] (lower measured values in the literature[115] have been attributed to dimerization to a less polar dimer held by reciprocal hydrogen bonds between the constituent carboxyl groups[120,121]), is smaller than that of DMSO, 3.96 D.[115] If we assume that the caprylic acid dipole orients as in formic acid, it would form an angle of 82.5° with the carboxyl C – C_α

bond[122] and the negative pole would point towards the carbonyl O (Figure 4E). Aligning this dipole against the pyrrole dipole would direct the alkyl chain roughly perpendicular the pyrrole axis and empower abundant contacts with the methine groups of the porphyrin ring and the ethyl and methyl side chains. (Figure 23D). The caprylic alkyl chain is comparable to that of octanol and its substantial dispersion interaction with the non-polar groups of etioporphyrin I contributes to the strong affinity of the solute to this solvent.

3.5 The Small Contribution of H-Bonds

Etioporphyrin I does not afford the opportunity to weigh the significance of hydrogen bonds between solvent and solute for the solution thermodynamics since its only polar groups, the pyrrole nitrogens, carry a partial positive charge and deflect solvent protons.[116] For these tests, we employed two additional metal-free porphyrins, protoporphyrin IX and coproporphyrin I. In protoporphyrin IX, two of the ethyl groups of etioporphyrin I are replaced with propionic residues and the other two, with vinyl; the locations where these four entities attach to the porphyrin ring differ from those in etioporphyrin I (Figure 25A). Protoporphyrin IX represents the demetallated form of heme, the prosthetic group of hemoglobin and other proteins.[123] In coproporphyrin I all four ethyl groups are substituted with propionates and the sequence methyl, propionate is analogous to the sequence methyl, ethyl in etioporphyrin I (Figure 25A); coproporphyrin I precipitates as a HCl salt. The crystals of protoporphyrin IX arrange as spherulites of flat plates, whereas those of coproporphyrin I hydrochloride present well separated needles (Figure 25B). No CSD entries have been deposited for any of these two porphyrins. In consequence, the X-ray powder diffraction spectra of the respective crystal forms (Figure 25C) fail to identify the crystal structures.

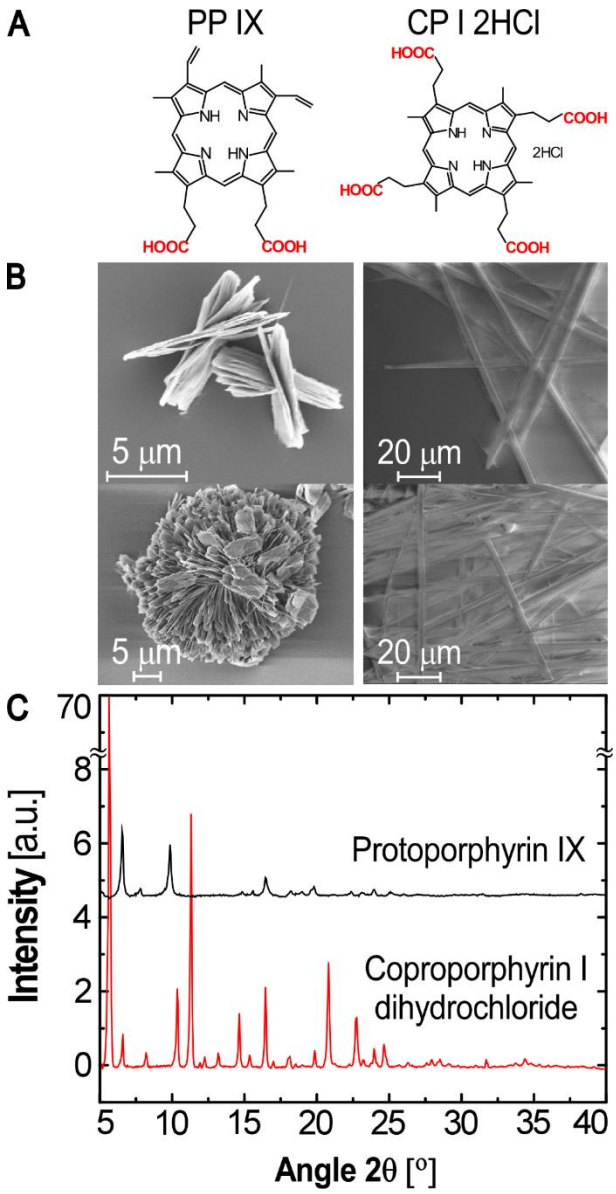

Figure 25: Crystallization of polar porphyrins from butanol. A. The structures of protoporphyrin IX (PP IX) and coproporphyrin I dihydrochloride (CP I 2HCl). **B.** Scanning electron microscopy (SEM) micrographs of PP IX (left) and CP I 2HCl (right) crystals grown from butanol **C.** Powder X-ray diffraction patterns of protoporphyrin IX and coproporphyrin I dihydrochloride crystals grown from butanol.

We expect that hydrogen bonds between the propionic groups of protoporphyrin IX and coproporphyrin I and the hydroxyl hydrogen of the solvent, butanol, would stabilize the solution and enforce low H_{soln} and high ΔH^{o}_{cryst}. In contrast to these expectations, the

enthalpy and entropy of crystallization of these two solutes in butanol are much lower than the respective values for etioporphyrin I (Figure 26A, B). The measurements of ΔH^{o}_{cryst} and ΔS^{o}_{cryst} submit that the thermodynamics of these two solutions are dictated by weak interactions, which exclude hydrogen bonds. The affinity to butanol of protoporphyrin IX and coproporphyrin I is weaker than that of etioporphyrin I suggesting that the propionic groups of the two acidic porphyrins, besides rejecting hydrogen bonding with the solvent hydroxyls, also impair the contacts between the butanol chain and the non-polar entities of porphyrin ring, which comprise a major part of the interaction of etioporphyrin I with butanol.

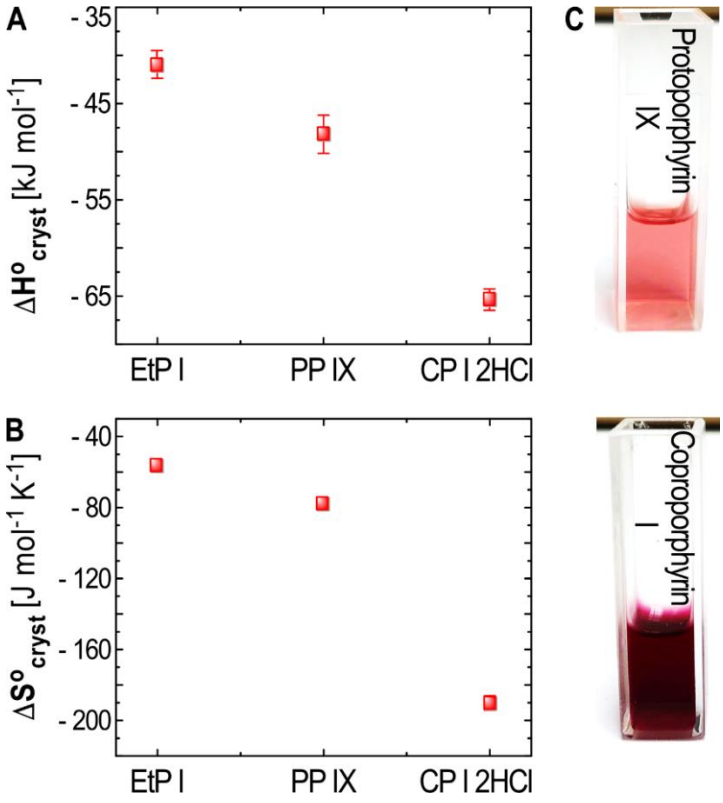

Figure 26: Thermodynamic parameters of crystallization of etioporphyrin I (EtP I), protoporphyrin IX (PP IX), and coproporphyrin I (CPI2HCl) from butanol. A. The crystallization enthalpy ΔH°_{cryst}. **B.** The crystallization entropy ΔS°_{cryst}. The error bars represent standard deviation of the slope and intercept of respective van 't Hoff plots. **C.** The color of solutions of protoporphyrin IX and coproporphyrin I in butanol.

The UV-vis spectra of this solution reveal four distinct Q-bands shifted to higher wavelengths (Figure S2) and promote the notion that protoporphyrin IX experiences dipole-dipole and dispersion interactions with butanol similar to those of etioporphyrin I. The persistence of the Q bands appears to contradict the pale red color of protoporphyrin IX solutions in butanol (Figure 26C), a manifestation of protonated pyrrole nitrogens.[84,117,118] We put forth that only a fraction of the protoporphyrin IX molecules are protonated and their red hue overpowers the brown color of the unprotonated majority that delivers the spectroscopic response. The likely proton donors are the own propionic groups of a protoporphyrin IX molecule; at the low solutions concentrations encounters with other protoporphyrin IX molecules may be rare. The intramolecular propionate – pyrrole salt bridges may be sustained by the high dielectric constant of butanol, about 18,[124] which substantially lowers the electrostatic potential of the constituent charged groups.

Dissolving coproporphyrin I dichloride in butanol colors the solution crimson and engenders a spectrum with merged Q bands shifted to the green range between 500 and 600 nm (Figure 19). The intense solution color and the Q bands shift indicate protonation of the pyrrole nitrogens, likely by protons from the co-solute HCl. HCl attaches to coproporphyrin I both in the solution and in the crystals and, in consequence, the interaction between the two co-solutes does not impact the low ΔH°_{cryst} and ΔS°_{cryst} (Figure 26A,B), dominated by the weak interactions with butanol.

3.6 Inference

To define the thermodynamic mechanisms that govern the dissolution of porphyrins in a line of organic solvents and drive their crystallization we combine determinations of the enthalpy and entropy of crystallization with molecular spectroscopy of the solutions and x-

ray and electron microcopy characterization of the crystal phases. We demonstrate that the thermodynamic parameters of crystallization can be faithfully evaluated from the temperature variations of the solubility.

We show that the weak propensity of the tested solvents to form solvent-solvent hydrogen bonds restricts the buildup of structured solvent around the solute molecules and along the crystal interface. The missing solvent structures stand in direct contrast with the three-dimensional network of hydrogen-bonded waters that wraps around solute molecules, coats the crystal surface, and dominates the thermodynamic and kinetic parameters of crystallization from aqueous solvents. In aqueous-based crystallization, the kinetic barrier assumes values in the range 25 – 35 kJ mol for a wide range of materials: from small ionic compounds, through organics, to proteins and viral particles.[47] This consistency has been attributed to the need to break the water structures as a solute molecules incorporates into a kink.[47] This finding of weak structuring of organic solvents promotes two fundamental predictions: First, that the activation energy for incorporation of solute molecules into organic crystals will be substantially lower than the value of about 30 kJ mol^{-1} found for aqueous crystallization,[47,125] and, second, that distinct solutes will exhibit disparate activation energies owing to the individual solute-solvent interactions. A third, more applied, corollary foresees that controlling crystal growth rate and its anisotropy by additives that erode solvent structures and suppress the activation energy for growth[126] may be less potent in organic crystallization.

We demonstrate that solution thermodynamics in the studied organic solvents are dominated by weak interactions between permanent dipoles and London dispersion forces between the nonpolar groups of the solute and solvent. We use an acidic solvent that

potentially could protonate a solute's basic group to demonstrate that salt bridges contribute insignificantly to the solution thermodynamics. We attribute the suppression of ionic pairs to the low dielectric constant of the tested solvents, which destabilizes charged groups by preserving their high Coulomb potential. Modifying the solute with carboxylic groups that may engage in solute-solvent hydrogen bonds unexpectedly strongly increases the solution enthalpy and demonstrates that solute-solvent hydrogen bonds do not form and the implanted acid groups impair the London dispersion interactions between the non-polar groups of the solute and solvent.

These insights may shepherd a rational approach to the search for organic solvents that lead to morphologies, sizes and number of organic crystals as demanded by their applications in electronics, optico-electronics, pharmacy, and chemical technology. Furthermore, the found preference for weak solute-solvent interactions and the exclusion of strong localized bonds may guide analytical and numerical models of nucleation and crystallization from organic solvents.

Chapter 4: Continuum of Solute Dimers Drives Distinct Growth Modes on Anisotropic Faces of Etioporphyrin I

One of the basic tenets of the classical theories of crystal nucleation and growth is the Szilard postulate[127,128], which states that molecules from the supersaturated phase join a nucleus or a growing crystal individually. Over the years, numerous crystals have been found to nucleate by assembly of monomers and grow by sequential association of monomers to growth sites. Recent experiments in bio- and geomimetic environments[49] have spotlighted a partial deviation from the Szilard rule, a bimodal distribution of growth species that arises from the assembly of ordered or amorphous particles[129-131].

Szilard formulated his postulate in the 1920s which claims that crystals only grow by association of monomers. The Szillard postulate is the most consequential assumption of the classical theories of crystal nucleation and growth and the basis of numerous theories that came after them which we use every day to model crystal growth and nucleation.

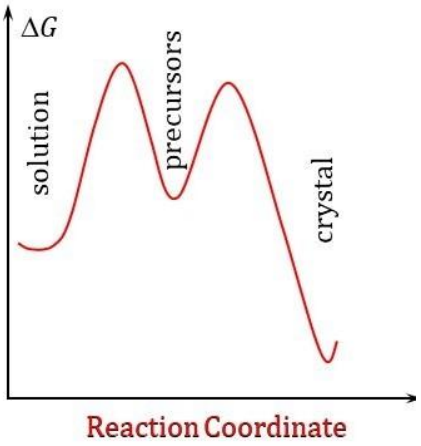

Figure 27: Free energy profile showing precursors having lower free energy.

Advanced imaging and spectroscopic techniques has been used extensively to study building blocks or growth units of complex biological, geological and synthetic

environments have exposed cases of non-classical crystallization employing crystalline, liquid and amorphous precursors[49,132,133]. To understand the violation of Szillard postulate, we must rely on the fact that Szillard based his postulate on a statistic argument. He argued that because a cluster of size n bigger that 1 has excess free energy due to the surface that is being created as this cluster nucleates the population of these clusters will be extremely low. Thus precursors in solution must populate a minimum in the free energy (shown in figure 27) as a function of a reaction coordinate leading to the formation of crystal.

Numerous examples of crystallization precursors that can be found in solution as shown in figure 2, which lists six such possible crystallization precursors. One very important peculiarity is that these non-classical mechanisms represent only a partial violation of the Szillard rule as growth units have a bimodal distribution of monomers and precursors. We show a complete violation of Szillard postulate during etioporphyrin I growth, the solute in the system we study populates a continuum of dimers that differ by their confirmation and then these dimers transform to the crystal competent structure upon association to the crystal lattice.

4.1 Etioporphyrin I Crystals

Etioporphyrin I, a free base porphyrin containing a relatively large porphyrin core hosts delocalized electron density and has disordered side chains which significantly lowers the crystal symmetry. As a result, the crystals of etioporphyrin I, possess appealing optical and electronic properties for use in modern high-tech applications for solar cells and transistors. It has a porphyrine core with four polar pyrrole groups (dipole moment μ = 1.81D) connected by methine bridges and alternating methyl and ethyl groups. Etioporphyrin I crystallized in the low symmetry P1 space group[8]. The molecules of etioporphyrin I in the

crystal has intermolecular π-π interactions (figure 28). The crystals of etioporphyrin I obtained by slow cooling of supersaturated solution has well and clear facets as shown in figure 28.

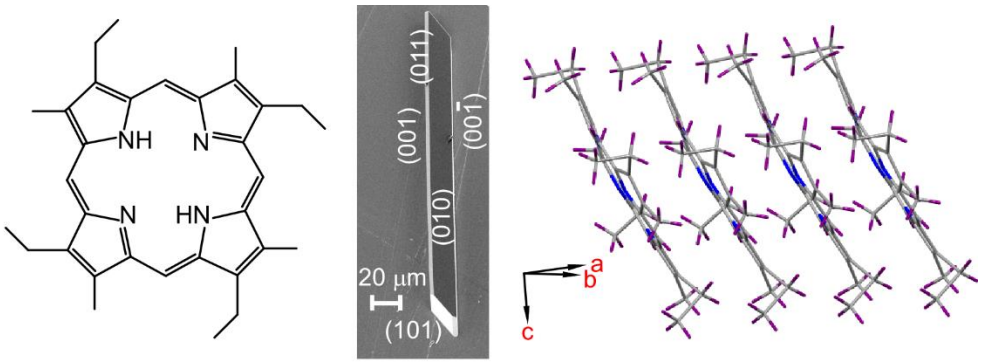

Figure 28: Etioporphyrin I molecule and crystal structure. Etioporphyrin I, a free base porphyrin with four pyrrole groups and alternating methyl, ethyl side chains. Scanning electron micrograph of etioporphyrin I crystals grown from octanol showing several crystal facets. Stacks of etioporphyrin I molecules along the a axis of the crystal lattice.

4.2 Single Crystal XRD of Etioporphyrin I

The crystal faces of etioporphyrin I obtained by slow cooling from octanol solution were indexed on a Bruker D8 Venture diffractometer equipped with a charge-coupled device (CCD) detector using graphite-monochromated Cu Kα radiation ($\lambda = 1.54056$ Å) and an APEX-3 face indexing plug-in.

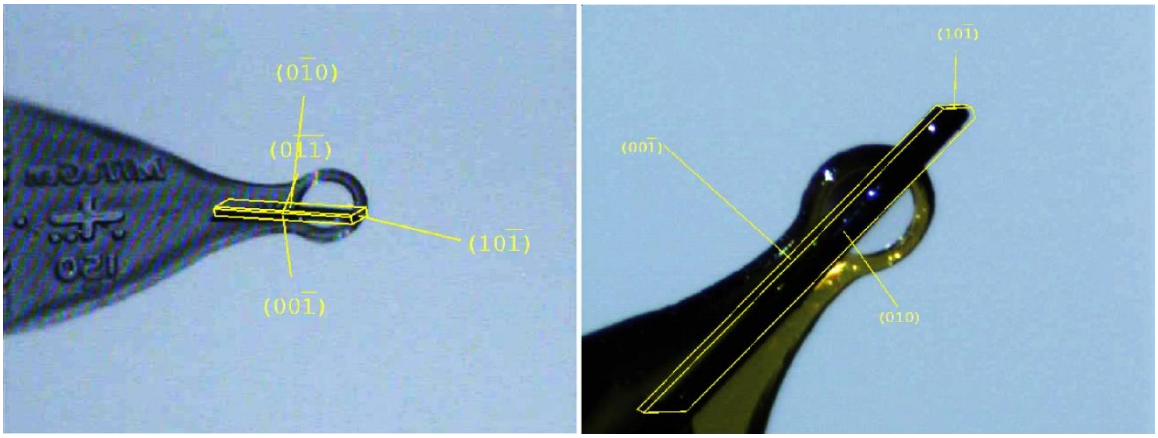

Figure 29: Face indexing of etioporphyrin I crystals obtained from alcohols.

4.3 Growth of Etioporphyrin I Crystals

Etioporphyrin I crystals were obtained by slow cooling. To understand the molecular mechanism of growth, we performed time resolved *in-situ* Atomic Force Microscopy. Crystals of etioporphyrin I were grown by slow cooling on a glass coverslip scratched at the center. Supersaturated solutions of etioporphyrin I in octanol (C = 0.50mM) were made by slow cooling at the rate of 5^{o}C/15 mins. Clear facets of etioporphyrin I crystals were seen in microscope and scanning electron microcopy (figure 28) clear facets of etioporphyrin I like [010], [001], [011] were clearly visible. We performed time resolved in-situ AFM on (010) and (001) faces of etioporphyrin I.

4.4 In-situ Atomic Force Microscopy of Anisotropic Growth Rates

We used a multimode atomic force microscope (Nanoscope IV) from Digital Instruments (Santa Barbara, CA) for all AFM experiments. AFM images were collected in tapping mode using Olympus TR800PSA probes (Silicon nitride, Cr/Au coated 5/30, 0.15 N/m spring constant) with a tapping frequency of 32 kHz. Image sizes ranged from nm to 20 μm. Scan rates were between 1 and 2.52 s^{-1}. Height, amplitude, and phase imaging modes were employed. The captured images contained 256 scan lines at angles depending on the orientation of the monitored crystal [52,134]. The temperature in the fluid cell reached a steady value of 28 ± 0.1°C within 15 min of imaging [52]. This value was higher than room temperature (ca. 22°C) owing to heating by the AFM scanner and laser.

Pure etioporphyrin I crystals were grown on glass disks as described above. The density of attached etioporphyrin I crystals was monitored under an optical microscope. We ensured similar crystal density for all samples to minimize potential depletion of solute due to high crystal number. The glass slides were mounted on AFM sample disks (Ted Pella

Inc.) and the samples were placed on the AFM scanner. Etioporphyrin I solution in octanol with varying concentrations were prepared less than 2 h in advance. This solution was loaded into the AFM liquid cell using 1 mL disposable polypropylene syringes (Henck Sass Wolf), tolerant of organic solvents. After loading, the system was left standing for 10 min to thermally equilibrate. The crystal edges and surface morphology were used to identify the (010) and (001) crystal surface. Etioporphyrin I crystals are very dynamic hence the surface features changed rapidly in presence of the growth solution. We set the scan direction parallel to the [100] crystallographic direction and AFM images were collected for 30 minutes. The solution in the AFM fluid cell was refreshed every 10-15 min to maintain constant concentration. With each etioporphyrin I concentration, AFM images were collected for 30 minutes, during which the solution was replenished several times. Etioporphyrin I solution was pumped into the AFM cell and the observed crystal could grow uninhibited for about 15 min before another etioporphyrin I concentration was introduced.

The evolution of the etioporphyrin I crystal surface was characterized by the velocity of growing steps ν. To determine v, we monitored the displacements of 10 – 15 individual steps with a measured step height h = 1.17 ± 0.07 nm and 9.9 ± 0.05 nm on the (001) and (010) face, respectively. Between 25 and 35 measurements were taken for each individual step and the average growth rates were reported.

The goal of the AFM investigations is to establish the molecular mechanisms of etioporphyrin I crystal growth. Using AFM imaging at mesoscopic scale, we measured the step displacement with time. The presence of steps, however, disrupts the contact between the scanning tip and the crystal surface and lowers the image resolution. The steps

outcropping from a screw dislocation move with time (figure 31), the displacements were measured with time and reported as shown in figures 31 and 32.

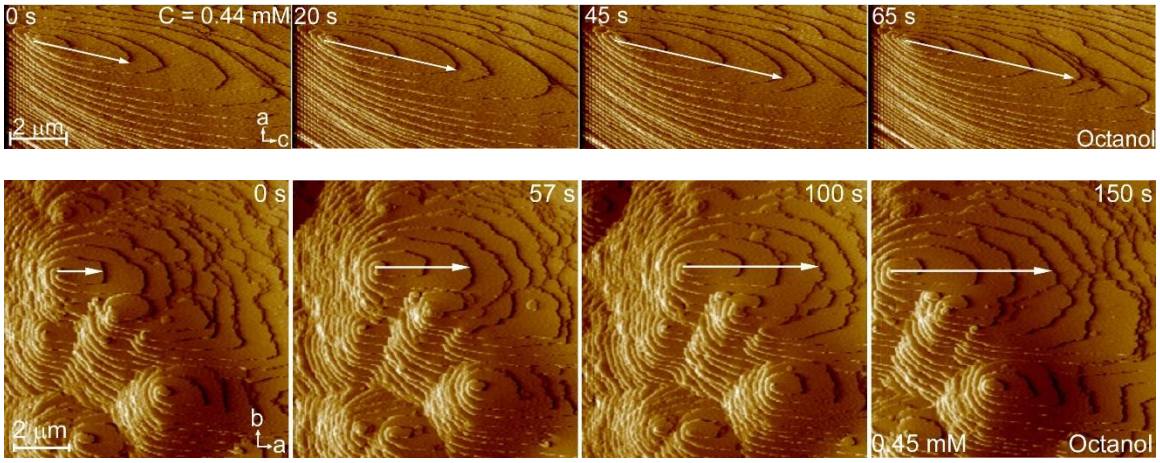

Figure 30: Steps outcropping from screw dislocations and displacements with time on the (010) top and (001) bottom face of etioporphyrin I.

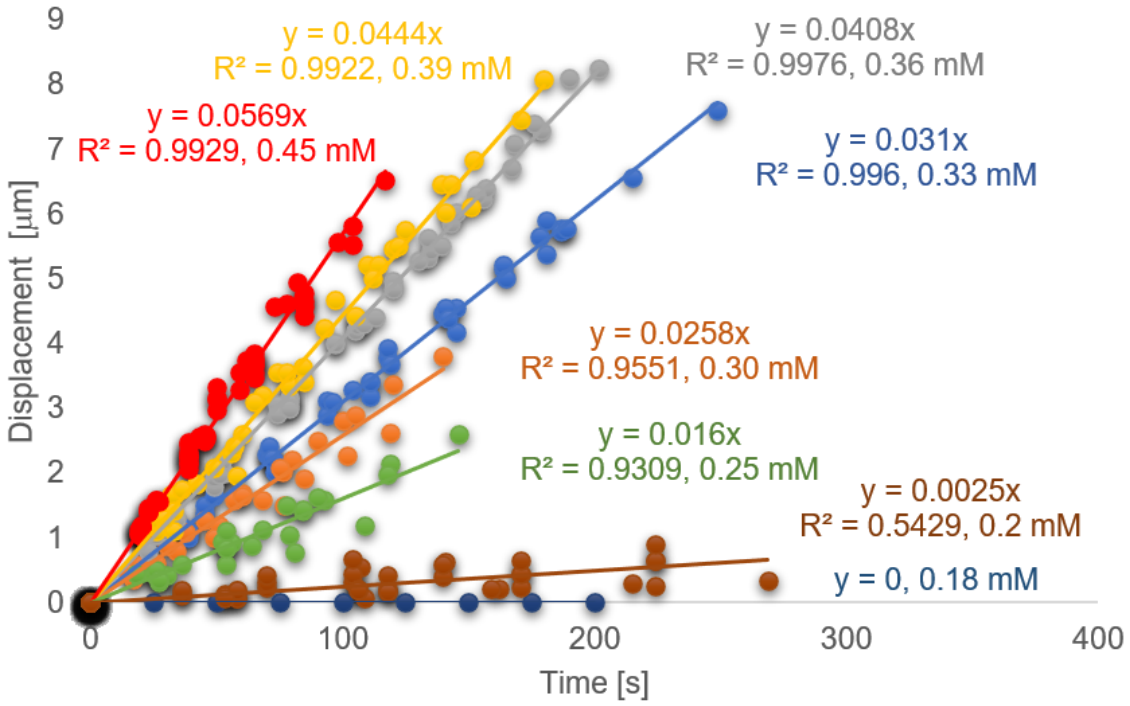

Figure 31: Step displacement measured on the (010) face with time. Displacements were averaged over 10-15 steps for statistics. The slope of each curve gives the step velocities and the R^2 values gives the validity of the fit.

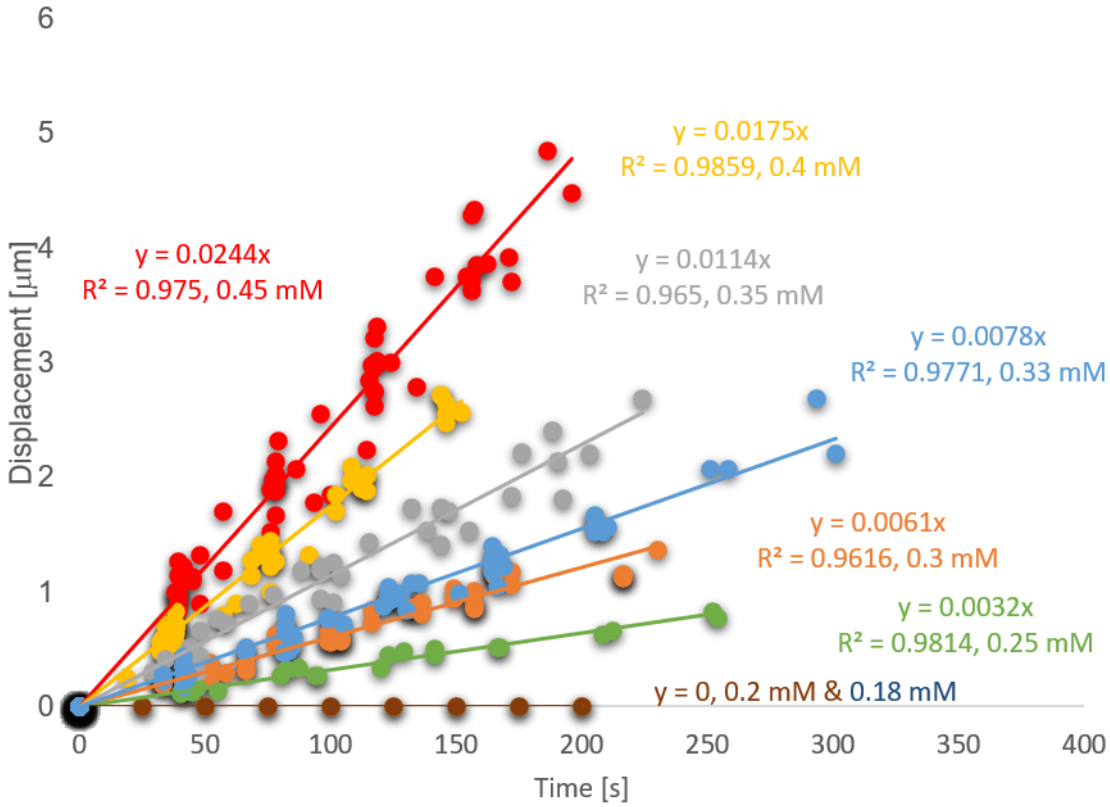

Figure 32: Step displacement measured on the (001) face with time. Displacements were averaged over 10-15 steps for statistics. The slope of each curve gives the step velocities and the R^2 values gives the validity of the fit.

The step displacements with time on the (010) and (001) face of etioporphyrin I are shown in figures 31 and 32 respectively. Etioporphyrin I exhibits two faces (010) and (001) as shown in figure 25 both faces grow by spreading of layers which are generated by screw dislocations outcropping on the face of monomolecular height. Step velocities are the rate of solute attachment to the crystal growth sites or kinks. Step displacements were monitored with time and the slopes of step displacement curves (as shown in figure 27 and 28) were used as step velocities.

Classical crystal growth theory assumes that crystals grow by incorporation solute monomers. The implied monomolecular reaction should give rise to a linear correlation between v and solute concentration C, $v = \beta\Omega(C - C_e)$, where subtracting solubility C_e

accounts for the reversibility of molecular attachment, Ω is the molecular volume in the crystal and β is the effective kinetic coefficient, which includes kinetic parameters for a selected growth mode, direct incorporation or surface diffusion. Linear v(C) correlations has been observed in hundreds of crystals organic, inorganic, colloids, proteins, and virus in the last twenty years[25].

The (001) face of etioporphyrin I differs not only by its morphology, but the most important difference is that the correlation between step velocity and solute concentration is superlinear which extends to concentrations more than twice as high as the solubility C_e. A superlinear dependence is highly unusual. Before understanding the deep fundamental mechanism of superlinearity we need to eliminate possible trivial reasons for these observations.

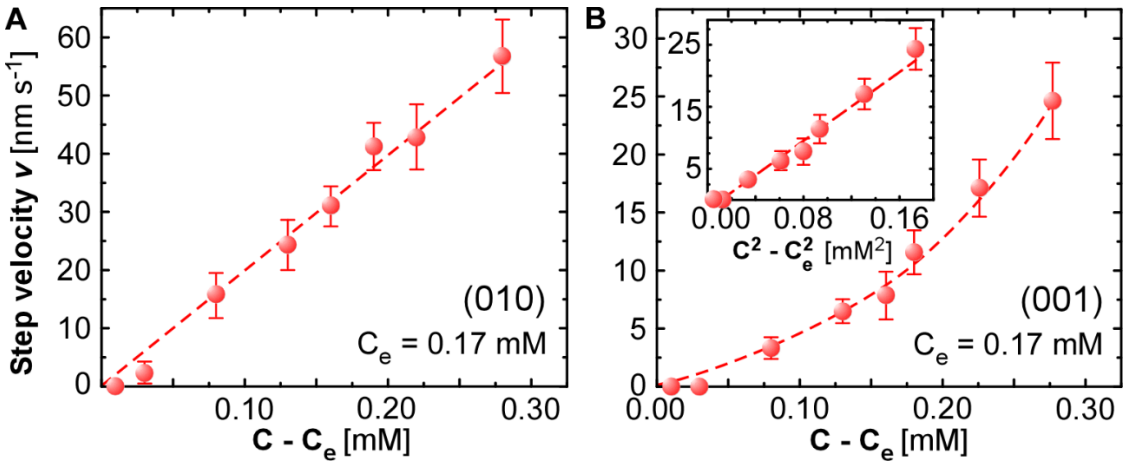

Figure 33: Measurement of step velocity on (010) and (001) face. A. Step velocities vary linearly with etioporphyrin I concentration on (010) face (Inset: step displacement measurement with time) and **B.** follows a superlinear trend on the (001) face.

4.5 Potential Reasons for Superlinearity

Potential reasons for apparent growth acceleration at high supersaturation include inaccurate measurement of solubility C_e, interpolated for the temperatures of the AFM measurements, 28°C. For an alternative determination, we continuously monitor a step site in a solution with $C = C_e$ at 28°C and observed a short segment of step on both faces, the attachment of solute from the solution is balanced by the detachment of solute from the step (figure 32A) on both faces. These dynamics indicate equilibrium between the solution and step and confirm the solubility determination. A second hypothesis is that steps on both faces have a paucity of kinks as the solute concentration increases, a higher kink density leads to faster than linear dependence between the step velocity and solute concentration. High resolution images of the step segments on both faces show that the steps in both faces are rich in kinks and the kink density is probably close to the thermodynamic limit of 0.3 so an increase in concentration cannot lead to a higher kink density and subsequently superlinear dependence of step velocity on the concentration (figure 29B).

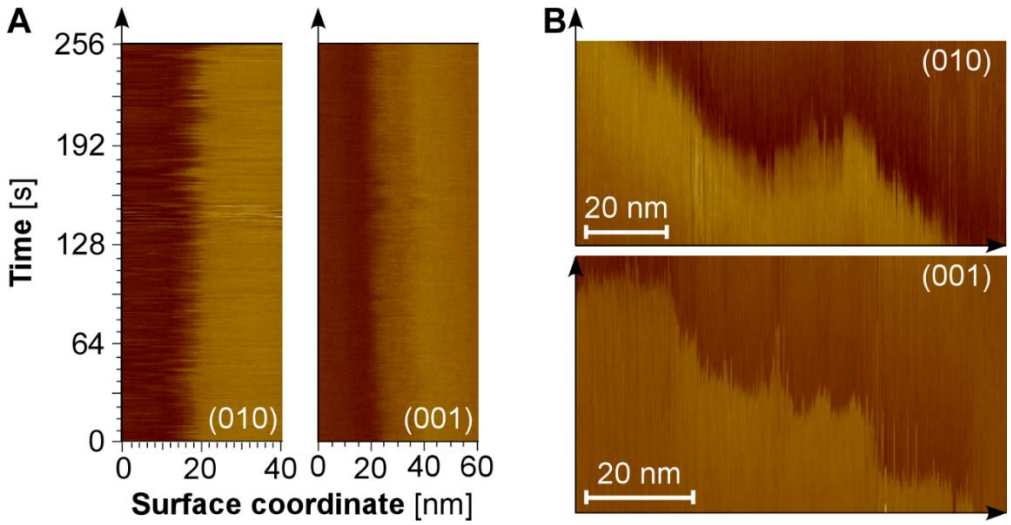

Figure 34: Elimination of factors for superlinear growth. A. Disabled y-axis *in-situ* AFM scan on (010) and (001) face at 28°C where the x axis is time and y axis is the surface coordinate. **B.** Kink density on the (010) and (001) face at C_e.

A third possible mechanism of the observed super linearity is the action of impurities that adsorb on the steps and enforce curvature on the advancing steps which slows them down. These mechanisms would lead to superlinear dependence in a relatively narrow region of supersaturation where the size of the critical 2d nucleus is commensurate with the spacing between the stoppers. Etioporphyrin crystals on the (001) face exhibit nonlinear dependence over concentration that ranges by a factor of 15 which eliminates step pinning as a possible mechanism of superlinearity.

This leaves us with another possible mechanism which assumes that two monomers in the solution form a dimer then the dimes incorporate into the crystal, recently in a paper the kinetic scenario, was modelled and it was concluded that in the case the dimers coexist with a majority of monomers in the solution only in this case the step velocity will be a quadratic function of the supersaturation[15]. We plot the step velocity and quadratic concentration dependence, and we find a linear plot (Figure 33B inset), which confirms the quadratic growth mechanism. The incorporating and the majority species in solution determines the shape of the step velocity curve. If a majority of dimers exists in the solution and dimers are the incorporation species we get a linear dependence of the step velocity on the concentration. If dimer is the majority species but the dimer needs to dissociate into monomers which then incorporates into the kink we will get a sublinear dependence of the step velocity on the concentration these scenarios of step velocity variation are depicted in figure 35.

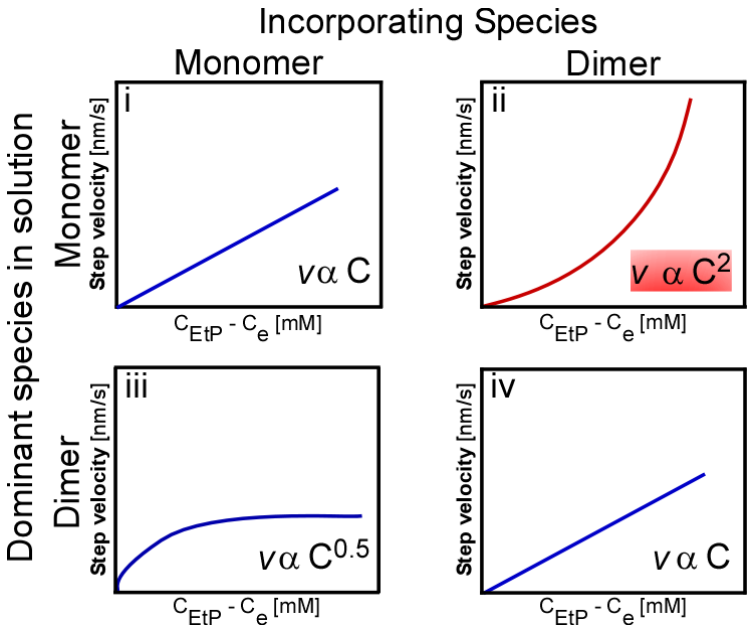

Figure 35: Step velocity variation with solute concentration for different incorporating species.

If the incorporating species is same as the dominant species in solution, we get linear curves.

4.6 Uv-vis Spectrum of Etioporphyrin I Solution

We characterized etioporphyrin I solution in octanol with absorption spectroscopy since etioporphyrin I contains four pyrrole rings in its porphine ring structure, a symmetric structure would produce a single q band, the 2 hydrogens which are part of the etioporphyrin I structure lower the symmetry of the ring to two-fold. With two-fold symmetry two bands which corresponds to the two groups of pyrrole ring should exist. The experimental absorption spectrum measured in two experimental exhibit four to five q bands the only explanation of this is that two monomers are in proximity of each other which causes splitting of the energy levels and multiplies the q bands. This conclusion is supported by DFT quantum mechanical modelling which shows that single etioporphyrin I monomer should exhibit two q bands while a dimer should exhibit 5-6 q bands in its

absorption spectra (figure 36). Even though the experimentally measured spectra is similar to the dimer model there are still subtle differences, we model several other dimers and what appears that all of these spectra's are similar to the dimer spectra yet they differ by the intensity of the peaks and in peak positions. No monomers are present in the solution and the crystals grow only by incorporation of dimers. The experimental dimer spectra is the superposition of several dimer spectra present in the solution.

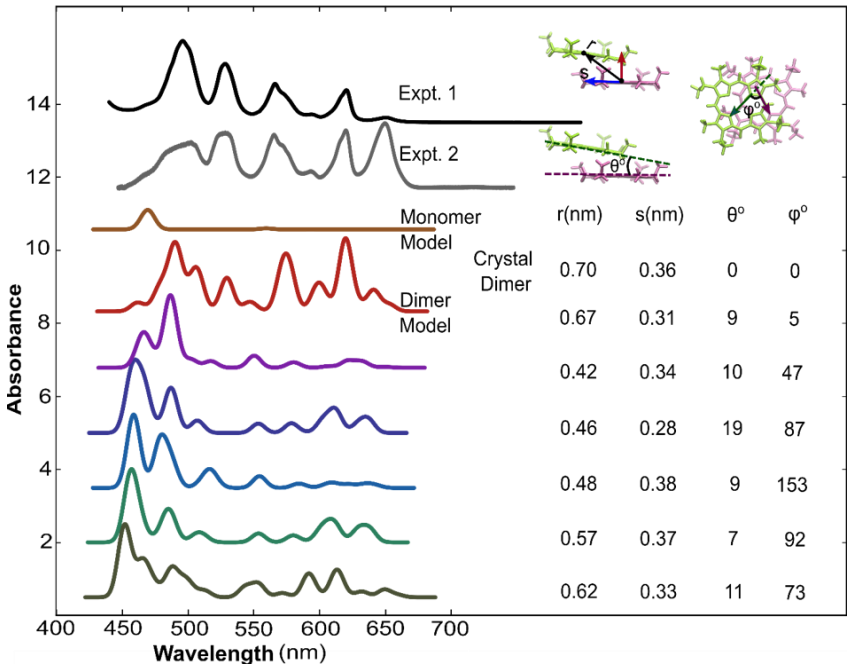

Figure 36: Uv-vis absorption spectra and DFT modeling of etioporphyrin I absorption spectra.

We model the dimerization equilibrium by all-atom MD simulation. The potential of free force between two dimers in the solution as the function of separation between them. Here we have the population of the states which differ by the shift (how much the centers of the two monomers in a dimer are displaced) or by the tilt angle or by the twist angle. Now all these data sets show that dimer stability is very insensitive to variation of the conformation variables of the dimer.

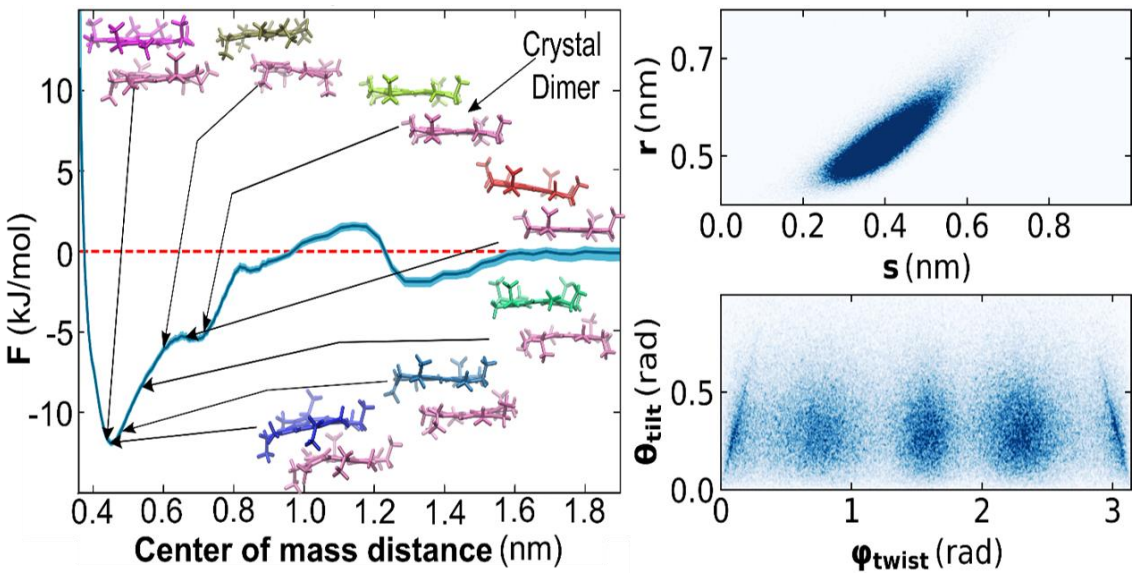

Figure 37: Dimerization equilibrium of etioporphyrin I in octanol, showing that a continuum of dimers exists in solution and crystalline dimers are underrepresented in the solution.

Which means we will have a continuum of dimers in the solution the crystal dimer has a relatively high energy, it is underrepresented in the solution. A few findings of this work are:

1. Crystals of etioporphyrin I grow exclusively by incorporation of dimers.
2. Solution dimers which are different from the crystallographic dimers must transform into crystallographic dimers upon incorporation into kinks.
3. Linear correlation between the step velocity and concentration on the 010 face, indicates a very simple straightforward sequential incorporation into kinks.
4. The quadratic relationship on the (001) face indicates that two dimers must cooperate to get incorporated into the kinks.

4.7 Direct Incorporation into Kinks

There are two modes of solute incorporation into the growth sites one is via surface diffusion, where the solute molecules adsorb on the terrace and diffuse towards the kinks

and the other is direct incorporation into the kinks (figure 39 A). Surface diffusion leads to competition for solutes between two closely placed steps while direct incorporation the transport field of solute being three-dimensional lead to similar step velocities of closely spaced steps. The steps velocities were independent of the step separation on both faces of etioporphyrin I indicating growth by direct incorporation (figure 39 E and I). All atom MD simulation of etioporphyrin I dimer incorporation directly into the kinks of (010) and (001) face indicate that adsorption of etioporphyrin I on (010) and (001) is not possible due to distinct reasons, on the (010) face incorporating species is not well aligned to the kinks and on the (001) face the free energy of adsorption is high thus dimers adsorb too strongly on the grooves of (001) face to desorb and diffuse.

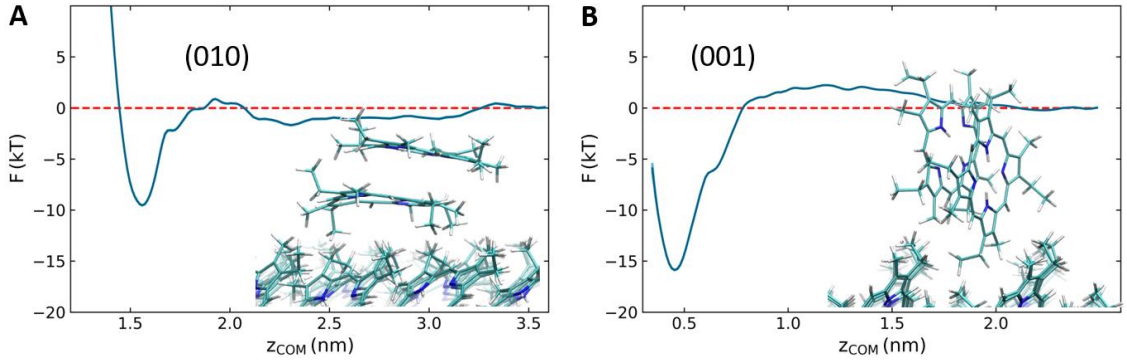

Figure 38: Free energy of adsorption of etioporphyrin I dimers on the (010) and (001) face.

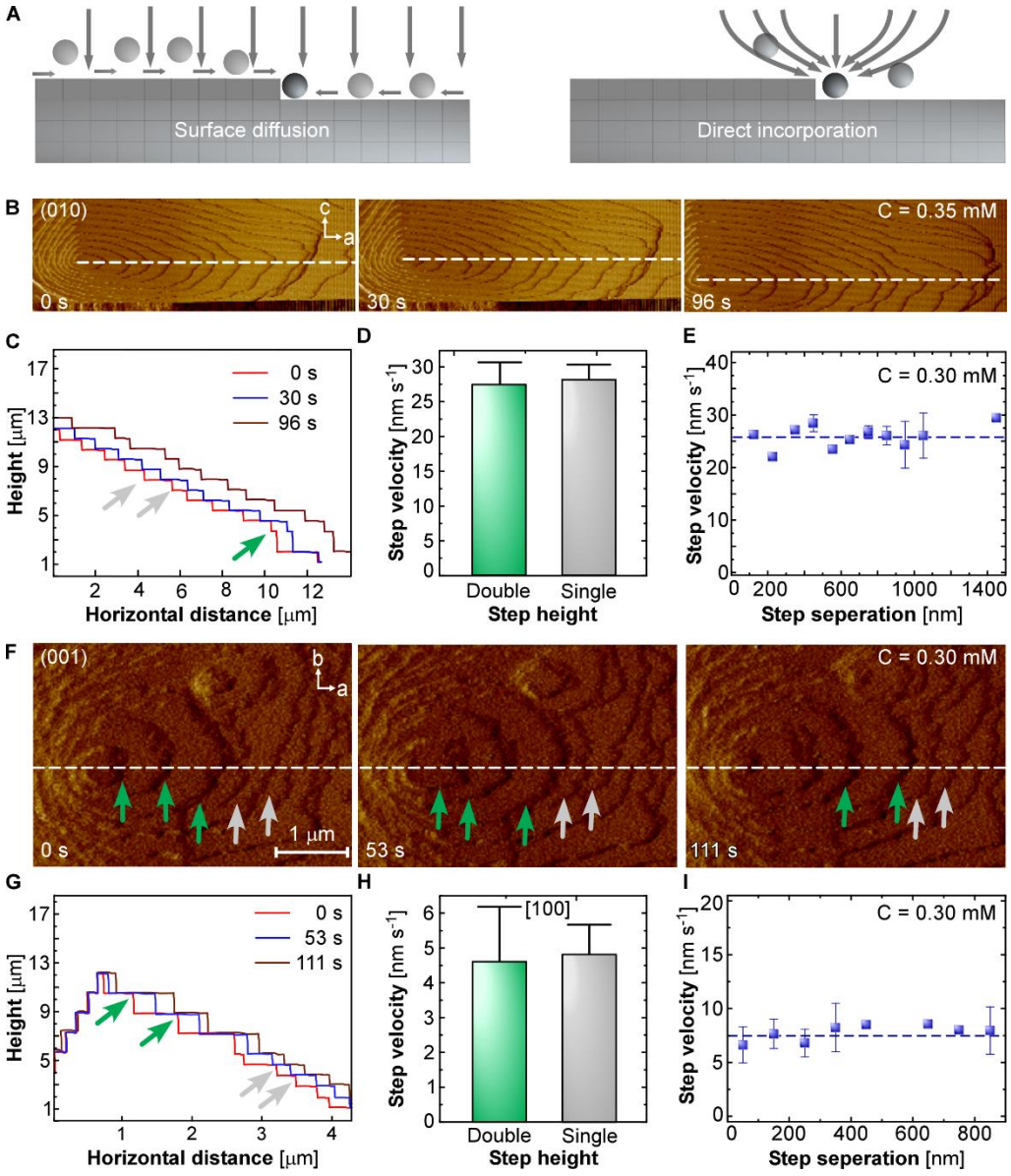

Figure 39: Direct incorporation of etioporphyrin I on (010) and (001) face. A. Schematic representation of surface diffusion and direct incorporation into kinks or growth sites. **B.** Steps on the (010) face of etioporphyrin I growing in presence of octanol at different time intervals at 35mM concentration showing the propagation of both single and double steps. **C.** Height profiles of steps in panel **B** where single steps are shown in silver and double steps in grey. **D.** Step velocities of double and single steps on the (010) face measured along a axis. **E.** Step velocity variation with step separation at *C*= 0.30 mM which shows step velocities are independent of step separation. Panels (F-I) show the same variation for (001) face.

4.8 All-atom MD Simulation of Etioporphyrin I Incorporation into Kink

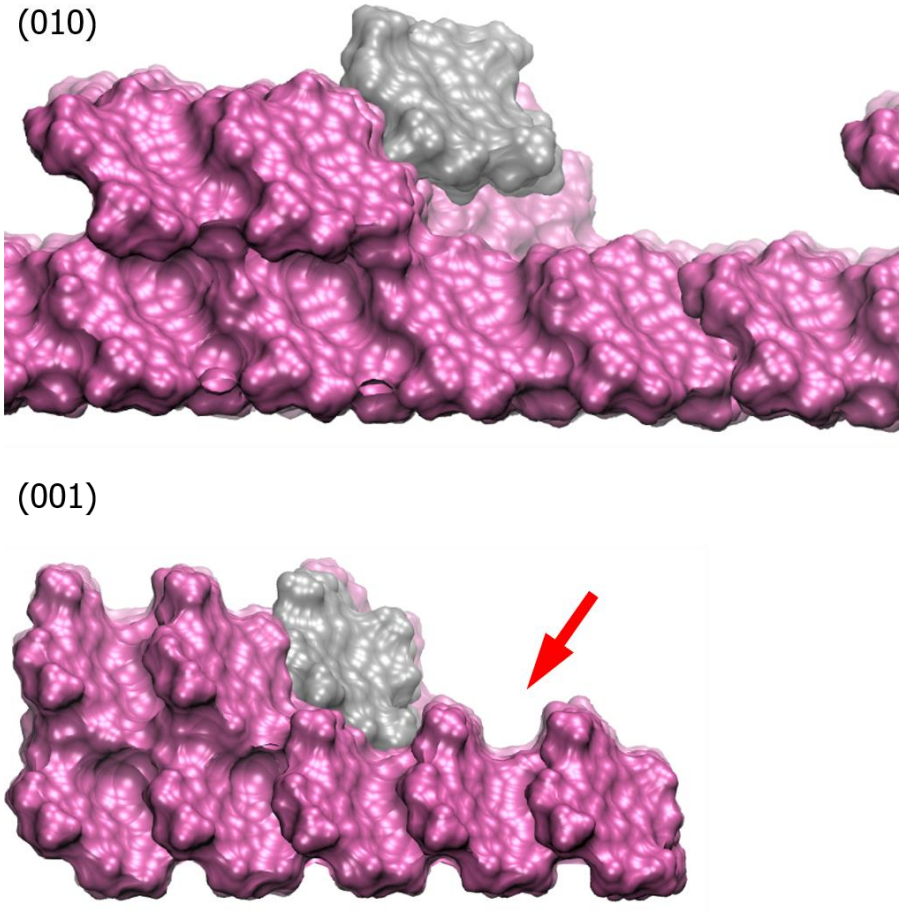

Figure 40: Configuration of Kinks on the (010) and (001) face. Schematics of solute molecule incorporation on the smooth (010) face promotes direct incorporation into the kinks and the grooved (001) needs the presence of two dimers for the formation of growth competent species.

To understand the incorporation of etioporphyrin I dimers on the 010 face of etioporphyrin Figure 40 shows the presence of two types of kinks, we see the presence of kinks which are very open on (010) face, and molecules directly attach to the kinks. On the (001) face the presence of grooves obstructs direct incorporation of etioporphyrin I dimers into the kinks and two dimers are required for turning the growth incompetent dimers to incorporate into the kinks.

4.9 Inference:

An example of complete violation of Szilard rule, whereby a continuum of building blocks contributes to crystallization is presented in this work. Here we report a complete violation of the Szilard rule. In octanol solutions of etioporphyrin I, a planar molecule whose crystals have attractive electronic and optical properties, the solute populates a continuum of quasi-parallel dimers that differ from the conformation in the crystal by shift and orientation. Molecular absorption and luminescence spectroscopies and all-atom molecular dynamics (MD) simulations reveal that the stabilities of the dimers are within the thermal energy and enforce free conversion between the distinct structures. The monomer concentration in the solution in below 0.1 %. Despite the structural complexity of the solute, the velocity of the steps on the (010) faces of etioporphyrin crystals (measured using time resolved in situ AFM) increases linearly with the total solute concentration. The observed linearity indicates that the molecular reaction at the growth sites in monomolecular and the majority of solute dimers seamlessly adopt the crystallographic conformation. By contrast, step growth on the other major face, (001), scales with the square of the solute concentration. We eliminate three potential mechanisms that may manifest as super-linear growth: inaccurate solubility determination, escalating kink density at elevated supersaturation, and adsorption of step pinners on the crystal surface. The disqualification of the three scenarios enforces the conclusion that the quadratic kinetic law indicates a bimolecular process of incorporation. We demonstrate that in contrast to numerous other solution grown crystals, solute molecules directly incorporate in the kinks and do not reach the growth sites after first adsorbing on the terraces between steps. The paucity of solute monomers precludes a collision between two monomers to form a

crystallographic dimer as the mechanism of the crystallization reaction. MD evaluation of solute interactions with kinks on the (001) face reveal a molecular trap selective for solute dimers located on the approach to all kinks, which necessitates a collision with a second dimer to ease the captured solute towards the kink. The results with etioporphyrin demonstrate the lack of correlation between the solute state and the incorporation kinetics driven by the solute. In a broader context, these observations illuminate the immense diversity of unexplored crystallization scenarios that pave the long road to crystallization control.

Chapter 5: The elementary reactions for incorporation into kinks

Molecular crystallization is a principal stage in the assembly of biological, geological, and engineered materials [135-139]. Classical theories posit that the crystallization rates and pathways are largely dictated by the slow ingress of solute molecules into specifically structured growth sites, the kinks [99,140], but the interactions and structures that administer the access to a kink remain elusive [141]. Here we show that *en route* to a kink an incoming solute molecule forms an intermediate complex, in which the solute binds, but only partially, to the molecules that comprise the kink; the disruption of the solute–solute and solute-solvent contacts that uphold this complex constitutes the transition state for incorporation. We combine time-resolved *in situ* atomic force microscopy with all-atom molecular dynamics simulations to examine the crystal growth of etioporphyrin I, which represents a class of materials with appealing optico-electronic properties [8,96,97]. Violating the classical models of solution crystallization, the measured activation barriers for crystallization disconnect from the strengths of the interactions of the solute with the four solvents and imply that a structure comprised of both solute and solvent molecules controls the access to a kink. MD simulations reveal that in this structure an incoming solute molecule forms a fraction of the crystal contacts whereas the remaining contacts are open to solvent molecules. The spatial constraints on the solvent access to the open contacts rank how much the distinct solvents stabilize this complex and set the height of the barrier to be surmounted for incorporation. The proposed two-step scheme of molecular incorporation presents an alternative paradigm that may expedite the selection of solutes and solvents in the crystallization process design of numerous organic electronic and solar materials [142].

Etioporphyrin I incorporates four pyrrole residues linked by methine groups into a flat porphyrin ring and decorated by alternating four ethyl and four methyl groups (Figure. 41a). In the known unsolvated crystal form with symmetry P1 the etioporphyrin molecules arrange in columnar stacks supported by π-π bonds and oriented roughly along the [110] direction (Figure. 41b) [8]. To illuminate the molecular interactions that govern how solute molecules incorporate into crystals, we compare the kinetics of etioporphyrin I crystallization from solutions in three alcohols with increasing alkyl chain length, butyl, hexanyl, and octanyl, and dimethyl sulfoxide (DMSO), a small molecule with two short aliphatic residues. This comparison is substantiated by the identical P1 structures of the crystals that grow from the four solvents [76]. The UV-vis absorption spectra of etioporphyrin I in these solvents feature a prominent Soret band, at ca. 400 nm, and four Q bands in the wavelength range 475 – 630 nm (Figure. 41c) attributed to distinct transitions of the conjugated π electron systems of the constituent pyrroles [118,143]. In aqueous solutions at elevated ionic strengths, which suppress Coulomb repulsion, [144] or in organic solvents, where two monomers were chemically tethered to stimulate dimerization [145], porphyrins may form co-facial dimers, in which the monomers position similarly to as in the crystal (Figure. 41b). Dimerization detectably modifies the UV-vis spectra of porphyrins: the Soret band shifts to higher wavelengths (the shift depends on the solvent, the porphyrin sidechains, and on the presence of a metal ion in the porphyrin core) and the shapes and relative heights of the Q bands adjust [113,144,145]. For etioporphyrin I, the Soret and the Q bands are similarly structured in the three alcohols and DMSO and signify that the dominant solute species, whether they be monomers or dimers, are identical in the four solvents.

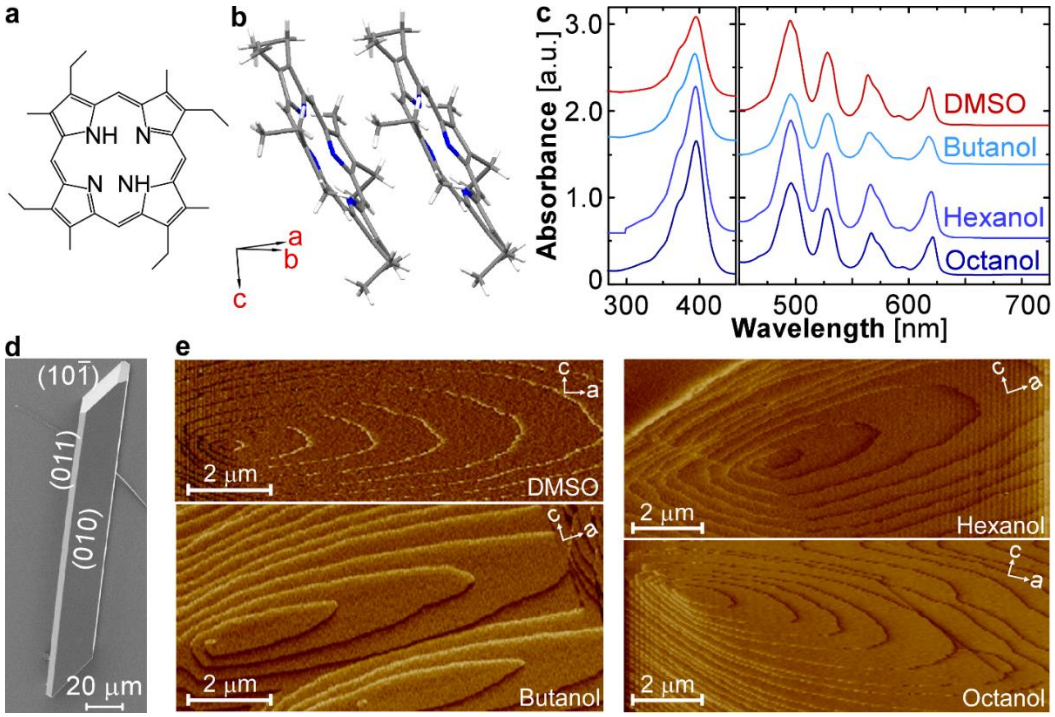

Figure 41: Etioporphyrin I crystals and solutions. a. The etioporphyrin I molecule**. b.** Stacks of etioporphyrin I molecules in the crystal in P1 space group; Cambridge Structural Database REFCODE WOBVUF Ref.[8]; N in drawn in blue, C, in charcoal, and H, in silver. **c.** UV-vis absorption spectra of etioporphyrin I dissolved in DMSO, butanol, hexanol and octanol. **D.** Scanning electron micrograph of an etioporphyrin I crystal. **E.** *In-situ* atomic force microscopy (AFM) images of (010) face of etioporphyrin I growing from solutions in DMSO, butanol, hexanol, and octanol.

5.1 Displacement and Step Velocity Measurement

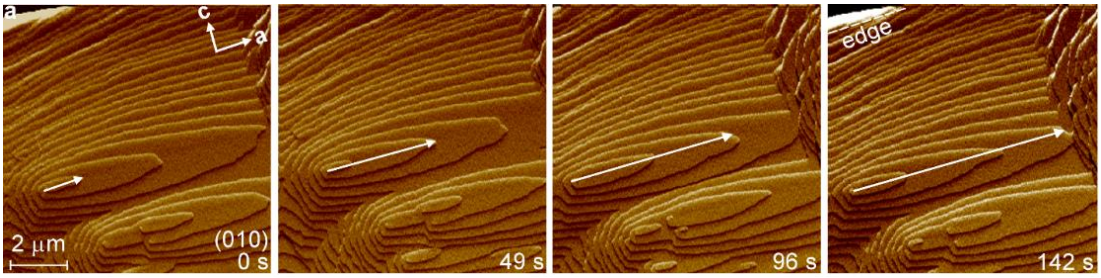

Figure 42: Time resolved *in situ* AFM images of etioporphyrin I (010) face growing from butanol. Arrows trace the growth of a step in the [100] direction.

(010), (011), and (101) faces are prominent in the habit of etioporphyrin I crystals grown from the three alcohols and DMSO (Figure. 41d). Typically, a (010) face orients

parallel to the substrate and affords a clear line of sight to atomic force microscopy (AFM). *In situ* AFM images (Figure 41e) in supersaturated solutions, where the solute concentration C exceeds the solubility C_e (the concentration at which a crystal and the solution are at equilibrium), reveal that the (010) faces are comprised of unfinished layers structured as spirals that originate at the outcrops of screw dislocations, similar to numerous other crystals growing from solution [146,147]. The crystals grow as solute molecules associate to kinks located along the edges of the unfinished layers, the steps [99,100,148]. The crystal anisotropy enforces distinct velocities of the steps that propagate in different directions such that steps in the [100] or $\vec{a}$ direction grow fastest and reach furthest from the dislocation (Figure 41e). In this way, the shape of the growth spiral reveals the ratios between the anisotropic step velocities; these ratios are similar in the four solvents (Figure. 41e) and independent of the supersaturation.

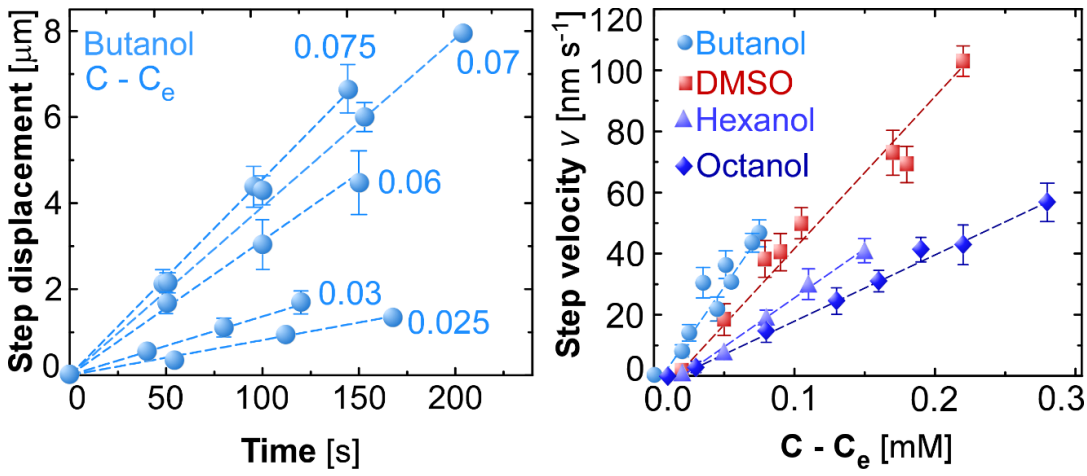

Figure 43: Displacements and step velocities measured in butanol. a. The evolutions of the step displacements during growth from butanol at printed values of $C - C_e$. **b.** Step velocity v, determined from the slopes of the time correlations of the step displacement as in b., as a function of the concentration C in the four listed solvents.

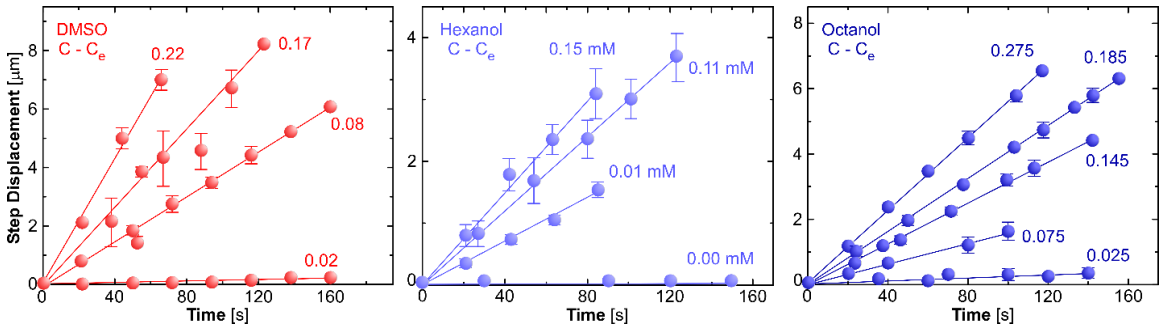

Figure 44: Step displacements measured in DMSO, hexanol and octanol.

We applied time-resolved *in situ* AFM to track the locations of growing steps in the [100] direction (Figure. 42). The step growth was steady in time (Figure. 43a) and the slopes of the time correlations of the step displacements present the step velocities v. In all solvents, v increased lineally with the solute concentration C (Figure. 43b), in common with numerous other solution grown crystals [38]. Mass preservation dictates that v equals the product of the rate of the chemical reaction of the solute with the kinks and the contribution of one molecule to step propagation, the solute molecular size a, $v = ak_a(C - C_e)$, where k_a is a second-order rate constant and subtracting the solubility C_e accounts for the reversibility of molecular attachment. Alternatively, the v has been modeled as the product of the solute flux into a kink and the volume Ω that a solute molecule contributes to the crystal, resulting in $v = \beta\Omega(C - C_e)$ [35,36]; here β is the step kinetic coefficient. Comparing the two relations informs that $ak_a = \beta\Omega$.

5.2 Solvent Viscosities

The viscosity of organic solvents varies non-linearly with temperature. Solvent viscosities at 28ºC were determined from the literature. We did linear interpolation of viscosity between 25º C and 30ºC/ 35ºC the two-bracketing temperatures. The solvent viscosities at 28ºC are reported in the table below and shown in figure 44.

Table 2: Solvent viscosities at 28°C

Solvent	Viscosity (cps)
DMSO	1.89 ± 0.02
Butanol	2.35 ± 0.025
Hexanol	4.15 ± 0.027
Octanol	7± 0.03

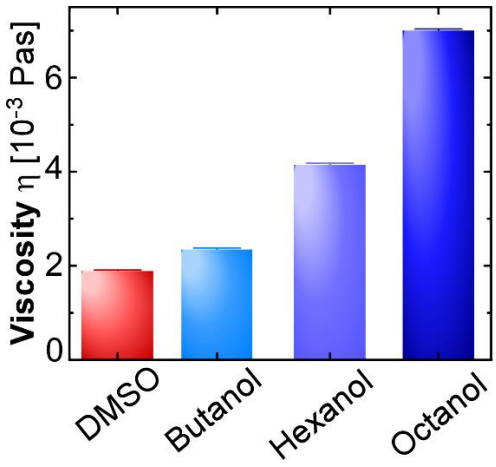

Figure 45: The viscosities η of the four solvents at 28° C, the temperature of the AFM measurements

5.3 Direct Incorporation into Kinks

To further illuminate the mechanism of solute incorporation into kinks, we start with whether etioporphyrin molecules reach the steps directly from the solution (Figure. 45a) or, as numerous solution grown crystals [15,149-151], after adsorption on the terraces between steps followed by diffusion towards the steps (Figure. 45b). Two sets of observations suggest that etioporphyrin I, uniquely, prefers the direct incorporation pathway during growth from the four solvents. First, v is independent of the step separation l for ls as short as a few nanometers (Figure. 46b). Second, in butanol, hexanol, and octanol the velocities of steps as high as the $\vec{b}$ lattice parameter ($|\vec{b}|$= 0.991 nm[8]), are close to those of steps of

height $h = 2|\vec{b}|$ (Figure. 47 c, d, f). If solute reaches the steps via the crystal surface, the step supply field is constrained to two dimensions, which stunts the growth of closely spaced steps or steps of $h = 2|\vec{b}|$. Concurrently, analytical models of the surface diffusion mechanism of step propagation predict that v scales with $h^{-1}s$. Experimental observations reveal that double-height steps that feed via the surface grow slower than single-height steps and may split into two single-height steps owing to unequal supply to the top and bottom layers [134,150]. By contrast, if the steps feed directly from the solution, the supply field is three-dimensional and abundant for closely spaced or twinned steps. Closed-form expressions for this growth mode predict negligible $v(h)$ correlation [35,36].

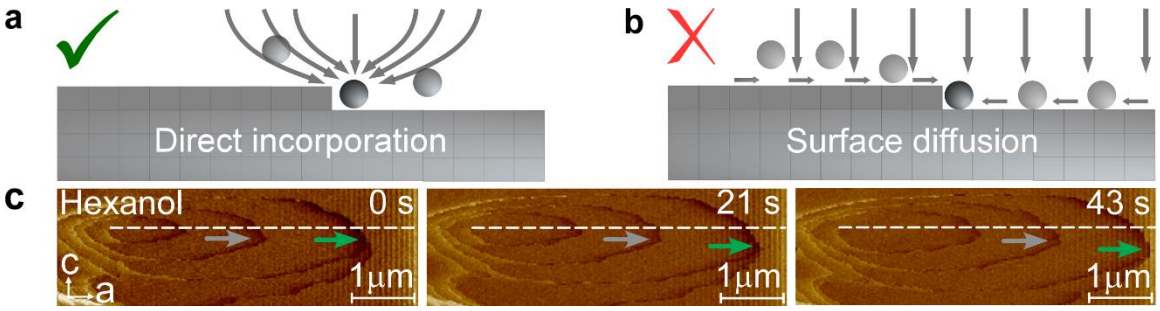

Figure 46: The pathway of a solute molecule into a kink. a, b. Schematic representations of two pathways from solution to steps. **a.** Solute molecules reach a step directly form the solution. **b.** Solute molecules adsorb on the crystal surface and diffuse towards the steps. **c.** Time resolved AFM images of the growth of single (silver arrows) and double (green arrows) steps of the (010) face at *C* = 0.23 mM in hexanol.

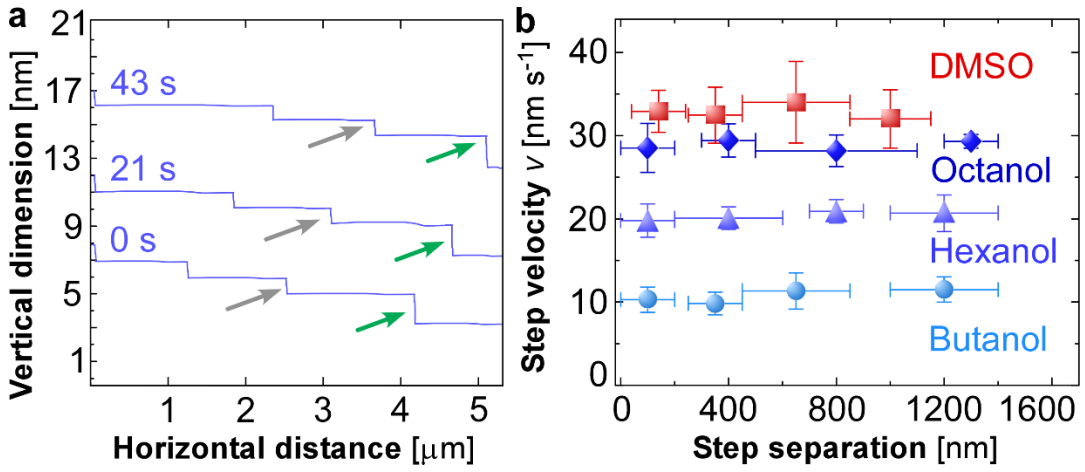

Figure 47: Step velocity vs step separation. a. The evolution of the surface profile along the dotted line in **c**. Double-height steps (green arrows) advance over lengths similar to those of single-height steps (silver arrows). **b.** The step velocity in the four solvent does not correlate with the step separation l. C = 0.23 mM in hexanol, 0.09 mM in butanol, 0.35 mM in octanol, and 0.25 mM in DMSO. The averages of 15-20 measurements for each step separation interval are shown. Vertical error bars represent the standard deviation of each measurement. Horizontal error bars represent the ranges of l during the measurements of v in each group.

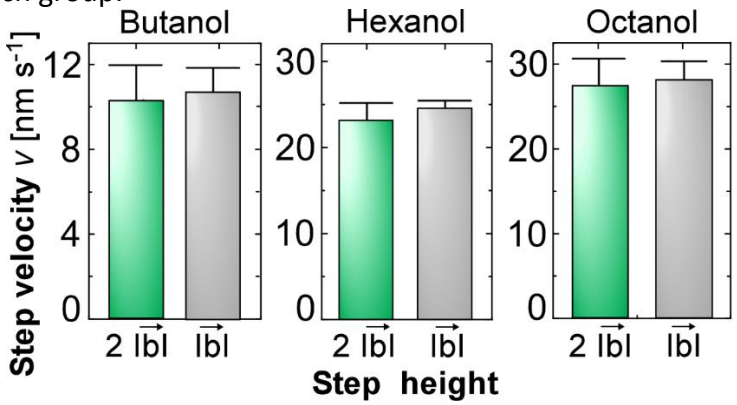

Figure 48: Comparison of the velocities v of single and double height steps in three solvents. The averages of 5-10 double and single heights steps are shown. Error bars represent the respective standard deviations. C = 0.23 mM in hexanol, 0.09 mM in butanol, and 0.35 mM in octanol.

5.4 Determination of Rate Constant

Assuming that etioporphyrin I crystals grow by incorporation of dimers that dominate the solution would double the values of a and Ω, but leave the core of the arguments below

intact. Scaling the slopes of the $v(C)$ correlations (Figure. 43b) with a exposes the dramatically divergent rate constants for incorporation into kinks from the four solvents (Figure. 48). The rates of chemical reactions occurring in solutions, in parallel with the reactants' diffusivities [152], scale as reciprocal viscosity of the solvent η^{-1} [153,154]. To expose the molecular behaviors that govern solute incorporation into kinks, we eliminate the divergent accounts for the reversibility of molecular attachment. Alternatively, the v has been modeled as the product of the solute flux into a kink and the volume Ω that a solute molecule contributes to the crystal, resulting in $v = \beta\Omega(C - C_e)$ [35,36]; here β is the step kinetic coefficient. Comparing the two relations informs that $ak_a = \beta\Omega$. Viscosities of the solvents (Figure. 44) and use the product $k_a\eta$ to quantify the reaction at a kink. The values of $k_a\eta$ are nearly identical for crystallization from solvents in the homologous series butanol – hexanol – octanol and lower by nearly half for crystallization from DMSO (Figure. 49). The rate constants were determined by assuming the incorporation of solute molecules in the kink as a bimolecular reaction where the rate constant $k_a = k_o \exp\left(\frac{\Delta G^{\ddagger}}{kT}\right)$ as shown in figure 48.

Table 3: Rate constants determined in different solvents.

Solvent	**Rate Constant K_a ($M^{-1}s^{-1}$)**
DMSO	$5.61*10^5 \pm 2.4*10^4$
Butanol	$7.54*10^5 \pm 7.60*10^4$
Hexanol	$4.08*10^5 \pm 2.28*10^3$
Octanol	$2.41*10^3 \pm 5.97*10^3$

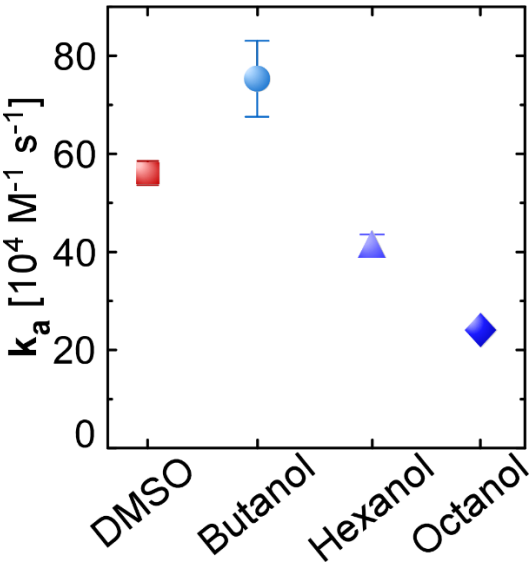

Figure 49: Second-order rate constants k_a for the reaction between incoming solute molecules and kinks evaluated from the $v(C)$ correations in 43b.

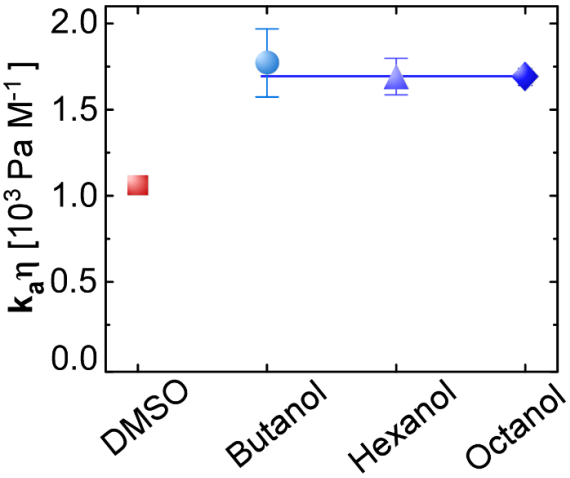

Figure 50: The product $k_a\eta$ for growth form the four solvents.

5.5 Determination of Activation Free Energy

We represent the rate constant k_a for the reaction between a kink and an incoming solute molecule as $k_a = k_0 \exp(-\Delta G^{\ddagger}/k_B T)$, where k_0 is the rate constant of a reaction uninhibited by an activation barrier and proceeding at the diffusion limit, $\Delta G^{\ddagger}$ is the free energy barrier for incorporation of solute molecules into kinks, k_B is the Boltzmann constant, and T is temperature [155]. Molecules approach kinks, which are immobile, only

from half the space above the crystal (Figure. 51) and the kinks along the steps separate, on the average, by $\overline{n_k}$ molecules [156]. These three restraints modify the Smoluchowski expression [157] for k_0 to $k_0 = 2\pi D r^* N_A/\overline{n_k}$ (D, etioporphyrin I diffusivity; $r^* \cong 0.5$ nm, reaction radius; and N_A, the Avogadro number). In turn, $D = k_B T/6\pi\eta a$. The restraints on a reaction at a kink and the elevated viscosities of the organic solvents depress the values of k_0 to order 10^8 $M^{-1}s^{-1}$, somewhat lower than the typical values of about 10^{10} $M^{-1}s^{-1}$ for diffusion-limited reactions of small molecules dissolved in water [155]. The relations for k_0 and D expectedly imply that k_a scales as η^{-1} and, importantly, the activation barrier for solute incorporation into kinks $\Delta G^{\ddagger}$ solely regulates the product $k_a\eta$. The established correlation between $\Delta G^{\ddagger}$ and $k_a\eta$ affords an opportunity to use the $k_a\eta$ data to illuminate the mechanisms that govern $\Delta G^{\ddagger}$. Classical crystal growth theories assign $\Delta G^{\ddagger}$ to an activated complex, in which solute-solvent bonds are broken, but the solute has not yet bound to the kink [35,36]; for etioporphyrin I this complex is identical in all solvents. Then the activation free energy for incorporation is instituted by the strength of the solute – solvent bonds and is greater in solvents that bind strongly with the solute (Fig. 50a).

Table 4: Diffusion limited rate in different solvents.

Solvent	$\boldsymbol{K_o}$ $\boldsymbol{(M^{-1}s^{-1})}$
DMSO	$1.68*10^8$
Butanol	$1.35*10^8$
Hexanol	$7.63*10^7$
Octanol	$4.52*10^7$

The following are the determined values of the activation energy barrier.

Table 5: Activation energy barrier in different solvents.

Solvent	Activation energy barrier E_a (kJM^{-1})
DMSO	14.3±0.11
Butanol	13.0±0.25
Hexanol	13.0±0.14
Octanol	13.0±0.06

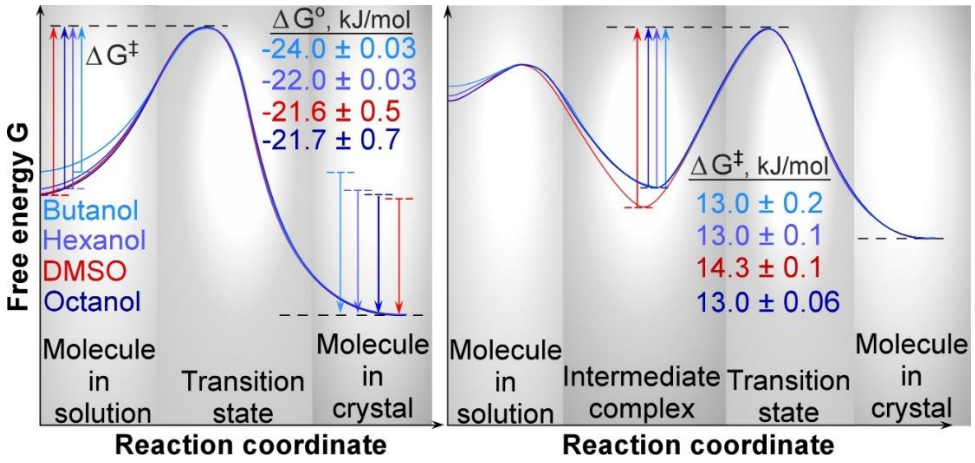

Figure 51: Schematic of the free energy landscape along the accepted pathway of incorporation of an etioporphyrin I molecules from the solution into a kink. **a.** The values for the standard free energy of crystallization ΔG^o are from Ref. [76]. **b.** Schematic of the free energy landscape along the pathway of incorporation suggested by the free energy barriers for incorporation into kinks $\Delta G^{\ddagger}$ in the four solvents.

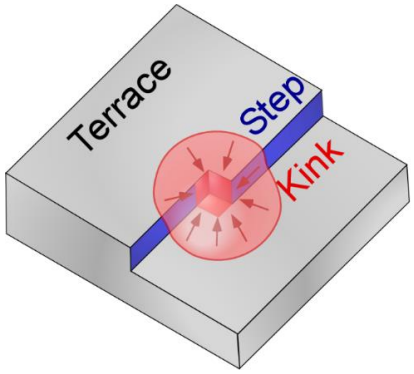

Figure 52: Molecules approach the kink from half space.

To test the validity of this proposal, we use that etioporphyrin I crystallizes as identical P1 crystals (Fig 41b, d) from all four solvents. In consequence, the equilibrium free energies of crystallization ΔG^o, evaluated from the respective solubilities [76], characterize the relative strengths of the solute-solvent interactions in each solvent. A correlation between ΔG^o and $\Delta G^{\ddagger}$ would exemplify the venerable Berthollet rule, according to which more stable solute-solvent complexes should decay slower [158]. Etioporphyrin I, however, defies both the Berthollet rule and the classical understanding of activation barriers for solution crystallization. It binds weakly to butanol and its interactions with DMSO, hexanol, and octanol are stronger and nearly equal [76]. The classical principles concertedly predict lowest activation barrier and fastest growth from butanol solutions and comparable growth rates from DMSO, hexanol and octanol. The AFM results on the step velocities belie both parts of this prediction after accounting for the divergent viscosities of the solvents (figure 44). The discrepancy between the interactions of etioporphyrin I with the solvents, manifest as ΔG^o, and the activation barriers for crystallization $\Delta G^{\ddagger}$ advocates for a metastable state that a solute molecule occupies before it invades a kink. This stability of this state dictates the height of the barrier that the solute molecule overcomes as it relocates to the kink. Interactions with the solvent stabilize this intermediate complex and define the distinct rates of growth in different solvents. The values of $\Delta G^{\ddagger}$ in the four solvents imply that DMSO strongly stabilizes the intermediate state and the contributions of the three alcohols are weaker and close (Figure. 50b). This intermediate complex locates along the direct access route of a molecule from the solution to a kink (Figure. 51) and likely represents a state in which the solute molecule is bound, but only partially, to the molecules comprising the kink.

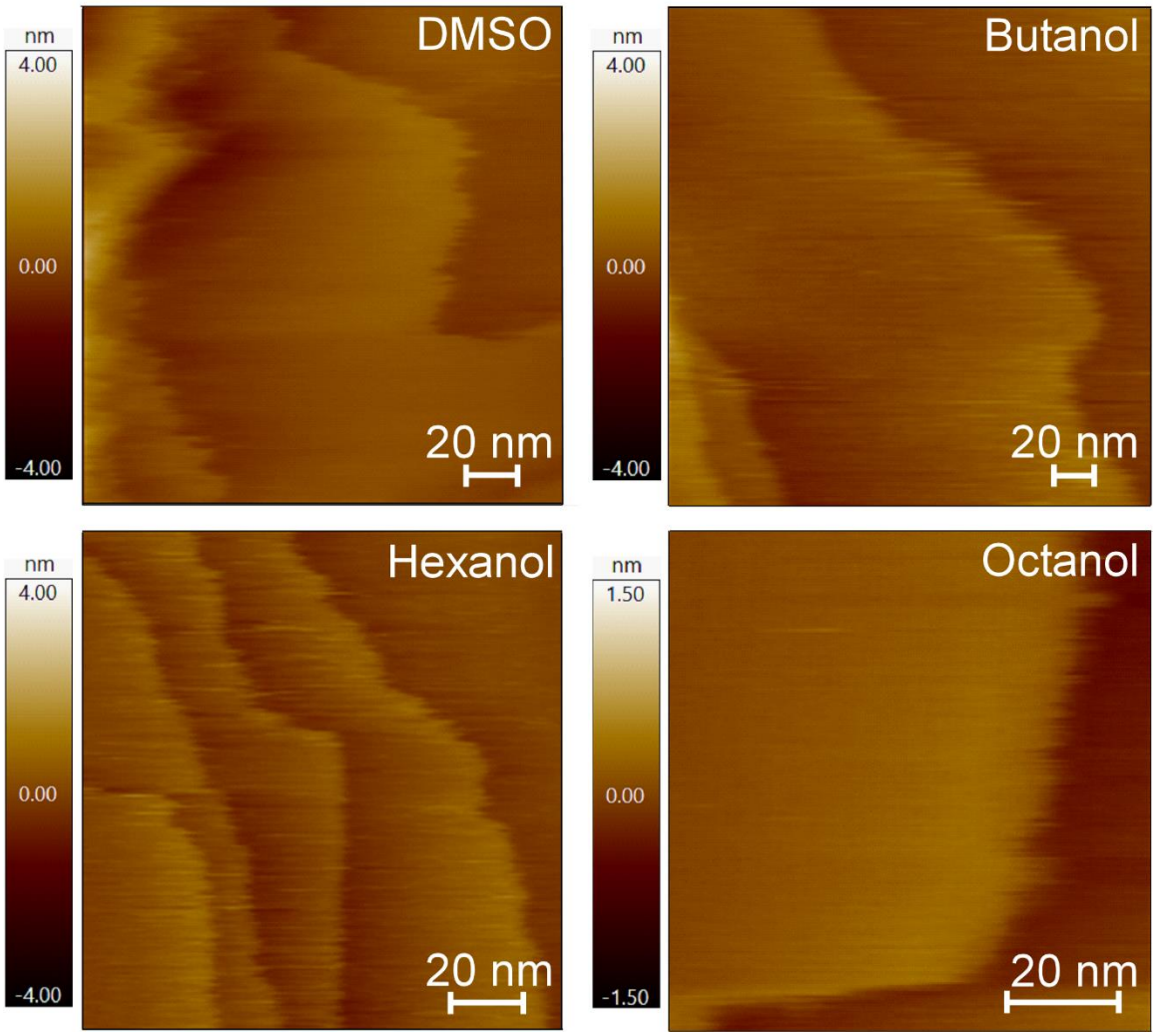

Figure 53: Kink density on the (010) face of etioporphyrin I. The kink density in hexanol and butanol are close to 0.3, the thermodynamic limit. The same is seen for octanol and DMSO.

5.6 M.D. Simulation of Free Energy Profile for Solute Incorporation into Kinks

For a microscopic view on the pathway from the solution into a kink, we undertook all-atom molecular dynamics simulations, complemented by advanced sampling methods. We modeled an etioporphyrin I molecule in the vicinity of a kink (Figure. 53a) in contact with the four solvents. Upon departure from a kink along the vertical *z* axis, the molecule mostly

preserves its orientation for $\Delta z \approx 0.7$ nm (Figure. 53 b, c). In all solvents, the potentials of mean force along the departure route feature a secondary minimum at $\Delta z \approx 0.2$ nm (Figure. 53b – d). Etioporphyrin molecules in this minimum locate higher than at the global minimum of $F(z)$, where they fully integrate in the kink (Figure. 39d, inset). This shift creates a ca. 0.2 nm gap between the incoming molecule and the lower molecule of the kink (Figure. 53d, inset). Entropy maximization requires that the gap fills with solvent. The smaller DMSO readily complies and the energy of the bonds that it forms with the etioporphyrin I molecules framing the gap adds to the entropy increase to stabilize the intermediate state. The larger molecules of butanol, hexanol, and octanol, however, fit poorly in the small space temporarily left open by the incoming molecule (Figure. 39d, inset) and the intermediate state in these solvents retains higher free energy. The intermediate complex represents the stepping stone from which a molecule launches to surmount the activation barrier and its lower free energy in DMSO enforces higher $\Delta G^{\ddagger}$ (Figure. 53d). The less stable intermediate complexes in the three alcohols define lower $\Delta G^{\ddagger}$s than in DMSO (Figure. 53d) and contribute to faster growth.

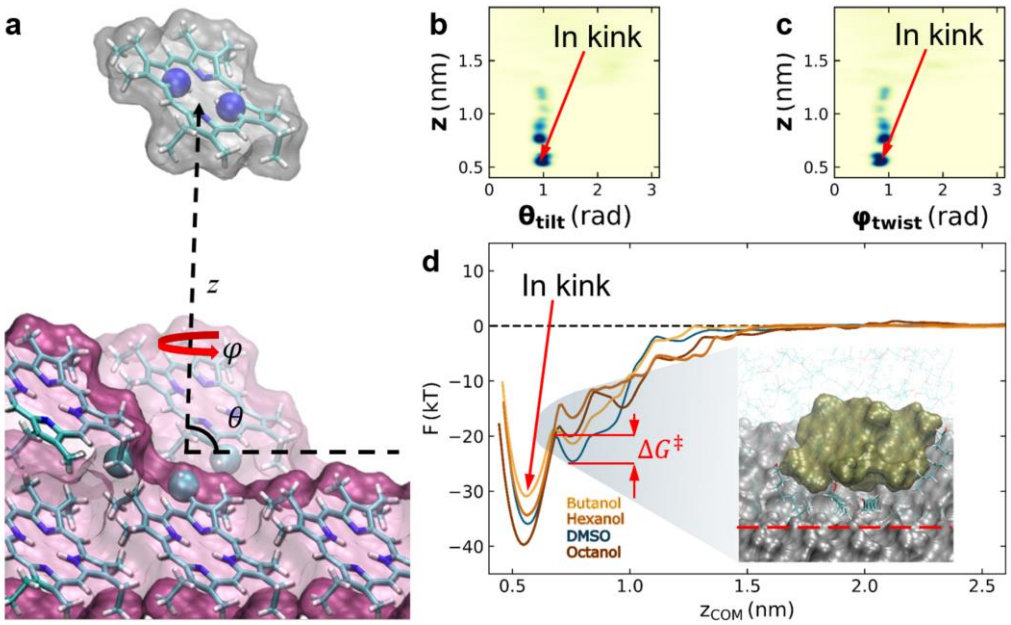

Fig. 54: Microscopic view of the ingress of an etioporphyrin I molecules into a kink. a. A molecule, shown as gray surface accessible to a solvent with diameter 0.14 nm, on approach to a kink, viewed along the missing half row of molecules along the step and shown as purple (molecules in the front plane) and pink (molecules in the rear plane) surface accessible to a solvent with diameter 0.14 nm. **b, c.** The probability densities of the angles θ and ϕ as a function of z. **d.** The potential of mean force F for the incorporation of etioporphyrin I in the four solvents.

Inference

In summary, the mechanism of molecular association to kinks that passes via an intermediate state, in which the incoming solute molecules only partially attach to the molecules in the kink, presents a new paradigm of molecular crystallization. The proposed model highlights the fine details of solute – solvent interactions that rely on solvent size as a parameter–complementary to solvent structure–to guide solvent selection and solute - solvent matching to optimize the synthesis of advanced functional organic materials. Among the remaining open questions are whether an intermediate state precedes the incorporation into kinks of solute adsorbed on the crystal surface; if more than one intermediate states are possible; if in the intermediate state may recruit more than one of

the incoming solute molecules; and about the structure of the intermediate state of solutes of irregular shapes and flexible configurations.

Chapter 6: Crystal Growth Inhibitors Employ Dual Mode of Action

Crystallization is an essential step in many biological, geological natural and industrial processes. Promotion or inhibition of crystallization in both natural and engineered environments by soluble foreign compounds are deployed that interact with the solute or the crystal-solution interface[3]. In many cases several modifiers act to inhibit or promote growth and attain desired physico-chemical properties of crystalline materials[159]. Molecular-level insights into the mechanisms of modifier actions help us design efficient processes with desired product quality or controlling pathological crystallization[52,160]. Impurities or modifier's effect on crystal growth can either be desirable or undesirable[5,6,134,161-165]. Industrial crystallization is mostly a purification process, and impurities pose problem to downstream processing like tableting, manufacturing etc. Crystal habit modification by modifiers are used extensively for making zeolites and pharmaceutical drugs. Pharmaceutical drugs are synthesized in crystalline form due to their steady release rate. Industrial manufacturing is prone to exposure towards impurities and upstream processing can lead to the presence of impurities in the downstream process, which can affect the physico-chemical properties of drugs. A good molecular mechanistic understanding of modifier action will help us void unnecessary contaminations and formulate better therapeutics for several pathological diseases. Recent works on modifiers has tried to identify modifiers as kink blockers, step pinners depending on their molecular mechanism of action. Step pinners bind to flat terraces and arrest crystal formation over broad areas of the crystal surface[148,162] Alternatively, kink blockers were found to block kinks, the sites where solute molecules incorporate into steps[162] Even though drug formulations with combinations of two or inhibitors are common in many drugs [166], a

crucial gap in the understanding of interactions between modifiers and crystal has been identified [167,168] and needs to be addressed. We examine the growth of etioporphyrin I crystals, in presence of protoporphyrin IX as an impurity. Both etioporphyrin I and protoporphyrin IX are free base porphyrins which mimic the real-world scenario where chemically similar molecules act as impurities[169]. The idea of this work is to understand the molecular mechanisms of etioporphyrin I inhibition by protoporphyrin IX. For the first time we wanted to prove the validity of Cabrera -Vermilya (C-V) model when the modifier acts both a step pinner and kink blocker and show the deviation from C-V model near the dead zone where growth is governed by stochastic fluctuations. We observed that etioporphyrin I crystal growth follows classical mechanisms whereby new layers nucleate on the crystal surfaces and advance by incorporation of solute molecules at the steps. These studies uncovered that some modifiers depending on their molecular size, chemical nature and interactions can act both as step pinners and kink blockers.

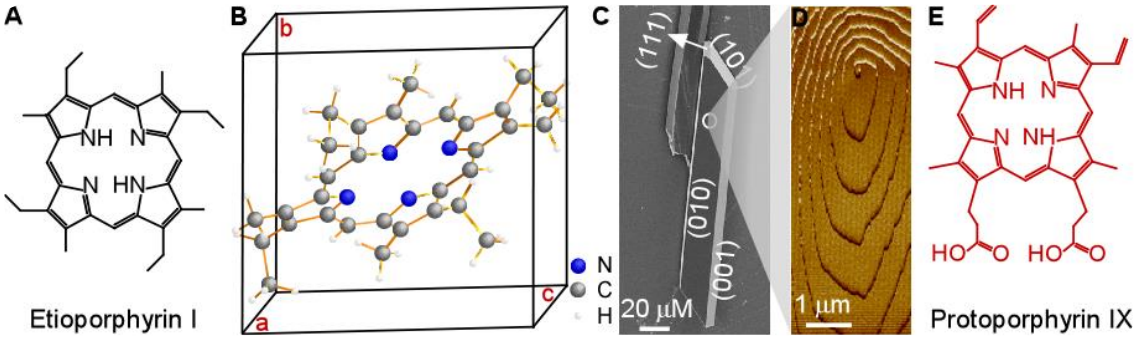

Figure 55: Etioporphyrin I crystal and protoporphyrin IX. A. Etioporphyrin I molecule. **B.** Crystal structure in P1 space group; Cambridge Structural Database REFCODE WOBVUF[8]. **C.** Scanning electron micrograph of crystals of etioporphyrin I grown in octanol showing different faces identified using single crystal XRD. **D.** *In-situ* Atomic Force Microscopy image of (010) face of etioporphyrin I showing steps emerging from a dislocation with 1 nm step height. **E.** Protoporphyrin IX, free base porphyrin used as a modifier.

To address the molecular mechanism of inhibition by a chemical homologue we study the inhibition of etioporphyrin I crystal growth by protoporphyrin IX. Protoporphyrin IX is used as a model organic porphyrin molecule to test the effect of other homologous free base porphyrin on the crystallization kinetics and crystal habit Etioporphyrin I.

6.1 Effect of Protoporphyrin IX on Bulk Etioporphyrin I Crystallization

Due to crystal anisotropy, inhibitor molecules binding to crystal surfaces exhibit marked differences in inhibition of growth in different crystallographic directions. To assess the anisotropic growth rates, we perform bulk crystallization studies to determine the macroscopic dimensions of etioporphyrin I crystals grown for 2 days at varying protoporphyrin IX concentrations (Fig. 4 C and D); these experiments were carried out at C_{EtP} = 0.40 mM and at supersaturation $\sigma = \ln(C_{EtP}/C_e) \cong 1.04$, where C_e = 0.14 mM is the solubility at 25 °C. Protoporphyrin IX leads to preferential inhibition of the axial faces (101) and (111) of etioporphyrin I leading to the reduction in *l* and lateral faces (001) leading to the reduction of crystal width. We see a reduction in crystal length and width and subsequent vanishing of the (101) and (111) face. The presence of protoporphyrin IX lead to the increase in crystal number density acting as heterogenous neucleation sites. Tapering has been attributed[170] to blocking of steps on an orthogonal face on approach to a shared edge, induced by enhanced supply of inhibitors at the edge, as illustrated in Figure 55 M. The symmetric tapering in Figure 55 H and I indicate that protoporphyrin IX interacts with both (111) and (101) faces.

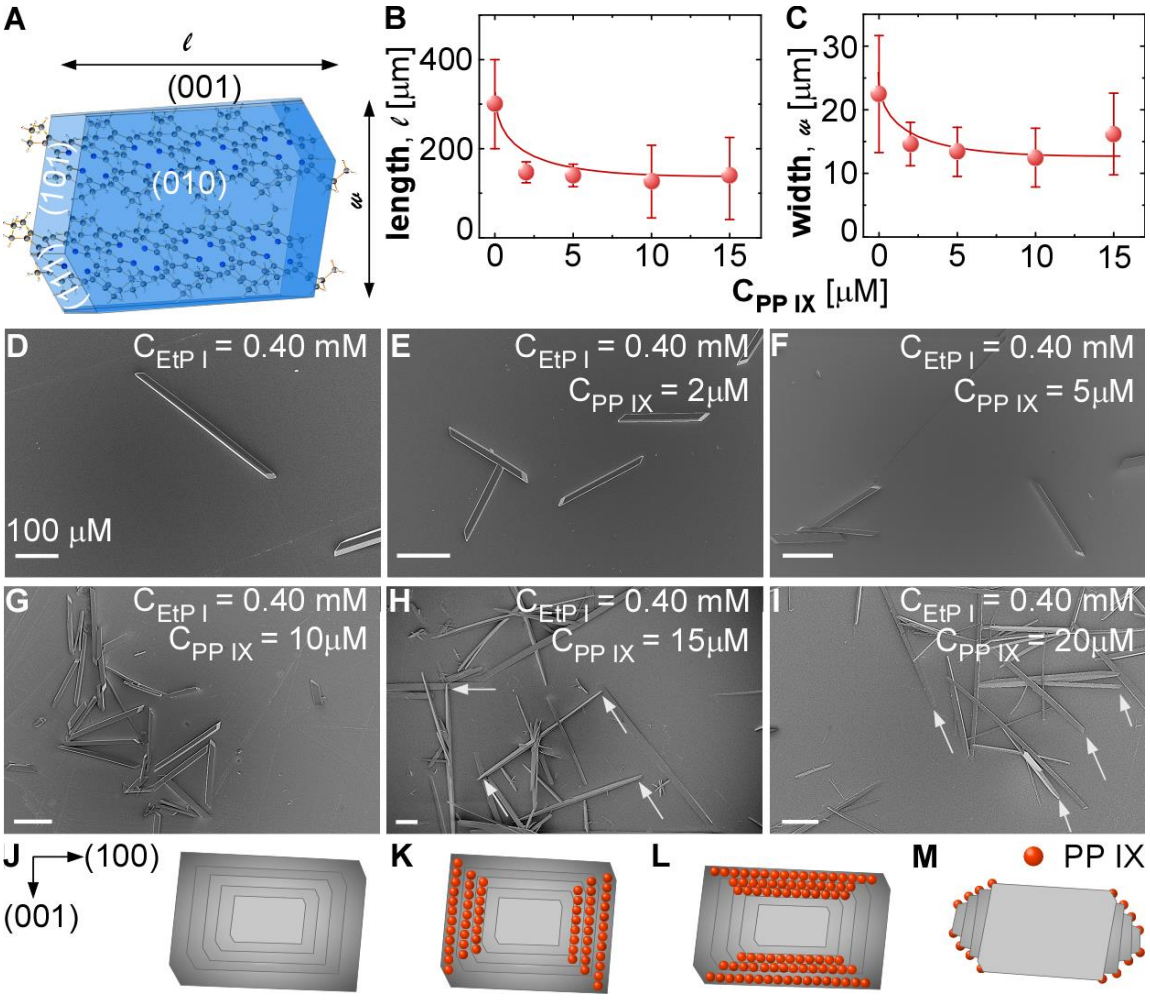

Figure 56. Effect of protoporphyrin IX on etioporphyrin I crystal size and morphology. **A.** BFDH morphology of etioporphyrin I crystal calculated using Mercury **B and C.** Variation of average length, *l* and width, *w* of etioporphyrin I crystals grown in pure octanol and in presence of increasing protoporphyrin IX concentrations obtained by slow cooling. **D-I.** Scanning electron micrographs of etioporphyrin I crystals grown in absence **(D)** and presence of different protoporphyrin IX concentrations listed in each panel. **J-M** Illustrations of modification of the crystal habit. J. Control and protoporphyrin IX induced suppression of crystal l and w by interactions with lateral (K) and axial (L) crystal faces, respectively. (M) Tapering due to enhanced adsorption of drugs near the crystal edges.

6.2 Lack of Complexation Between Etioporphyrin I and Protoporphyrin IX

To test the hypothesis if the inhibition of etioporphyrin I crystal growth is due to the sequestration of etioporphyrin I in soluble complexes of etioporphyrin I with protoporphyrin IX we study the Uv-vis absorption spectrum of etioporphyrin I and

protoporphyrin IX. Using the Beer's Law $A = \varepsilon CL$, where A is the absorbance, ε, is the extinction coefficient, C is the concentration and L is the path length. Our findings refute the hypothesis that that any complex form between etioporphyrin I and protoporphyrin IX. This crystal growth inhibition we see in the bulk crystallization experiments is not due to sequestration of etioporphyrin I in soluble complexes but due to the inhibition of layers on etioporphyrin I crystal surface. The Uv-vis spectrum is additive in nature and the $R^2 = 1$ for the correlation between calculated and observed absorbance values at a wavelength of 496 nm.

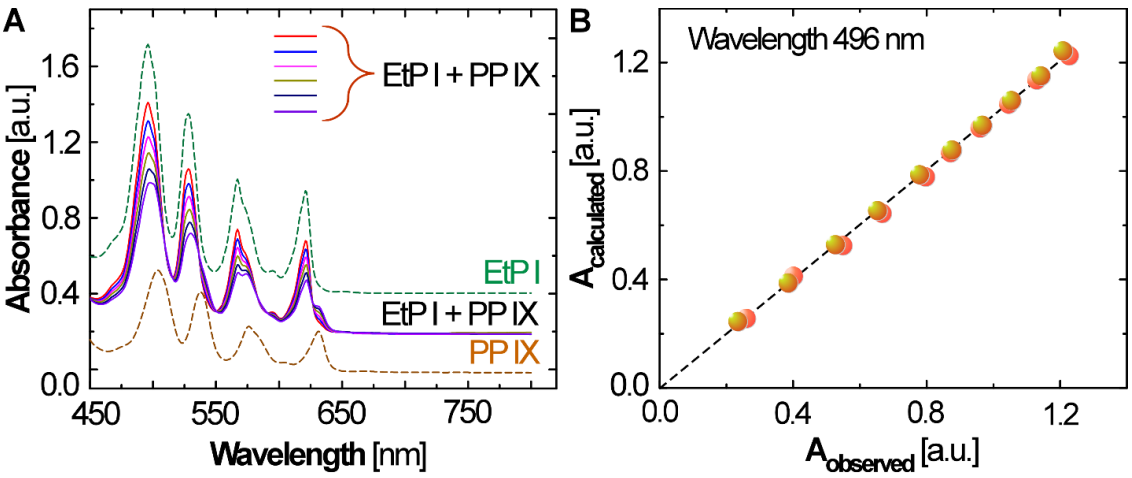

Figure 57: Lack of complexation between etioporphyrin I and protoporphyrin IX. A. Uv-vis spectrum of etioporphyrin I and protoporphyrin IX in octanol. The individual spectrums of etioporphyrin I and protoporphyrin IX when added give the combined spectrum indicating the lack of complexation. **B.** Linear correspondence between observed and calculated spectrum of protoporphyrin IX and etioporphyrin I with $R^2 = 1$ again emphasises the absence of complexation.

6.3 Molecular Mechanism of Protoporphyrin IX Action

Etioporphyrin I are triclinic crystals belonging to the P1 space group with unit cell parameters a= 6.88 Å, b = 9.91 Å, c = 10.35 Å and a = 88.47 °, b = 79.70 °, c = 77.44°. We studies the tangential step velocity on the (010) face of etioporphyrin I crystal in presence of protoporphyrin IX.

The (010) face of etioporphyrin I crystals grow by spreading of layers from a screw dislocation center as illustrated in figure 58A. The step height is 0.99 ± 0.02 nm. The possible areas of inhibition are the kinks figure 57B or flat terraces between steps figure 57A. A study of the literature shows various mechanisms of inhibition kink blocking[134], step pinning[134], dissolution due to strain[3]. The understand the mechanism of inhibition of one free base porphyrin due to another free base porphyrin, these scenarios are quite common in industrial or the natural environments where homologues can act as inhibitors.

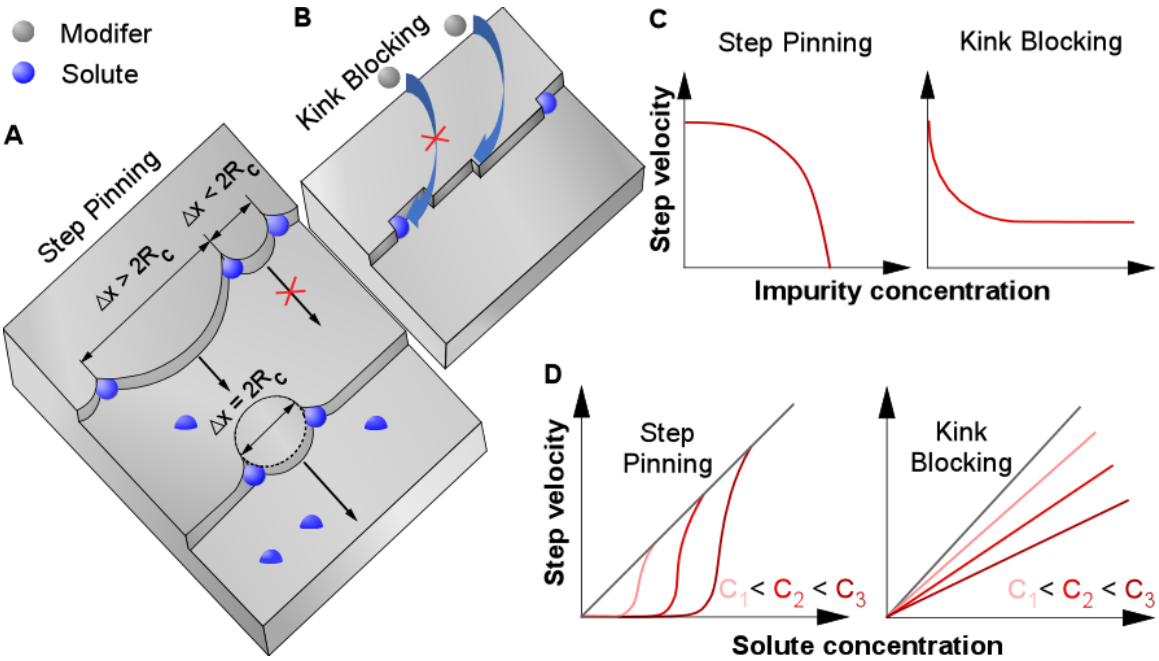

Figure 58: Step pinners and kink blockers. A and **B.** Schematics showing step propagation inhibition in presence of step pinners and kink blockers. Step pinners adsorb on the terraces thus curving the propagating steps. Kink blockers getting incorporated into the kinks inhibit solute incorporation. **C.** Step velocity variation with increasing impurity concentration at constant solute concentration in presence of step pinners and kink blockers. **D.** Schematic representation of step velocity variation with solute concentration at constant impurity concentration. Kink blocking leading to a decrease in the step kinetic coefficient and step pinners increases the dead zone width, where $C_1 < C_2 < C_3$.

We measured the step velocity of etioporphyrin I at C_{EtP} = 0.35 mM, at different increasing protoporphyrin IX concentrations figure 58D. The resultant curve exhibits the

nature of a kink blocker, but kink blockers does not lead to complete step inhibition due to fast kink dynamics. The step anisotropy changes in presence of protoporphyrin IX and at 5μM of protoporphyrin IX concentration the steps undergo complete inhibition, these are the characteristics of a step pinner. To understand the molecular mechanism of protoporphyrin IX action we studied the step velocity variation at several increasing concentration of etioporphyrin I and in absence and presence of 1.5 μM of protoporphyrin IX figure 59A. The purple curve represents the step velocity in absence of impurities, but with increasing etioporphyrin I concentration. The red line are the step velocities at increasing etioporphyrin I concentration keeping the impurity concentration constant at 1.5μM. Even when the concentration of etioporphyrin I is 400 times the impurity concentration the step velocities are lower than the control. We see the presence of a dead zone. Indicating that homologous molecules act both as step pinner and kink blocker. The study the accumulation of PPIX over time, a steady step velocity indicates that accumulation of PPIX is negligible as shown in figure 58.

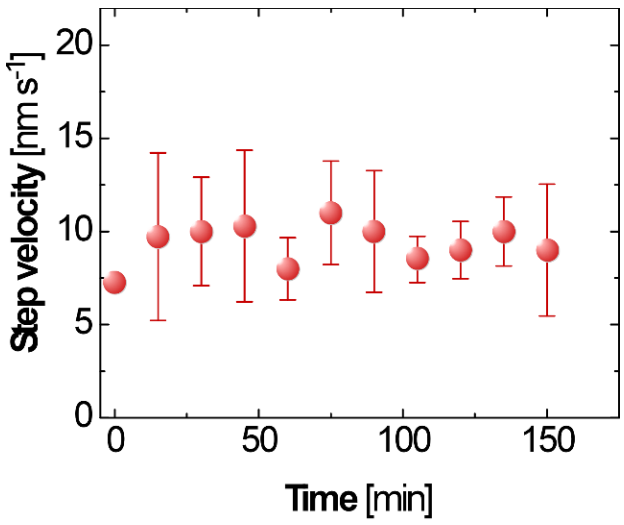

Figure 59: Lack of strain generation due to protoporphyrin IX accumulation. Step velocity at C_{EtP} = 0.35 mM and PPIX concentration 1.5 μM.

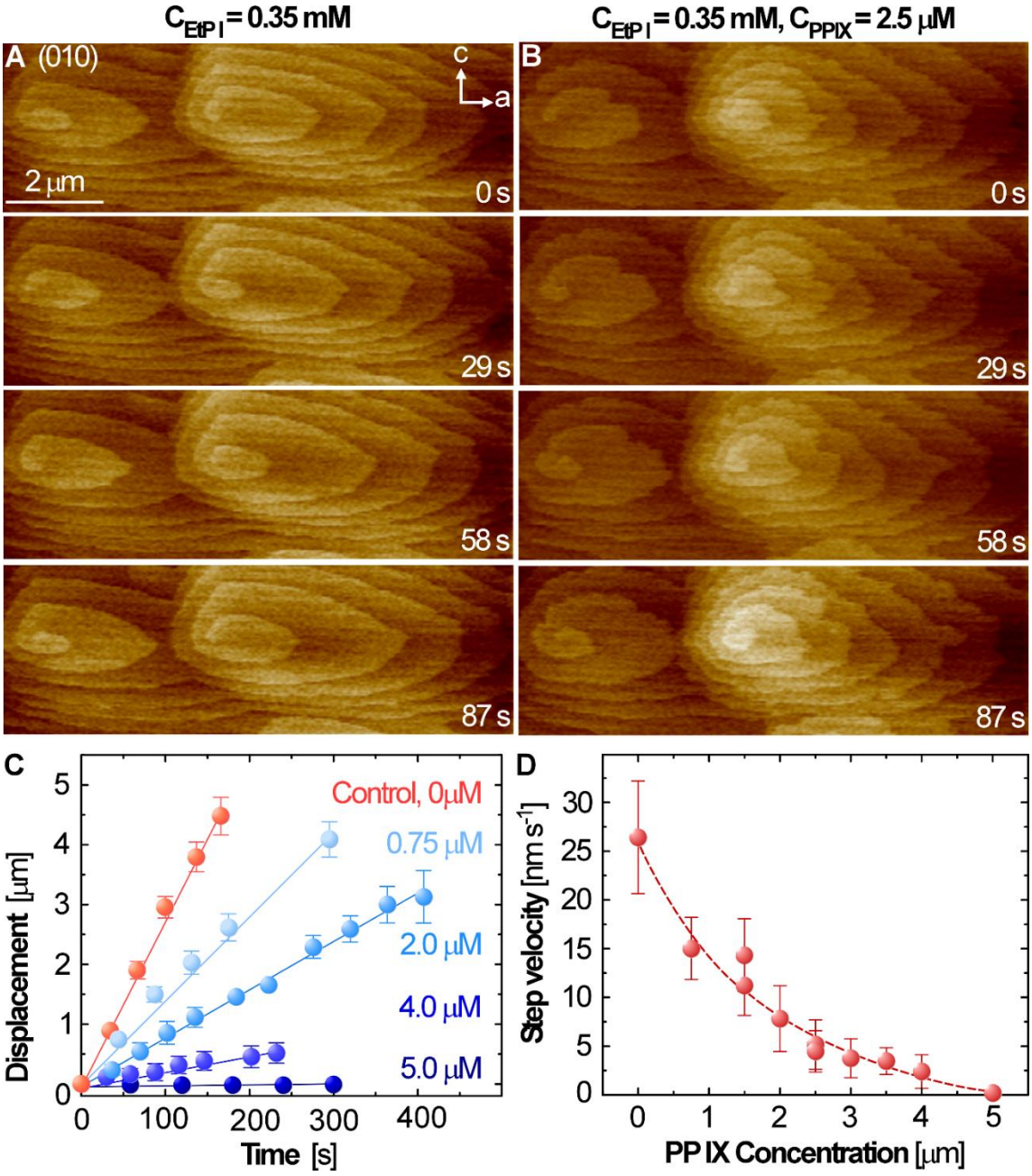

Figure 60: Etioporphyrin I step velocity variation in presence of protoporphyrin IX. A. Time resolved *In-situ* Atomic Force Microscopy monitoring of (010) face of etioporphyrin I at C_{etpI} =0.35 mM. **B.** Step displacements in presence of C_{etpI} =0.35 mM and C_{PPIX} = 1.5µM. **C.** Step displacements measured at varying impurity concentration. **D.** Step velocities measured at varying impurity concentration and constant etioporphyrin I concentration (C_{etpI} = 0.35 mM).

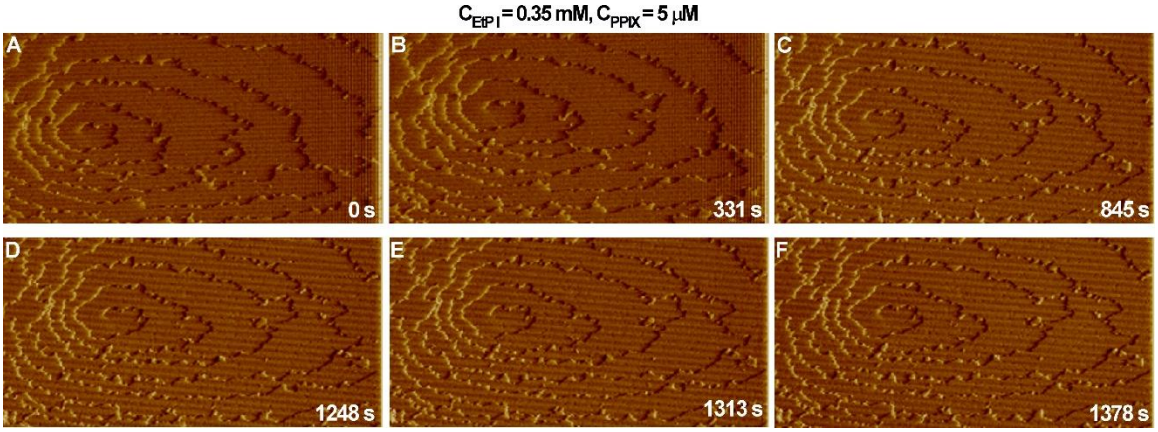

Figure 61: Inhibition of layers at protoporphyrin IX concentration 5μM.

Figure 60 shows the inhibition of layers of etioporphyrin I on the (010) face. Protoporphyrin IX inhibits the layer growth by step pinning and kink blocking mechanism. A impurity concentration of 5 μM completely inhibits step propagation and stops growth. The disparity we see in bulk and AFM inhibition is since in AFM there is molecular level inhibition but in bulk crystallization several factors are at play, the bulk concentration, local concentration profile around the crystals.

6.4 Development of Kinetic Model for Step Pinners and Kink Blockers

We develop the Cabrera - Vermilya model to predict the step kinetics in presence of impurities which act as both step pinner and kink blockers. We consider the motion of steps governed by three phenomena: 1. Step curvature imposed by impurity molecules adsorbed on the terraces as step pinners; the chemical potential of curved steps is elevated [171], enforcing lower effective supersaturation and slower step growth. 2. Impurity molecules as kink blockers, which bar association of solute molecules to some of the kinks, and 3. Decrease of the surface free energy γ of the step edges that regulates how they respond to greater curvature.

To evaluate $\Delta\gamma$, we assume that $n_{s,B}$, the density of kinks occupied by adsorbed kink blockers, is equal to the number of blocker molecules adsorbed at the kinks. With this assumption, $n_{s,B}$ complies with the Gibbs equation of adsorption[171].

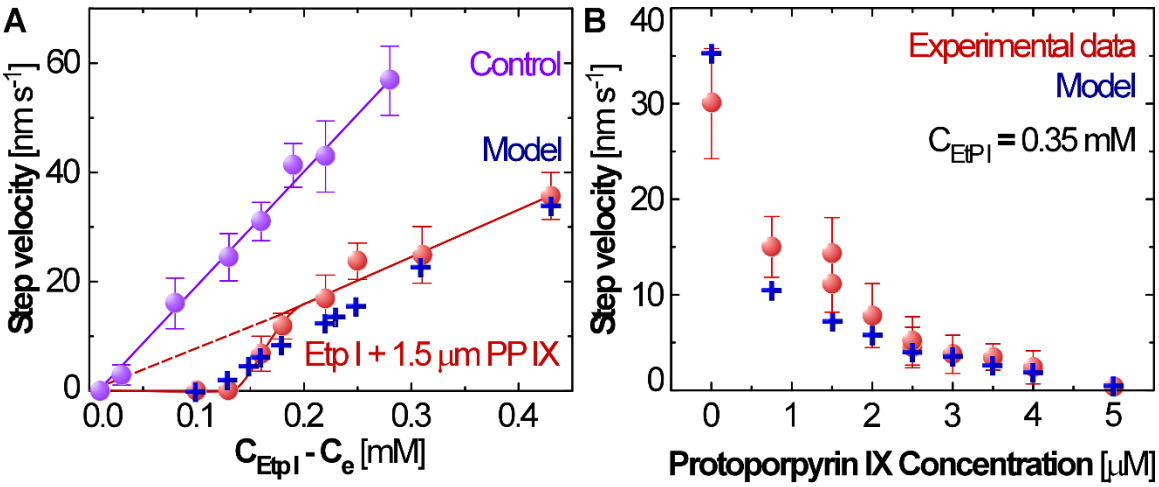

Figure 62: C-V Model fit and experimental data of step velocities at constant impurity and varying impurity concentration.

It is given as,

$$\frac{n_{s,B}}{a} = -\frac{d\gamma}{d\mu_B}, \tag{15}$$

where a is the step height and μ is the chemical potential of the inhibitors in the solution. Owing to the low inhibitor concentrations, the interactions between inhibitor molecules are weak and $\mu_B = \mu_{B0} + k_B T \ln c_B$, where μ_{B0} is the standard value of μ_B, k_B is the Boltzmann constant and T is temperature. The sum of occupied and free kinks $n_{s,B} + n_{k,B} = n_{k,0}$ and $n_{s,B} = \theta_B \xi n_{k,0}$.

We integrate the Gibbs equation and substitute the relations for $n_{s,B}$ and μ_B to obtain

$$-\Delta\gamma = \int_0^{c_B} \frac{n_{s,B}}{a} d\mu_B = \int_0^{c_B} \frac{\theta_B \xi n_{k,0}}{a} k_B T d \ln c_B = \int_0^{c_B} \frac{K_{LB}}{1+K_{LB}c_B} \frac{n_{k,0}\xi}{a} k_B T dc_B \tag{16}$$

and

$$-\Delta\gamma = \frac{k_B T \xi n_{k,0}}{a} \int_0^{c_B} \frac{K_{LB} dc_B}{1+K_{LB}c_B} = \frac{k_B T n_{k,0}}{a} \xi \ln(1 + K_{LB}c_B)\,. \tag{17}$$

On the (010) faces of etioporphyrin I crystals the step height $b \cong 1.0$ nm[8]. The characteristic molecular length is 0.68 nm in the $\vec{a}$ direction and 1.03 nm in the $\vec{c}$ direction[8]. The kink density along the step is high and can be approximated as the reciprocal average of these two lengths, leading to $\frac{n_{k,0}}{a} \approx 10^{18}$ m^{-2}. With this, the constant in Eq. (17) that is independent of the nature of the inhibitor is $\frac{k_B T n_{k,0}}{a} \approx 4 \times 10^{-3}$ J m^{-2}.

We define the supersaturation as $\Delta\mu = k_B T \ln(c_{EtP}/c_e)$, where $\Delta\mu = \mu - \mu_e = \mu - \mu_c$, μ, μ_e, and μ_c being the chemical potentials of the solute in the growth solution, in the solution at equilibrium with the crystal, and in the crystal, respectively; c_{EtP} is are the solute concentration; and c_e is its solubility. This definition relies on the assumption that the ratio of solute activity coefficients in the supersaturated solution and at equilibrium is close to one. For brevity we introduce σ, defined as $\sigma \equiv \Delta\mu/k_B T = \ln(c_{EtP}/c_e)$. According to transition state theory the rate of a reversible chemical reaction is proportional to $\left(\exp\frac{\Delta\mu}{k_B T} - 1\right)$ Accounting for geometric factors and for the change in molecular density upon crystallization, the step velocity relates to the supersaturation as

$$v = \beta\Omega c_e \left(\exp\frac{\Delta\mu}{k_B T} - 1\right) = \beta\Omega(c_{EtP} - c_e), \qquad (18)$$

where Ω is the molecular volume in the crystal, and β is the kinetic coefficient [35,36]. Linear $v(C)$ correlations have been recorded for numerous crystals growing in supersaturated solutions of solute only [38].

We assume the step pinners adsorb on the crystal surface with molecular surface concentration $n_P = \theta_P/S_0$, where θ_P is the surface coverage and S_0 is the area per adsorption site. For inhibitors with molecular size commensurate with that of the solute, S_0 is the dot

product of the two lattice vectors parallel to upward facing crystal face. We evaluate the average distance between stoppers as

$$L = n_P^{-0.5} = \sqrt{S_0/\theta_P}. \tag{19}$$

To evaluate θ_P, we assume that adso.rption follows the Langmuir relation between θ_P and the solution concentration of the step pinners c_P,

$$\theta_P = K_{LP}c_P/(1 + K_{LP}c_P), \tag{20}$$

where K_L is the respective Langmuir constant. We assume that pinners separated by distance L enforce step curvature with radius $R = L/2$. We obtain

$$R = \frac{1}{2}\sqrt{S_0 \frac{1+K_{LP}c_P}{K_{LP}c_P}}\ . \tag{21}$$

According to the Gibbs-Thomson relation, a step with radius of curvature R is in equilibrium with a solution of concentration c_{eR}, which is greater than the equilibrium concentration of a straight step c_e by

$$\ln\left(\frac{c_{eR}}{c_e}\right) = \frac{\Omega\gamma}{Rk_BT}, \tag{22}$$

where γ is the surface free energy of the step edge. Eq. (15) reverses the familiar application of the Gibbs-Thomson relation to define the radius R_c of a two-dimensional cluster in equilibrium with a solution with concentration c_H greater than the solubility c_e

$$R_c = \frac{\Omega\gamma}{k_BT\ln(c_{EtP}/c_e)}. \tag{23}$$

Unifying Eqs. (14) and (15), we obtain an expression for the critical supersaturation σ_d, below which a step cannot penetrate the inhibitor fence and growth ceases

$$\sigma_d = \ln\left(\frac{c_{eR}}{c_e}\right) = \frac{2\Omega\gamma}{k_BT}\sqrt{\frac{1}{S_0}\frac{K_{LP}c_P}{1+K_{LP}c_P}}. \tag{24}$$

The supersaturation range between 0 and σ_d , in which step growth is arrested, is often called "the dead zone". This expression for σ_d is identical to the one derived by Weaver and De Yoreo [172,173].

From Eq. (15), the solution concentration at equilibrium of a curved step with radius is

$$c_{eR} = c_e \exp\frac{\Omega\gamma}{Rk_BT}, \tag{25}$$

At a concentration $c > c_{eR}$, a step with radius of curvature R grows with velocity

$$v_R = \beta\Omega(c_{EtP} - c_{eR}) = \beta\Omega\left(c_{EtP} - c_e \exp\frac{\Omega\gamma}{Rk_BT}\right) = v_\infty \frac{c_{EtP} - c_e \exp\frac{\Omega\gamma}{Rk_BT}}{c_{EtP} - c_e}, \tag{26}$$

where v_∞ is the velocity of a straight step, defined in Eq. (11). An equivalent form of this relation, derived by Weaver, *et al.* [172], is

$$v_R = v_\infty\left(1 - \frac{e^{\sigma_d} - 1}{e^{\sigma} - 1}\right). \tag{27}$$

Introducing the step pinning mechanism of inhibitor action, Cabrera and Vermilyea [174] evaluated the effective step velocity as the geometric mean of the maximum velocity, corresponding to uninhibited step propagation in the gaps between the stoppers and following the kinetic law in Eq. (18) and, and the minimum v due to stopper inhibition according to Eq. (26). In the resulting step motion law, this mode of averaging invoked an exponent of ½ on the expression in parenthesis in Eq. (26). Instead of using the geometric mean, subsequent models assume that the measured step velocity corresponds to an arithmetic mean [175] or just to the minimum velocity expressed by Eq. (26) [105]. The impact of additional factors—kink blocking by the pinners, step anisotropy, variable step curvature [176], stopper mobility, slow stopper adsorption, and others—on the correlation between the step velocity and the surface distribution of step pinners is summarized in Lee-Thorp, *et al.* [177]. Even the most elaborate models fail to predict quantitatively experimentally

measured $v(c_P)$ correlations [177]. Importantly, recent solid-on-solid kMC results reveal that uniformly distributed pinners inhibit moving steps to the same degree as randomly positioned pinners of the same surface concentration, i.e., the surface distribution of step pinners has no effect on the step velocity [178]. To avoid the ambiguity associated with averaging inhibited, partially inhibited, and uninhibited step velocities, below we only model the effects of kink blockers on the velocity of steps with greatest curvature enforced by step pinners, v_R. The evaluated v_R, contained by step pinners at concentration c_P would correspond to the measured step velocity if the approximation introduced De Yoreo [173] and Weaver, *et al.* [172 105], that $v = v_R$ and follows Eqs. (26) and (27), is valid.

Combining Eq. (26) with Eq. (21) on the relation between the step radius of curvature R, dictated by the surface concentration of step pinners, and the bulk concentration of step pinners c_P engenders a relation between the v_R and c_P

$$v_R = \frac{v_\infty}{c-c_e}\left(c_{EtP} - c_e \exp\frac{2\Omega\gamma}{k_BT}\sqrt{\frac{K_{LP}c_P}{S_0(1+K_{LP}c_P)}}\right). \quad (28)$$

According to Eq. (21), the velocity $v_R$of a step with curvature R enforced by step pinners with solution concentration c_P decreases monotonically from v_∞ at $c_P = 0$ and $R = \infty$ to zero as c_P increases.

Kink blockers present in the solution at concentration c_B, which adsorb to the kinks with Langmuir constant K_{LB}, impact step motion in two ways: 1. they diminish the number of kinks available for solute association, and 2. they lower the surface free energy of the step edge. These two consequences can be quantified by Eqns. (17) and (26), respectively, leading to

$$v_R = \beta\Omega\left(1 - \xi\frac{K_{LB}c_B}{1+K_{LB}c_B}\right)\left(c_{EtP} - c_e \exp\left(\frac{2\Omega}{k_BT}\left(\gamma_0 - \frac{k_BTn_{k,0}}{a}\xi \ln(1 + K_{LB}c_B)\right)\sqrt{\frac{K_{LP}c_P}{S_0(1+K_{LP}c_P)}}\right)\right), \quad (29)$$

where $v_0 = \beta\Omega(c_{EtP} - c_e)$ is the step velocity in the absence of both step pinners and kink blockers and γ_0 is the surface free energy of the step edge in the absence of kink blockers. Here $c_P = c_B$, as kink blocker and pinner are same. We assumed ξ=0.5. β in absence and presence of impurities were calculated as 0.448 mm/s and 0.2mm/s respectively. γ was calculated from the Turnbull rule $\gamma = \frac{0.3|\Delta H^o_{cryst}|}{\Omega^{2/3}}$, it's around 18mJ/m^2. The K_{lb} = 17μM^{-1} and K_{lp} = 0.0016μM^{-1} were determined by simultaneously solving for $\Delta\gamma$ and V_R. Figure 61 shows a good fit of the step velocity predicted by C-V with the step velocities measured at constant impurity and varying impurities.

6.5 Reversibility of Protoporphyrin IX Inhibition

The effect of protoporphyrin IX was found to be reversible as shown in figure 62 and the step velocities completely regenerated as shown in figure 63. The step velocities regenerated on removal of protoporphyrin IX.

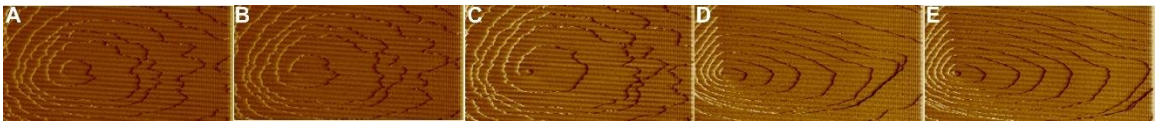

Figure 63: Regeneration of steps on (010) face of etioporphyrin I after removal of protoporphyrin IX. Panel (A-C) growth in presence of PPIX and panel (D, E) growth after removal of protoporphyrin IX.

To understand if the effect of protoporphyrin IX is reversible or irreversible we performed pulse studies where growth ($C_{EtP\,I} = 0.35mM$) and impure solution ($C_{EtP\,I} = 0.35mM, C_{PPIX} = 2\mu M$) were alternatively pushed on the (010) face of etioporphyrin I (figure 62). The removal of protoporphyrin IX from the growth solution changes the step

anisotropy to the original form. The step velocities eventually reach the pure solution velocity. This is due to the removal of adsorbed protoporphyrin IX from the terraces and kinks.

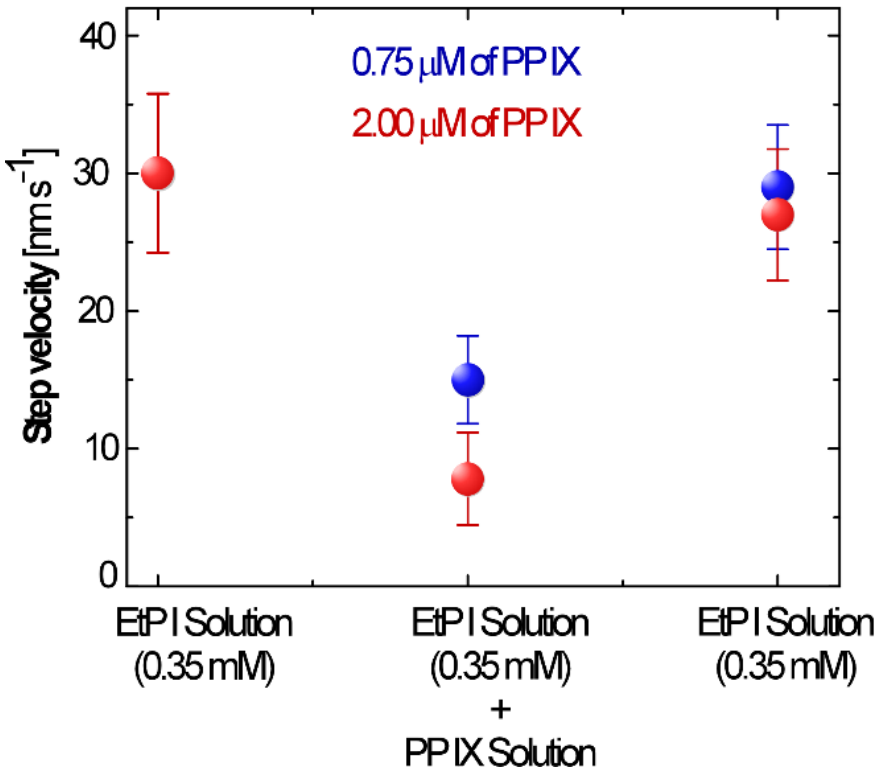

Figure 64: Regeneration of step velocity on the (010) face of etioporphyrin I. The step velocities on the (010) face of etioporphyrin I in presence of C_{etpI} =0.35mM and C_{etpI} =0.35mM and C_{PPIX} =1.5μM.

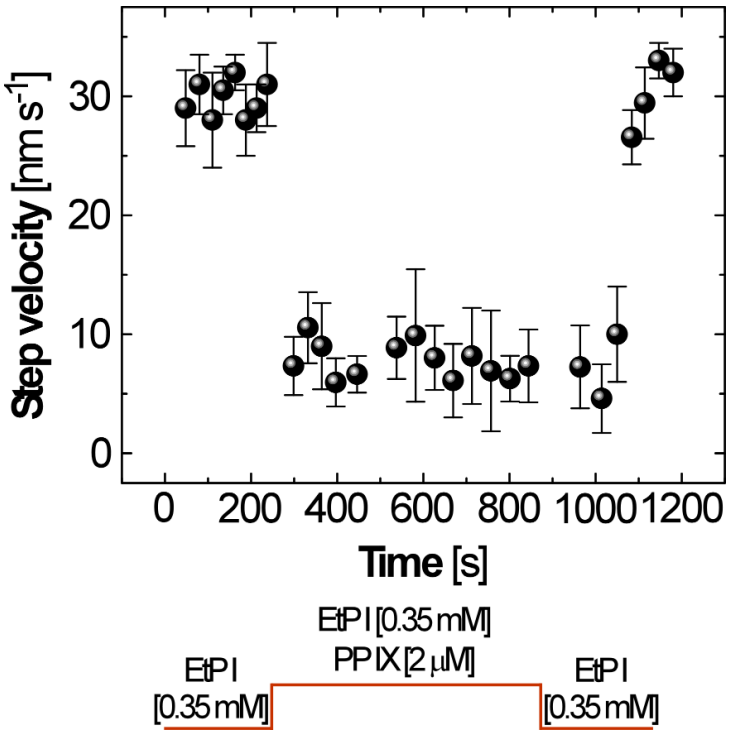

Figure 65: The transient time need to reach the pure step velocity of (010) face after removal of impurities.

On removal of impurity from the growth solution the step velocities revert to the original pure solution step velocity shown in figure 63. The transient time needed to reach pure solution velocity is shown in figure 64. The removal of adsorbed impurities leads to the regeneration of steps and step velocities.

6.6 Inference

Presence of impurities are an integral part of industrial and natural crystallization processes. Understanding the molecular mechanism of inhibition is essential to design robust crystallization processes and crystal growth modifiers. We have demonstrated that protoporphyrin IX exhibits inhibition of etioporphyrin I crystal growth by both kink blocking and step pinning. The suppression by protoporphyrin IX is based on its specific interactions with crystal terraces, step edges and kinks. We show that drug–crystal interactions are a significantly more efficient pathway to inhibition of etioporphyrin I

crystallization than sequestration of soluble etioporphyrin I into impurity– etioporphyrin complexes. Finally, we show the compliance of the Cabrera- Vermilya Model in predicting the step kinetics of etioporphyrin I in presence of protoporphyrin IX, which acts as both step pinner and kink blocker.

Chapter 7: Future Work

Some of the interesting paradigms of organic crystallization were understood from this work. We deduced the importance of solute-solvent interactions from solution thermodynamics of etioporphyrin I from a line to five organic solvents, highlighting the importance of a variety of solute-solvent interactions like permanent dipoles and London dispersion forces. The thermodynamic parameters of crystallization were determined from the solubility measurements. Thus, highlighting the importance of solvent medium for crystallization processes. Understanding of solute-solvent interactions help in the prediction of solubility in organic solvents. In organic solvents the weak solvent-solvent bonds contribute negligibly to the solution thermodynamics and solvent structuring, at the crystal interface being negligible, it plays an important role in determining solute incorporation mode into the growth sites or kinks. A further prospect of this understanding is to develop in-silico models of solubility prediction for different solutes in a variety of organic solvents, thus providing robust method development technologies for crystallization.

Anisotropic growth in different crystal facets of etioporphyrin I proves the long road to go for complete understanding of crystallization fundamentals. The grooved and flat faces of etioporphyrin I show distinct growth modes. Finally using solvents of different viscosities, we show that the rate constants scales with solvent viscosity for homologous series of solvents and we show the presence of an intermediate state stabilized by solvent. The further step of this work will be determining the step kinetic rates in presence of different small molecule as solvents. Thus, we can form an idea on how the solute-solvent

interactions affect the kinetics of crystallization and develop in-silico models for crystal growth rate of different small molecules from a variety of solvents.

Finally, impurities or crystal growth modifiers are an important area of research for understanding real world scenarios of crystallization. The control of nucleation and growth plays an important role in controlling crystallization. It would be interesting to design classical and non-classical modes of crystallization inhibition to suppress, fine-tune and design crystal growth processes. Control of crystal nucleation is among the grandest fundamental challenges facing modern materials science[179]. Insight on how organic molecules form assemblies that host nucleation and enhance crystal growth[77] is severely lacking; this lack stands in contrast to the advanced understanding of the mechanisms leading to the formation of nucleation precursors of protein crystals and other solid aggregates[180]. A fundamental mechanism of formation and stability of the nucleation precursors and their response to modifiers should be established. We will test whether suppression of precursors correlates with inhibition of nucleation.

To define molecular and mesoscopic mechanisms that leads to irreversible or reversible inhibition of crystal growth experiments should be performed on crystallites, whose nucleation is promoted by additives, land on the crystal surface out of registry with the underlying lattice[160]. Crystallization in presence of additives should be studied which boosts step bunching, destabilize the crystal surface dynamics, and engender numerous dislocations. Both outcomes strain the top crystal layers. If the strain persists after remove of the triggering additive from the solution it will prevent crystal growth to resume. It is important to extend the insight on the mechanism of crystallization precursors to formulate selection criteria for modifiers. It is also important to establish whether a threshold modifier

concentration for irreversible inhibition exists. *In-silico* studies on the interaction of modifiers with step patterns to identify step bunch stabilizers that may act as irreversible inhibitors and test the model predictions experimentally.

In real-world scenarios crystallization takes place in presence of multiple additives, formation of biomimetic, pathological, natural, and industrial crystals with variety of forms and functionality occurs in the presence of several impurities. Multiple modifiers act in tandem to vary the crystal habit, growth, and nucleation. To control crystallization, it is important to elucidate the molecular mechanisms of synergistic, additive, and antagonistic cooperativity between pairs or multiple crystal growth inhibitors. Recent work on modifiers suggests that the cooperativity between step pinners and kink blockers transitions from synergistic at low inhibitor concentrations to antagonistic at moderate and high inhibitor amounts[181]. It will be interesting to study the cooperativity between two step pinners or two kink blockers guided by the hypothesis that their activities will not be additive as long as their adsorptions on terraces and kinks, respectively, are not matched. To explore the crystal nucleation precursors, we can monitor etioporphyrin I solutions with concentrations below the crystal solubility, in which crystallization is prohibited, with oblique illumination microscopy (OIM). In OIM a green laser illuminates a thin (500 nm) solution layer at an oblique angle such that the incident beam avoids a microscope lens positioned above the sample. Solution inhomogeneities are detected from the light that they scatter toward the objective lens.

It will be interesting to study organic compound that form crystals of direct technological application: pharmaceuticals, such as mefenamic acid, a nonsteroidal anti-inflammatory drug,[182] and functional materials, such as etioporphyrin I, whose crystals find potential

applications as field-effect transistors.[8,96,97] To explore the consequences of solute-solvent interactions on clusters, it will be interesting to employ organic solvents that exhibit distinct interactions with the solutes and enforce divergent solubilities: alkyl alcohols, from ethanol to octanol, dimethyl sulfoxide (DMSO), acetonitrile, polar aprotic solvents with short aliphatic residues, and caprylic (octanoic) acid.

Analyze cooperative inhibition in bulk crystallization experiments. Owing to the crystal anisotropy, inhibitor molecules that bind to crystal surfaces exhibit marked differences in inhibition of growth in different crystallographic directions.[50,141,183] It will be interesting to assess the anisotropic growth rates by bulk crystallization studies to determine the macroscopic dimensions of crystals grown for 10-20 days at varying concentrations of the modifiers. To quantify the modifier effect on the growth of the anisotropic faces in the presence and absence of modifiers it should be done by measuring the length and width of the grown crystals from SEM micrographs.

References

1 Addadi, L. & Weiner, S. A pavement of pearl. *Nature* **389**, 912-913, doi:10.1038/40010 (1997).

2 Teng, H. H., Dove, P. M., Orme, C. A. & De Yoreo, J. J. Thermodynamics of Calcite Growth: Baseline for Understanding Biomineral Formation. *Science* **282**, 724, doi:10.1126/science.282.5389.724 (1998).

3 Chung, J., Granja, I., Taylor, M.G., Mpourmpakis, G., Asplin, J.R. & Rimer, J.D. Molecular modifiers reveal a mechanism of pathological crystal growth inhibition. *Nature* **536**, 446-450, doi:10.1038/nature19062 (2016).

4 Busch, N., Matiuck, N., Sahlin, S., Pillay, S. P. & Holzbach, R. T. Inhibition and promotion of cholesterol crystallization by protein fractions from normal human gallbladder bile. *Journal of Lipid Research* **32**, 695-702, doi:10.1016/s0022-2275(20)42057-7 (1991).

5 Song, X., Yang, X., Zhang, T., Zhang, H., Zhang, Q., Hu, D., Chang, X., Li, Y., Chen, Z., Jia, M., Zhang, P. &Yu, J. Controlling the Morphology and Titanium Coordination States of TS-1 Zeolites by Crystal Growth Modifier. *Inorganic Chemistry* **59**, 13201-13210, doi:10.1021/acs.inorgchem.0c01518 (2020).

6 Sanhoob, M. A., Muraza, O., Al-Mutairi, E. M. & Ullah, N. Role of crystal growth modifiers in the synthesis of ZSM-12 zeolite. *Advanced Powder Technology* **26**, 188-192, doi:https://doi.org/10.1016/j.apt.2014.09.007 (2015).

7 Liu, X., Yang, Z., Wang, D. & Cao, H. Molecular Structures and Second-Order Nonlinear Optical Properties of Ionic Organic Crystal Materials. *Crystals* **6**, doi:10.3390/cryst6120158 (2016).

8 Che, C.-M., Xiang, H-F., Chui, S. S-Y., Xu, Z-X., Roy, V.A.L., Yan, J.J., Fu, W-F., Lai, P. T. & Williams, I. D. A High-Performance Organic Field-Effect Transistor Based on Platinum(II) Porphyrin: Peripheral Substituents on Porphyrin Ligand Significantly Affect Film Structure and Charge Mobility. *Chemistry – An Asian Journal* **3**, 1092-1103, doi:10.1002/asia.200800011 (2008).

9 F. Doherty, M. in *Computer Aided Chemical Engineering* Vol. 24 (eds Valentin Pleşu & Paul Şerban Agachi) 9-10 (Elsevier, 2007).

10 Datta, S. & Grant, D. J. W. Crystal structures of drugs: advances in determination, prediction and engineering. *Nature Reviews Drug Discovery* **3**, 42-57, doi:10.1038/nrd1280 (2004).

11 Ramakrishnan, S. Yarranguntla, S. R., Peddireddy, S. R., Kanniah, S. L., Mudapaka, V.K. & Shekhawat, L.K. Development of Pharmaceutically Acceptable Crystalline Forms of Drug Substances via Solid-State Solvent Exchange. *Organic Process Research & Development* **21**, 1478-1487, doi:10.1021/acs.oprd.7b00114 (2017).

12 Chadha, R., Gupta, S. & Shukla, G. Crystal habit, characterization and pharmacological activity of various crystal forms of arteether. *Acta Pharmaceutica Sinica B* **1**, 129-135, doi:https://doi.org/10.1016/j.apsb.2011.06.010 (2011).

13 Hadjittofis, E., Isbell, M.A., Karde, V., Varghese, S., Ghoroi, C. & Heng, J.Y.Y. Influences of Crystal Anisotropy in Pharmaceutical Process Development. *Pharmaceutical Research* **35**, 100, doi:10.1007/s11095-018-2374-9 (2018).

14 Bernstein, J. & MacAlpine, J. Pharmaceutical Crystal Forms and Crystal-Form Patents: Novelty and Obviousness1. *Polymorphism in the Pharmaceutical Industry*, 469-483, doi:https://doi.org/10.1002/9783527697847.ch16 (2018).

15 Warzecha, M., Verma, Lakshmanji., Johnston, B.F., Palmer, J.C., Florence, A.J. & Vekilov, P.G. Olanzapine crystal symmetry originates in preformed centrosymmetric solute dimers. *Nature Chemistry* **12**, 914-920, doi:10.1038/s41557-020-0542-0 (2020).

16 Mohan, R. & Myerson, A. S. Growth kinetics: a thermodynamic approach. *Chemical Engineering Science* **57**, 4277-4285, doi:https://doi.org/10.1016/S0009-2509(02)00344-5 (2002).

17 *Frontiers in Crystalline Matter:From Discovery to Technology*. (The National Academies Press, 2009).

18 De Yoreo, J. J., Burnham, A. K. & Whitman, P. K. Developing KH_2PO_4 and KD_2PO_4 crystals for the world's most power laser. *International Materials Reviews* **47**, 113 -- 152 (2002).

19 Myerson, A. S. *Handbook of Industrial Crystallization*. (Butterworth-Heinemann, 2002).

20 Brange, J. *Galenics of Insulin*. (Springer, 1987).

21 Long, M. L., Bishop, J.B. & DeLucas.L.J. Protein crystal growth in microgravity review of large scale temperature induction method. *J. Crystal Growth* **168**, 233-243 (1996).

22 Matsuda, S. Senda, T., Itoh, S., Kawano, G., Mizuno, H. & Mitsui, Y. New crystal form of recombinant murine interferon-b. *J. Biol. Chem* **264**, 13381-13382 (1989).

23 Peseta, S., Langer, J. A., Zoon, K. C. & Samuel, C. E. in *Annual Review of Biochemistry* Vol. 56 (eds C.C. Richardson, P.D. Boyer, I.B. Dawid, & A. Meister) 727-778 (Annual Reviews, 1989).

24 Reichert, P. Mcnemar, C., Nagabhushan, N., Nagabhusan, T.L. Tindall, S. & Hruza, A.. Metal-interferon-alpha crystals. US Patent patent 5,441,734. (1995).

25 De Yoreo, J. J. & Vekilov, P. G. Principles of Crystal Nucleation and Growth. *Reviews in Mineralogy and Geochemistry* **54**, 57-93, doi:10.2113/0540057 (2003).

26 Lin, H., Rosenberger, F., Alexander, J. I. D. & Nadarajah, A. Convective-diffusive transport in protein crystal growth. *J. Crystal Growth* **151**, 153-162 (1995).

27 Yeckel, A. & Derby, J. J. *Computer Modelling of Bulk Crystal Growth*. (John Wiley & Sons Ltd, 2005).

28 Vartak, B., Yeckel, A. & Derby, J. J. Time-dependent, three-dimensional flow and mass transport during solution growth of potassium titanyl phosphate. *J. Cryst. Growth* **281**, 391-406, doi:10.1016/j.jcrysgro.2005.04.037 (2005).

29 Derby, J. J., Chelikowsky, J. R., Sinni, T., Bai, B., Jwon, Y., Lun, L., Panday, A. & Yeckel, A. in *Perspectives on Inorganic, Organic, and Biological Crystal Growth: From Fundamentals to Applications* Vol. 916 *AIP Conference Proceedings* (eds M. Skowronski, J. J. DeYoreo, & C. A. Wang) 139-158 (Amer Inst Physics, 2007).

30 Lin, H., Petsev, D. N., Yau, S.-T., Thomas, B. R. & Vekilov, P. G. Lower Incorporation of Impurities in Ferritin Crystals by Suppression of Convection: Modeling Results. *Crystal Growth and Design* **1**, 73-79 (2001).

31 Yeckel, A. & Derby, J. J. Dynamics of three-dimensional convection in microgravity crystal growth: g-jitter with steady magnetic fields. *J. Cryst. Growth* **263**, 40-52, doi:10.1016/j.jcrysgro.2003.11.047 (2004).

32 Kwon, Y. I. & Derby, J. J. Modeling the coupled effects of interfacial and bulk phenomena during solution crystal growth. *J. Cryst. Growth* **230**, 328-335, doi:10.1016/s0022-0248(01)01345-8 (2001).

33 Lin, H., Vekilov, P. G. & Rosenberger, F. Facet morphology response to non-uniformities in nutrient and impurity supply. II. Numerical modeling. *J. Crystal Growth* **158**, 552-559 (1996).

34 Vekilov, P. G., Lin, H. & Rosenberger, F. Unsteady crystal growth due to step-bunch cascading. *Phys. Rev. E* **55**, 3202-3214 (1997).

35 Chernov, A. A. The spiral growth of crystals. *Sov. Phys. Uspekhi* **4**, 116-148 (1961).

36 Chernov, A. A. *Modern Crystallography III, Crystal Growth,*. (Springer, 1984).

37 Petsev, D. N., Chen, K., Gliko, O. & Vekilov, P. G. Diffusion-limited kinetics of the solution-solid phase transition of molecular substances. *Proc. Natl. Acad. Sci. USA* **100**, 792-796 (2003).

38 De Yoreo, J. J. & Vekilov, P. G. in *Biomineralization* Vol. 54 *Reviews in Mineralogy & Geochemistry* 57-93 (2003).

39 Vekilov, P. G. in *Perspectives on Inorganic, Organic and Biological Crystal Growth: From Fundamentals to Applications: AIP Conference Proceedings* Vol. 916 *AIP Conference Series* (eds M. Skowronski, J. J. DeYoreo, & C.A. Wang) 235-267 (AIP, 2007).

40 Vekilov, P. G. Phase transitions of folded proteins. *Soft Matter* **6**, 5254-5272 (2010).

41 Sleutel, M., Driessche, A. E. S.V., Pan, W., Reichel, E.K., Maes, D., Vekilov, P.G. Does Solution Viscosity Scale the Rate of Aggregation of Folded Proteins? *The Journal of Physical Chemistry Letters*, 1258-1263, doi:10.1021/jz300459n (2012).

42 Miyata, K., Tracey, J., Miyazawa, K., Haapasilta, V., Spijker, P., Kawagoe, Y., Foster, A.S., Tsukamoto, K. & Fukuma, T. Dissolution Processes at Step Edges of Calcite in Water Investigated by High-Speed Frequency Modulation Atomic Force Microscopy and Simulation. *Nano Letters* **17**, 4083-4089, doi:10.1021/acs.nanolett.7b00757 (2017).

43 Tsarfati, Y., Rosenne, S., Weissman, H., Shimon, L.J.W., Gur, D., Palmer B.A. & Rybtchinski, B. Crystallization of Organic Molecules: Nonclassical Mechanism Revealed by Direct Imaging. *ACS Central Science* **4**, 1031-1036, doi:10.1021/acscentsci.8b00289 (2018).

44 Fukuma, T. Water distribution at solid/liquid interfaces visualized by frequency modulation atomic force microscopy. *Science and Technology of Advanced Materials* **11**, 033003, doi:10.1088/1468-6996/11/3/033003 (2010).

45 Ball, P. Chemical physics: How to keep dry in water. *Nature* **423**, 25 - 26 (2003).

46 Ball, P. Water as an Active Constituent in Cell Biology. *Chem. Rev.* **108**, 74-108 (2008).

47 Vekilov, P. G. What determines the rate of growth of crystals from solution? . *Crystal Growth and Design*, **7**, 2796-2810 (2007).

48 Vekilov, P. G. What Is the Molecular-Level Role of the Solution Components in Protein Crystallization? *Cryst. Growth Des.* **7**, 2239-2246 (2007).

49 De Yoreo, J. J., Gilbert, P.U.P.A., Sommerdijk, N.A.J.M., Penn, R.L., Whitelam, S. Joester, D., Zhang, H., Rimer, J.D., Navrotsky, A., Banfield, J.F., Wallace, A.F., Michel, F.M., Meldrum, F.C., Cölfen,H. & Patricia M. Dove, P.M. Crystallization by particle attachment in synthetic, biogenic, and geologic environments. *Science* **349**, aaa6760, doi:10.1126/science.aaa6760 (2015).

50 Olafson, K. N., Li, R., Alamani, B. G. & Rimer, J. D. Engineering Crystal Modifiers: Bridging Classical and Nonclassical Crystallization. *Chemistry of Materials* **28**, 8453-8465, doi:10.1021/acs.chemmater.6b03550 (2016).

51 Vekilov, P. G. What Determines the Rate of Growth of Crystals from Solution? *Crystal Growth & Design* **7**, 2796-2810, doi:10.1021/cg070427i (2007).

52 Olafson, K. N., Ketchum, M. A., Rimer, J. D. & Vekilov, P. G. Molecular Mechanisms of Hematin Crystallization from Organic Solvent. *Crystal Growth & Design* **15**, 5535-5542, doi:10.1021/acs.cgd.5b01157 (2015).

53 Vekilov, P. G., Kuznetsov, Y. G. & Chernov, A. A. Interstep interaction in solution growth; (101) ADP face. *Journal of Crystal Growth* **121**, 643-655, doi:https://doi.org/10.1016/0022-0248(92)90571-Y (1992).

54 Fukuma, T., Higgins, M. J. & Jarvis, S. P. Direct Imaging of Individual Intrinsic Hydration Layers on Lipid Bilayers at Ångstrom Resolution. *Biophysical Journal* **92**, 3603-3609, doi:https://doi.org/10.1529/biophysj.106.100651 (2007).

55 Sazaki, G., Zepeda, S., Nakatsubo, S., Yokoyama, E. & Furukawa, Y. Elementary steps at the surface of ice crystals visualized by advanced optical microscopy.

Proceedings of the National Academy of Sciences **107**, 19702, doi:10.1073/pnas.1008866107 (2010).

56 Rimer, J. D., An. Z., Zhu, Z., Lee, M.H., Goldfarb, D.S., Wesson, J.A. & Ward, M.D. Crystal Growth Inhibitors for the Prevention of L-Cystine Kidney Stones Through Molecular Design. *Science* **330**, 337, doi:10.1126/science.1191968 (2010).

57 Teng, H. H., Dove, P. M. & De Yoreo, J. J. Kinetics of calcite growth: surface processes and relationships to macroscopic rate laws. *Geochimica et Cosmochimica Acta* **64**, 2255-2266, doi:https://doi.org/10.1016/S0016-7037(00)00341-0 (2000).

58 Reviakine, I., Georgiou, D. K. & Vekilov, P. G. Capillarity Effects on Crystallization Kinetics: Insulin. *Journal of the American Chemical Society* **125**, 11684-11693, doi:10.1021/ja030194t (2003).

59 Lupulescu, A. I. & Rimer, J. D. In Situ Imaging of Silicalite-1 Surface Growth Reveals the Mechanism of Crystallization. *Science* **344**, 729, doi:10.1126/science.1250984 (2014).

60 Kumar, M., Luo, H., Román-Leshkov, Y. & Rimer, J. D. SSZ-13 Crystallization by Particle Attachment and Deterministic Pathways to Crystal Size Control. *Journal of the American Chemical Society* **137**, 13007-13017, doi:10.1021/jacs.5b07477 (2015).

61 Myerson, A. S. *Handbook of Industrial Crystallization: Third Edition*. (Cambrifge University Press, 2019).

62 Sato, S., Gondo, D., Wada, T., Kanehashi, S. & Nagai, K. Effects of various liquid organic solvents on solvent-induced crystallization of amorphous poly(lactic acid)

film. *Journal of Applied Polymer Science* **129**, 1607-1617, doi:10.1002/app.38833 (2013).

63 Paul, E. L., Tung, H.-H. & Midler, M. Organic crystallization processes. *Powder Technology* **150**, 133-143, doi:http://dx.doi.org/10.1016/j.powtec.2004.11.040 (2005).

64 Marinova, V., Wood, G. P. F., Marziano, I. & Salvalaglio, M. Dynamics and Thermodynamics of Ibuprofen Conformational Isomerism at the Crystal/Solution Interface. *Journal of Chemical Theory and Computation* **14**, 6484-6494, doi:10.1021/acs.jctc.8b00702 (2018).

65 Marinova, V., Wood, G. P. F., Marziano, I. & Salvalaglio, M. Solvent Dynamics and Thermodynamics at the Crystal–Solution Interface of Ibuprofen. *Crystal Growth & Design* **19**, 6534-6541, doi:10.1021/acs.cgd.9b00983 (2019).

66 Khamar, D., Zeglinski, J., Mealey, D. & Rasmuson, Å. C. Investigating the Role of Solvent–Solute Interaction in Crystal Nucleation of Salicylic Acid from Organic Solvents. *Journal of the American Chemical Society* **136**, 11664-11673, doi:10.1021/ja503131w (2014).

67 Lovette, M. A. & Doherty, M. F. Needle-Shaped Crystals: Causality and Solvent Selection Guidance Based on Periodic Bond Chains. *Crystal Growth & Design* **13**, 3341-3352, doi:10.1021/cg301830u (2013).

68 Spijker, P., Hiasa, T., Musso, T., Nishioka, R., Onishi, H. & Foster, A.S.. Understanding the Interface of Liquids with an Organic Crystal Surface from Atomistic Simulations and AFM Experiments. *The Journal of Physical Chemistry C* **118**, 2058-2066, doi:10.1021/jp4106647 (2014).

69 Gnanasambandam, S. & Rajagopalan, R. Growth morphology of α-glycine crystals in solution environments: an extended interface structure analysis. *CrystEngComm* **12**, 1740-1749, doi:10.1039/b922780f (2010).

70 Marin, F. & Luquet, G. Molluscan biomineralization: The proteinaceous shell constituents of Pinna nobilis L. *Materials Science and Engineering: C* **25**, 105-111, doi:https://doi.org/10.1016/j.msec.2005.01.003 (2005).

71 Porter, S. M. Seawater Chemistry and Early Carbonate Biomineralization. *Science* **316**, 1302-1302, doi:10.1126/science.1137284 (2007).

72 Reznikov, N., Steele, J. A. M., Fratzl, P. & Stevens, M. M. A materials science vision of extracellular matrix mineralization. *Nature Reviews Materials* **1**, 16041, doi:10.1038/natrevmats.2016.41 (2016).

73 Duewell, P., Kono, H., Rayner, K.J., Sirois, C.M., Vladimer, G., Bauerfeind, F.G., Abela, G.S., Franchi, L., Nuńez, G., Schnurr, M., Espevik, T., Lien, E., Fitzgerald, K.A., Rock, K.L., Moore, K.J., Wright, S.D., Hornung, V. & Latz, E. NLRP3 inflammasomes are required for atherogenesis and activated by cholesterol crystals. *Nature* **464**, 1357-1361, doi:10.1038/nature08938 (2010).

74 Blagden, N. & Davey, R. J. Polymorph Selection: Challenges for the Future? *Crystal Growth & Design* **3**, 873-885, doi:10.1021/cg030025k (2003).

75 Bonnett, P. E., Carpenter, K. J., Dawson, S. & Davey, R. J. Solution crystallization via a submerged liquid-liquid phase boundary: oiling out. *Chem. Commun.*, 698-699 (2003).

76 Chakrabarti, R. G. & Vekilov, P. G. Attraction between Permanent Dipoles and London Dispersion Forces Dominate the Thermodynamics of Organic

Crystallization. *Crystal Growth & Design* **20**, 7429-7438, doi:10.1021/acs.cgd.0c01102 (2020).

77 Hu, Y., Liang, J. K., Myerson, A. S. & Taylor, L. S. Crystallization Monitoring by Raman Spectroscopy: Simultaneous Measurement of Desupersaturation Profile and Polymorphic Form in Flufenamic Acid Systems. *Industrial & Engineering Chemistry Research* **44**, 1233-1240, doi:10.1021/ie049745u (2005).

78 Hashimoto, T., Choe, Y.-K., Nakano, H. & Hirao, K. Theoretical Study of the Q and B Bands of Free-Base, Magnesium, and Zinc Porphyrins, and Their Derivatives. *The Journal of Physical Chemistry A* **103**, 1894-1904, doi:10.1021/jp984807d (1999).

79 Borah, K. D. & Bhuyan, J. Magnesium porphyrins with relevance to chlorophylls. *Dalton Transactions* **46**, 6497-6509, doi:10.1039/c7dt00823f (2017).

80 Santos, E. H., Carvalho, C., Terzi, C. M. & Nakagaki, S. Recent Advances in Catalyzed Sequential Reactions and the Potential Use of Tetrapyrrolic Macrocycles as Catalysts. *Molecules* **23**, 2796, doi:10.3390/molecules23112796 (2018).

81 de Araujo Tôrres, M. G., da Silva, V. S., Idemori, Y. M. & DeFreitas-Silva, G. Manganese porphyrins as efficient catalysts in solvent-free cyclohexane oxidation. *Arabian Journal of Chemistry* **13**, 1563-1574, doi:https://doi.org/10.1016/j.arabjc.2017.12.007 (2020).

82 Kou, J., Dou, D. & Yang, L. Porphyrin photosensitizers in photodynamic therapy and its applications. *Oncotarget* **8**, 81591-81603, doi:10.18632/oncotarget.20189 (2017).

83 Jurow, M., Schuckman, A. E., Batteas, J. D. & Drain, C. M. Porphyrins as Molecular Electronic Components of Functional Devices. *Coord Chem Rev* **254**, 2297-2310, doi:10.1016/j.ccr.2010.05.014 (2010).

84 Giovannetti, R. (2012).

85 Harriman, A. & Sauvage, J.-P. A strategy for constructing photosynthetic models: porphyrin-containing modules assembled around transition metals. *Chemical Society Reviews* **25**, 41-48, doi:10.1039/cs9962500041 (1996).

86 Gouterman, M., Mathies, R. A., Smith, B. E. & Caughey, W. S. *J. Chem. Phys.* **52** (1970).

87 Eastwood, D. & Gouterman, M. *J. Mol. Spectr.* **30** (1969).

88 Ake, R. L. & Gouterman, M. *Theor. Chim. Acta* **15** (1969).

89 Fulton, R. L. & Gouterman, M. Vibronic Coupling. I. Mathematical Treatment for Two Electronic States. *The Journal of Chemical Physics* **35**, 1059-1071, doi:10.1063/1.1701181 (1961).

90 Gouterman, M. & Stevenson, P. E. Porphyrin Charge-Transfer Complexes with Sym-Trinitrobenzene. *The Journal of Chemical Physics* **37**, 2266-2269, doi:10.1063/1.1732997 (1962).

91 Gouterman, M. Study of the Effects of Substitution on the Absorption Spectra of Porphin. *The Journal of Chemical Physics* **30**, 1139-1161, doi:10.1063/1.1730148 (1959).

92 Prins, L. J., Reinhoudt, D. N. & Timmerman, P. Noncovalent Synthesis Using Hydrogen Bonding. *Angewandte Chemie International Edition* **40**, 2382-2426,

doi:https://doi.org/10.1002/1521-3773(20010702)40:13<2382::AID-ANIE2382>3.0.CO;2-G (2001).

93 Liang, Z., Chen, J-F., Ma, Y., Wang, W., Han, X., Xue, C. & Zhao, H. Qualitative rationalization of the crystal growth morphology of benzoic acid controlled using solvents. *CrystEngComm* **16**, 5997-6002, doi:10.1039/c4ce00776j (2014).

94 Olafson, K. N., Clark, R. J., Vekilov, P. G., Palmer, J. C. & Rimer, J. D. Structuring of Organic Solvents at Solid Interfaces and Ramifications for Antimalarial Adsorption on β-Hematin Crystals. *ACS Applied Materials & Interfaces* **10**, 29288-29298, doi:10.1021/acsami.8b08579 (2018).

95 Harris, K. D. M., Hughes, C. E., Palmer, B. A. & Guillaume, F. New Strategies for Exploring Crystallization Processes of Organic Materials. *Transactions of the American Crystallographic Association* **43**, 97 - 112 (2012).

96 Hoang, M. H., Kim, M., Kim, K.H., Lee, T.W., Nguyen, D.N., Kim, J., Lee, K., Lee, S.J. & Choi, D.H. Unusually High-Performing Organic Field-Effect Transistors Based on π-Extended Semiconducting Porphyrins. *Advanced Materials* **24**, 5363-5367, doi:10.1002/adma.201202148 (2012).

97 Hoang, M. H., Kim, Y., Kim, S.-J., Choi, D. H. & Lee, S. J. High-Performance Single-Crystal-Based Organic Field-Effect Transistors from π-Extended Porphyrin Derivatives. *Chemistry – A European Journal* **17**, 7772-7776, doi:10.1002/chem.201100599 (2011).

98 Schneider, H.-J. Dispersive Interactions in Solution Complexes. *Accounts Chem. Res.* **48**, 1815-1822, doi:10.1021/acs.accounts.5b00111 (2015).

99 Stranski, I. N. Zur Theorie des Kristallwachstums. *Z. Phys. Chem.* **136**, 259-278 (1928).

100 Yau, S.-T., Thomas, B. R. & Vekilov, P. G. Molecular mechanisms of crystallization and defect formation. *Phys. Rev. Lett.* **85**, 353-356 (2000).

101 Warzecha, M., Safari, M. S., Florence, A. J. & Vekilov, P. G. Mesoscopic Solute-Rich Clusters in Olanzapine Solutions. *Crystal Growth & Design* **17**, 6668-6676, doi:10.1021/acs.cgd.7b01299 (2017).

102 Sleutel, M. Willaert, R., Gillespie, C., Evrard, C., Wyns, L. & Maes, D. Kinetics and Thermodynamics of Glucose Isomerase Crystallization. *Crystal Growth & Design* **9**, 497-504, doi:10.1021/cg800756h (2009).

103 Schall, C., Arnold, E. & Wiencek, J. M. Enthalpy of Crystallization of Hen Egg White Lysozyme. *J. Crystal Growth* **165** (1996).

104 Shtukenberg, A. G., Ward, M. D. & Kahr, B. Crystal growth with macromolecular additives. *Chemical reviews* **117**, 14042-14090 (2017).

105 Weaver, M. L., Qiu, S.R., Hoyer, J.R., Casey, W.H., Nancollas, G.H. & Yoreo, J.J. Improved model for inhibition of pathological mineralization based on citrate–calcium oxalate monohydrate interaction. *ChemPhysChem* **7**, 2081-2084 (2006).

106 De Yoreo, J. J., Zepeda-Ruiz, L.A., Friddle, R.W., Qiu, S.R., Wasylenki, L.E., Chernov, A.A., Gilmer, G.H. & Dove, P.M. Rethinking Classical Crystal Growth Models through Molecular Scale Insights: Consequences of Kink-Limited Kinetics. *Crystal Growth & Design* **9**, 5135-5144, doi:10.1021/cg900543g (2009).

107 Bostanov, V., Staikov, G. & Roe, D. K. Rate of propagation of growth layers on cubic crystal faces in electrocrystallization of silver. *J. Electrochem. Soc.* **122**, 1301-1305 (1975).

108 Vekilov, P. G., Kuznetsov, Y. G. & Chernov, A. A. Dissolution morphology and kinetics of (101) ADP face; mild etching of surface defects. *J. Crystal Growth* **102**, 706-716 (1990).

109 Fersht, A. *Structure and mechanism in protein science*. (W.H. Freeman, 1999).

110 Finkelstein, A. & Janin, J. The price of lost freedom: entropy of bimolecular complex formation. *Protein Engineering* **3**, 1-10 (1989).

111 Choudhury, N. & Pettitt, B. M. On the Mechanism of Hydrophobic Association of Nanoscopic Solutes. *J. Am. Chem. Soc.* **127**, 3556-3567 (2005).

112 Vekilov, P. G., Galkin, O., Pettitt, B. M., Choudhury, N. & Nagel, R. L. Determination of the transition-state entropy for aggregation suggests how the growth of sickle cell hemoglobin polymers can be slowed. *J Mol Biol* **377**, 882-888, doi:S0022-2836(08)00047-8 [pii] 10.1016/j.jmb.2008.01.025 (2008).

113 Dvornikov, S. S., Solov'ev, K. N. & Tsvirko, M. P. Spectroscopic manifestations of dimerization of etioporphyrin I in hydrocarbon solvents. *Journal of Applied Spectroscopy* **38**, 581-585, doi:10.1007/BF00658793 (1983).

114 *Handbook of Chemistry and Physics, 81-th Edition*. (CRC Press, 2000-2001).

115 James Speight, P. D. *Lange's Handbook of Chemistry, Sixteenth Edition*. 16th ed. / edn, (McGraw-Hill Education, 2005).

116 Marino, G. The direction of the dipole moments of furan, thiophen, and pyrrole: A controversial question. *Journal of Heterocyclic Chemistry* **9**, 817-819, doi:10.1002/jhet.5570090409 (1972).

117 Goldberg, P. K., Pundsack, T. J. & Splan, K. E. Photophysical Investigation of Neutral and Diprotonated Free-Base Bis(Arylethynyl)porphyrins. *The Journal of Physical Chemistry A* **115**, 10452-10460, doi:10.1021/jp205309f (2011).

118 Bruhn, T. & Brückner, C. The origin of the absorption spectra of porphyrin N- and dithiaporphyrin S-oxides in their neutral and protonated states. *Physical Chemistry Chemical Physics* **17**, 3560-3569, doi:10.1039/C4CP04675G (2015).

119 Marini, A., Muñoz-Losa, A., Biancardi, A. & Mennucci, B. What is Solvatochromism? *The Journal of Physical Chemistry B* **114**, 17128-17135, doi:10.1021/jp1097487 (2010).

120 Moldoveanu, S. C. & David, V. in *Essentials in Modern HPLC Separations* (eds Serban C. Moldoveanu & Victor David) 115-143 (Elsevier, 2013).

121 Mognaschi, E. R., Laboranti, L. M. & Chierico, A. Associating behaviour of pure polar liquids : dielectric properties of caprylic acid. *J. Phys. II France* **3**, 1271-1277 (1993).

122 Kim, H., Keller, R. & Gwinn, W. D. Dipole Moment of Formic Acid, HCOOH and HCOOD. *The Journal of Chemical Physics* **37**, 2748-2750, doi:10.1063/1.1733099 (1962).

123 Paoli, M., Marles-Wright, J. & Smith, A. Structure–Function Relationships in Heme-Proteins. *DNA and Cell Biology* **21**, 271-280, doi:10.1089/104454902753759690 (2002).

124 Mohsen-Nia, M., Amiri, H. & Jazi, B. Dielectric Constants of Water, Methanol, Ethanol, Butanol and Acetone: Measurement and Computational Study. *Journal of Solution Chemistry* **39**, 701-708, doi:10.1007/s10953-010-9538-5 (2010).

125 De Yoreo, J. J. in *13 International Conference on Crystal Growth.* (eds T. Hibiya, J.B. Mullin, & M. Uwaha) (Elsevier).

126 Elhadj, S., De Yoreo, J. J., Hoyer, J. R. & Dove, P. M. Role of molecular charge and hydrophilicity in regulating the kinetics of crystal growth. *PNAS* **103**, 19237-19242 (2006).

127 Kashchiev, D. The kinetic approach to nucleation. *Crystal Research and Technology* **19**, 1413-1423, doi:https://doi.org/10.1002/crat.2170191102 (1984).

128 Farkas, L. Keimbildungsgeschwindigkeit in übersättigten Dämpfen. *Zeitschrift für Physikalische Chemie* **125U**, 236-242, doi:doi:10.1515/zpch-1927-12513 (1927).

129 Vallina, B., Rodriguez-Blanco, J. D., Brown, A. P., Blanco, J. A. & Benning, L. G. The role of amorphous precursors in the crystallization of La and Nd carbonates. *Nanoscale* **7**, 12166-12179, doi:10.1039/c5nr01497b (2015).

130 Rodriguez-Navarro, C., Burgos-Cara, A., Lorenzo, F. D., Ruiz-Agudo, E. & Elert, K. Nonclassical Crystallization of Calcium Hydroxide via Amorphous Precursors and the Role of Additives. *Crystal Growth & Design* **20**, 4418-4432, doi:10.1021/acs.cgd.0c00241 (2020).

131 Liu, Z. Zhang, Z., Wang, Z., Jin, B., Li, D., Tao, J., Tang, R. & Yoreo, J.J. Shape-preserving amorphous-to-crystalline transformation of $CaCO_3$ revealed by in situ TEM. *Proceedings of the National Academy of Sciences* **117**, 3397, doi:10.1073/pnas.1914813117 (2020).

132 Li, D. Nielsen, M.H., Lee, J.R. I., Fradsen, C., Banfield, J.F. & DeYoreo, J.J. Direction-Specific Interactions Control Crystal Growth by Oriented Attachment. *Science* **336**, 1014, doi:10.1126/science.1219643 (2012).

133 Gliko, O., Neumaier, N., Pan, W., Haase, I., Fischer, M., Bacher, A., Weinkauf, S. & Vekilov, P.G. A Metastable Prerequisite for the Growth of Lumazine Synthase Crystals. *Journal of the American Chemical Society* **127**, 3433-3438, doi:10.1021/ja043218k (2005).

134 Olafson, K. N., Ketchum, M. A., Rimer, J. D. & Vekilov, P. G. Mechanisms of hematin crystallization and inhibition by the antimalarial drug chloroquine. *Proceedings of the National Academy of Sciences* **112**, 4946, doi:10.1073/pnas.1501023112 (2015).

135 Ackerson, M. R., Mysen, B. O., Tailby, N. D. & Watson, E. B. Low-temperature crystallization of granites and the implications for crustal magmatism. *Nature* **559**, 94-97, doi:10.1038/s41586-018-0264-2 (2018).

136 Ni, P., Chabot, N. L., Ryan, C. J. & Shahar, A. Heavy iron isotope composition of iron meteorites explained by core crystallization. *Nature Geoscience* **13**, 611-615, doi:10.1038/s41561-020-0617-y (2020).

137 Daniels, M. J. D., Rivers-Auty, J., Schilling, T., Spencer, N.G., Watreme, W., Fasolino, V., Booth, S.J., White, Baldwin, A.G., Freeman, S., Wong, R., Latta, C., Yu, S., Jackson, J., Fisher, N., Koziel, V., Pillot, T., Bagnall, J., Allan, S.M., Paszek, P., Galea, J., Harte, M.K., Eder, C., Lawrence, C.B. & Brough, D. Fenamate NSAIDs inhibit the NLRP3 inflammasome and protect against

Alzheimer's disease in rodent models. *Nature Communications* **7**, 12504, doi:10.1038/ncomms12504 (2016).

138 Wang, Y. Wu, H., Li, P., Chen, S., Jones, L.O., Mosquera, M.A., Zhang, L., Cai, K., Chen, H., Chen, X-Y., Stern, C.L., Wasielewski, M.R., Schatz, G.C. & Stoddart, J.F. Two-photon excited deep-red and near-infrared emissive organic co-crystals. *Nature Communications* **11**, 4633, doi:10.1038/s41467-020-18431-7 (2020).

139 Pagola, S., Stephens, P. W., Bohle, D. S., Kosar, A. D. & Madsen, S. K. The structure of malaria pigment β-haematin. *Nature* **404** 307-310 (2000).

140 Kossel, W. *Nachr. Ges. Wiss. Götingen*, 135-138 (1928).

141 Chung, J., Granja, I., Taylor, M.G., Mpourmpakis, G., Asplin, J.R. & Rimer, J.D. Molecular modifiers reveal a mechanism of pathological crystal growth inhibition. *Nature* **536**, 446-450, doi:10.1038/nature19062

http://www.nature.com/nature/journal/vaop/ncurrent/abs/nature19062.html#supplementary-information (2016).

142 Dandekar, P., Kuvadia, Z. B. & Doherty, M. F. Engineering Crystal Morphology. *Annual Review of Materials Research* **43**, 359-386, doi:10.1146/annurev-matsci-071312-121623 (2013).

143 Giovannetti, R. in *Macro To Nano Spectroscopy* (ed Jamal Uddin) (IntechOpen, 2012).

144 Kano, K., Minamizono, H., Kitae, T. & Negi, S. Self-Aggregation of Cationic Porphyrins in Water. Can π–π Stacking Interaction Overcome Electrostatic Repulsive Force? *The Journal of Physical Chemistry A* **101**, 6118-6124, doi:10.1021/jp9710446 (1997).

145 PaineIII, J. B., Dolphin, D. & Gouterman, M. Exciton and electron interaction in covalently-linked dimeric porphyrins. *Canadian Journal of Chemistry* **56**, 1712-1715, doi:10.1139/v78-277 (1978).

146 Teng, H. H., Dove, P. M., Orme, C. A. & De Yoreo, J. J. Thermodynamics of calcite growth: baseline for understanding biomineral formation. *Science* **282**, 724-727 (1998).

147 Gliko, O., Reviakine, I. & Vekilov, P. G. Stable Equidistant Step Trains during Crystallization of Insulin. *Phys. Rev. Lett* **90**, 225503 (2003).

148 Orme, C. A., Noy, A., Wierzbicki, A., McBride, M.T., Grantham, M., Teng, H.H., Dove, P.M. & DeYoreo, J.J. Formation of chiral morphologies through selective binding of amino acids to calcite surface steps. *Nature* **411**, 775-779, doi:10.1038/35081034 (2001).

149 Vekilov, P. G., Kuznetsov, Y. G. & Chernov, A. A. Interstep interaction in solution growth; (101) ADP face. *J. Crystal Growth* **121**, 643-655 (1992).

150 Land, T. A., DeYoreo, J. J. & Lee, J. D. An in-situ AFM investigation of canavalin crystallization kinetics. *Surf. Sci.* **384**, 136-155 (1997).

151 Olafson, K. N., Rimer, J. D. & Vekilov, P. G. Early Onset of Kinetic Roughening due to a Finite Step Width in Hematin Crystallization. *Physical Review Letters* **119**, 198101 (2017).

152 Einstein, A. Zur Theorie der Brownschen Bewegung. *Annalen der Physik* **19**, 371-381 (1906).

153 Kramers, H. A. Brownian motion in a field of force and the diffusion model of chemical reactions. *Physica A* **7**, 284-304 (1940).

154 Frauenfelder, H. & Wolynes, P. G. Rate Theories and Puzzles of Hemeprotein Kinetics. *Science* **229**, 337-345 (1985).

155 Atkins, P. & DePaula, J. *Physical Chemistry*. Seventh edn, (Freeman, 2002).

156 Burton, W. K., Cabrera, N. &. Frank, F.C. The growth of crystals and equilibrium structure of their surfaces. *Phil. Trans. Roy. Soc. London Ser. A* **243**, 299- 360 (1951).

157 von Smoluchowski, M. Versuch einer matematischen theorie der koagulationskinetik kollpider losungen. *Z. Phys. Chem.* **92**, 129-135 (1918).

158 Zambelli, S. in *Chemical Kinetics* (ed Vivek Patel) 3-28 (InTech 2012).

159 Feldmann, T. & Demopoulos, G. P. Effects of crystal habit modifiers on the morphology of calcium sulfate dihydrate grown in strong CaCl2-HCl solutions. *Journal of Chemical Technology & Biotechnology* **89**, 1523-1533, doi:https://doi.org/10.1002/jctb.4231 (2014).

160 Ma, W., Lutsko, J. F., Rimer, J. D. & Vekilov, P. G. Antagonistic cooperativity between crystal growth modifiers. *Nature* **577**, 497-501, doi:10.1038/s41586-019-1918-4 (2020).

161 Sosa, R. D., Geng, X., Agarwal, A., Palmer, J.C., Conrad, J.C., Reynolds, M.A. & Rimer, J.D. Acidic Polysaccharides as Green Alternatives for Barite Scale Dissolution. *ACS Applied Materials & Interfaces* **12**, 55434-55443, doi:10.1021/acsami.0c16653 (2020).

162 Olafson, K. N., Nguyen, T. Q., Rimer, J. D. & Vekilov, P. G. Antimalarials inhibit hematin crystallization by unique drug–surface site interactions. *Proceedings of the National Academy of Sciences* **114**, 7531, doi:10.1073/pnas.1700125114 (2017).

163 Nielsen, L. C., De Yoreo, J. J. & DePaolo, D. J. General model for calcite growth kinetics in the presence of impurity ions. *Geochimica et Cosmochimica Acta* **115**, 100-114, doi:https://doi.org/10.1016/j.gca.2013.04.001 (2013).

164 Lupulescu, A. I., Kumar, M. & Rimer, J. D. A Facile Strategy To Design Zeolite L Crystals with Tunable Morphology and Surface Architecture. *Journal of the American Chemical Society* **135**, 6608-6617, doi:10.1021/ja4015277 (2013).

165 Liang, Y., Jacobson, A. J. & Rimer, J. D. Strontium Ions Function as Both an Accelerant and Structure-Directing Agent of Chabazite Crystallization. *ACS Materials Letters*, 187-192, doi:10.1021/acsmaterialslett.0c00460 (2020).

166 Eastman, R. T. & Fidock, D. A. Artemisinin-based combination therapies: a vital tool in efforts to eliminate malaria. *Nat Rev Microbiol* **7**, 864-874, doi:10.1038/nrmicro2239 (2009).

167 Mott, B. T., Eastman, R.T., Guha, R., Sherlach, K.S., Siriwardana, A., Shinn, P., McKnight, C., Michael, S., Lacerda-Queiroz, N., Patel, P.R., Khine, P., Sun, H., Kasbekar, M., Ashdam, N., Fontaine, S.D. Liu, D., Mierzwa, T., Mathews-Giner, L.A., Ferrer, M., Renslo, A.R., Inglese, J., Yuan, J., Roepe, P.D., Su, X-Z. & Thomas, C.J. High-throughput matrix screening identifies synergistic and antagonistic antimalarial drug combinations. *Sci Rep* **5**, 13891, doi:10.1038/srep13891

https://www.nature.com/articles/srep13891#supplementary-information (2015).

168 Gorka, A. P., Jacobs, L. M. & Roepe, P. D. Cytostatic versus cytocidal profiling of quinoline drug combinations via modified fixed-ratio isobologram analysis. *Malar J* **12**, 332-332, doi:10.1186/1475-2875-12-332 (2013).

169 Kras, W., Carletta, A., Montis, R., Sullivan, R. A. & Cruz-Cabeza, A. J. Switching polymorph stabilities with impurities provides a thermodynamic route to benzamide form III. *Communications Chemistry* **4**, 38, doi:10.1038/s42004-021-00473-7 (2021).

170 Dam, B., Bennema, P. & Van Enckevort, W. J. P. The mechanism of tapering on KDP-type crystals. *Journal of Crystal Growth* **74**, 118-128, doi:https://doi.org/10.1016/0022-0248(86)90254-X (1986).

171 Gibbs, J. W. On the equilibrium of heterogeneous substances, First Part. *Trans. Connect. Acad. Sci.* **3**, 108-248 (1876).

172 Weaver, M. L., Qiu, S.R., Hoyer, J.R., Casey, W.H., Nancollas, G.H., DeYoreo, J.J. Inhibition of calcium oxalate monohydrate growth by citrate and the effect of the background electrolyte. *J. Cryst. Growth* **306**, 135-145, doi:https://doi.org/10.1016/j.jcrysgro.2007.04.053 (2007).

173 De Yoreo, J. J. Physical Mechanisms of Crystal Growth Modification by Biomolecules. *AIP Conference Proceedings* **1270**, 45-58, doi:10.1063/1.3476238 (2010).

174 Cabrera, N. & Vermilyea, D. A. in *Growth and Perfection of Crystals* Vol. 393-408 (eds R.H. Doremus, B.W. Roberts, & D. Turnbul) (Wiley, 1958).

175 Kubota, N. & Mullin, J. W. A kinetic model for crystal growth from aqueous solution in the presence of impurity. *J. Cryst. Growth* **152**, 203-208, doi:https://doi.org/10.1016/0022-0248(95)00128-X (1995).

176 Potapenko, S. Y. Moving of step through impurity fence. *J. Cryst. Growth* **133**, 147-154 (1993).

177 Lee-Thorp, J. P., Shtukenberg, A. G. & Kohn, R. V. Effect of Step Anisotropy on Crystal Growth Inhibition by Immobile Impurity Stoppers. *Crystal Growth & Design* **17**, 5474-5487, doi:10.1021/acs.cgd.7b01006 (2017).

178 Lutsko, J. F., González-Segredo, N., Durán-Qlivencia, M.A., Maes, D., Driessche, A.E.S.V. & Sleutel, M. Crystal Growth Cessation Revisited: The Physical Basis of Step Pinning. *Crystal Growth & Design* **14**, 6129-6134, doi:10.1021/cg501307y (2014).

179 De Yoreo, J. More than one pathway. *Nature Materials* **12**, 284-285, doi:10.1038/nmat3604 (2013).

180 Choudhary, M. K., Kumar, M. & Rimer, J. D. Regulating Nonclassical Pathways of Silicalite-1 Crystallization through Controlled Evolution of Amorphous Precursors. *Angewandte Chemie International Edition* **58**, 15712-15716, doi:https://doi.org/10.1002/anie.201908751 (2019).

181 Jain, R. & Rimer, J. D. Seed-Assisted zeolite synthesis: The impact of seeding conditions and interzeolite transformations on crystal structure and morphology. *Microporous and Mesoporous Materials* **300**, 110174, doi:https://doi.org/10.1016/j.micromeso.2020.110174 (2020).

182 Pringsheim, T., Davenport, W. J. & Dodick, D. Acute treatment and prevention of menstrually related migraine headache. *Evidence-based review* **70**, 1555-1563, doi:10.1212/01.wnl.0000310638.54698.36 (2008).

183 Olafson, K. N., Nguyen, T. Q., Rimer, J. D. & Vekilov, P. G. Antimalarials inhibit hematin crystallization by unique drug–surface site interactions. *Proceedings of the*

National Academy of Sciences **114**, 7531-7536, doi:10.1073/pnas.1700125114 (2017).